TECHNICAL IMPROVEMENTS IN QUANTITATIVE SUSCEPTIBILITY MAPPING

TECHNICAL IMPROVEMENTS IN QUANTITATIVE SUSCEPTIBILITY MAPPING

BY

SAIFENG LIU B.Sc.

A Thesis

Submitted to the School of Biomedical Engineering

and the School of Graduate Studies

of McMaster University

in Partial Fulfilment of the Requirements

for the Degree of

Doctor of Philosophy

Ph. D. (2014) McMaster University

(School of Biomedical Engineering) Hamilton, Ontario, Canada

TITLE: Technical Improvements in Quantitative Susceptibility Mapping

AUTHOR: Saifeng Liu

B.Sc., (Biomedical Engineering)

Huazhong University of Science and Technology

Wuhan, China

SUPERVISOR: E. Mark Haacke Ph. D.

NUMBER OF PAGES: xx, 192

To my parents

Fenling Liu and Yongqi Liu

Abstract

Quantitative susceptibility mapping (QSM) is a promising technique to study tissue properties and function *in vivo*. The presence of a susceptibility source will lead to a non-local field variation which manifests as a non-local behavior in magnetic resonance phase images. QSM is an ill-posed inverse problem that maps the phase back to the susceptibility source. In practice, the phase images are usually contaminated by background field inhomogeneities. Consequently, the efficacy and accuracy of QSM rely on background field removal. In this thesis, several technical advances in QSM have been made which accelerate the data processing and improve the accuracy of this ill-posed problem.

Different background field removal algorithms are analyzed and compared in detail, including homodyne high-pass filtering, variable high-pass filtering, sophisticated harmonic artefact reduction for phase data (SHARP), and projection onto the dipole field (PDF). In these algorithms, phase unwrapping is usually required, which can be time-consuming and sensitive to noise. To solve this problem, a new background field removal algorithm, local spherical mean value filtering (LSMV), is proposed, in which the global phase unwrapping is bypassed. This algorithm improves the time-efficiency and robustness of background field removal, especially for double-echo data.

The simplest algorithm to solve the inverse problem is the regularization process using truncated k-space division. However, this algorithm induces streaking artefacts in the

susceptibility maps. The streaking artefacts can be reduced dramatically using geometry constraints. In the k-space/image domain iterative algorithm for susceptibility weighted imaging and mapping (SWIM), the geometries extracted from the initial susceptibility maps are used to update the data in the singularity regions in k-space. An improved version of this algorithm is demonstrated using multi-level thresholding to account for the variation in the susceptibilities of different structures in the brain.

These susceptibility maps could be used to generate orientation independent weighting masks, to form a new type of susceptibility weighted image (SWI), referred to here as true-SWI (tSWI). The tSWI data show improved contrast-to-noise ratio (CNR) of the veins and reduced blooming artefacts due to the strong dipolar phase of microbleeds.

Finally, the accuracy in estimating the susceptibility of a small object is usually hampered by partial volume effects. In this thesis, it is shown that the effective magnetic moment, being the product of the apparent volume and the measured susceptibility of the small object, is constant and can be used to improve the susceptibility quantification, if *a priori* information of the volume is available.

In conclusion, the technical improvements presented in this thesis contribute to a better data processing scheme for QSM, with accelerated data processing by using the LSMV algorithm for background field removal, reduced streaking artefacts in the susceptibility maps by using the iterative SWIM algorithm for solving the inverse problem, and improved accuracy by proper handling of the partial volume effects using volume constraints.

Acknowledgements

I would like to express my deepest appreciation to my supervisor, Dr. E. Mark Haacke, for his enduring support and persistent inspiration. It is Dr. Haacke who led me into the exciting and intriguing world of MRI. As one of the great scientists in this field, Dr. Haacke has demonstrated to me how the knowledge of spins in MRI and expertise in physics can be applied to both MRI and tennis. It is his passion for both research and life that has encouraged me to finish the work presented in this thesis.

I would like to thank my supervisory committee members, Dr. Nicholas Bock, Dr. Qiyin Fang, and Dr. Maureen MacDonald, for their valuable guidance and comments. Thanks to Dr. Michael Noseworthy, for helping me on extending my research horizon and improving my teaching skills.

Moreover, I would like to thank Dr. Yu-Chung Norman Cheng, Dr. Yongquan Ye and Dr. Jaladhar Neelavalli, for their careful reviewing of my thesis. Thanks to my colleagues and friends Sagar Buch M. Sc., Jin Tang Ph.D., Eyesha Hashim, B. Sc., Weili Zheng Ph.D. and Manju Liu M. Sc.

Finally, I wish to thank my grandfather Bingyan Liu (1933-2012) and grandmother Hongzhu Liu, for their endless love.

Contents

List of Figures

List of Tables

List of Abbreviations

ANOVA	Analysis of variance
BW	Bandwidth
CMRO2	Cerebral metabolic rate of oxygen
CN	Caudate nucleus
CNR	Contrast-to-noise ratio
CSF	Cerebrospinal fluid
FA	Flip angle
FOV	Field of view
FSL	FMRIB Software Library
GDAC	Geometry dependent artefact correction
GP	Globus pallidus
GRAPPA	Generalized Autocalibrating Partially Parallel Acquisitions
GRE	Gradient recalled echo
Hct	Hematocrit
ICP-MS	Inductively coupled plasma mass spectrometry
Iterative SWIM	k-space/image domain iterative algorithm for susceptibility weighted imaging and mapping
LSMV	Local spherical mean value filtering

MEDI	Morphology enabled dipole inversion
mIP	Minimum intensity projection
MIP	Maximum intensity projection
MRI	Magnetic resonance imaging
MS	Multiple sclerosis
PD	Parkinson's disease
PDF	Projection onto the Dipole Field
PRELUDE	Phase region expanding labeller for unwrapping discrete estimates
PUT	Putamen
QSM	Quantitative susceptibility mapping
RMSD	Root-mean-square-deviation
RMSE	Root-mean-square-error
RN	Red nucleus
ROI	Region of interest
SHARP	Sophisticated Harmonic Artifact Reduction for Phase data
SMV	Spherical mean value filtering
SN	Substantia Nigra
SNR	Signal-to-noise ratio
SSS	Superior sagittal sinus
SWI	Susceptibility weighted imaging
TBI	Traumatic brain injury
TE	Echo Time
THA	Thalamus

TR	Repetition time
tSWI	True susceptibility weighted imaging
VHP	Variable high-pass filter
VOI	Volume of interest
XRF	X-ray fluorescence

Chapter 1 Introduction

1.1 Background and significance

Magnetic Resonance Imaging (MRI) provides both structural and functional information through magnitude and phase images. The contrast in the images is dependent on the sequence design and the associated acquisition parameters. In Susceptibility Weighted Imaging (SWI), phase images are combined with magnitude images to enhance the visualization of veins, iron (in the form of ferritin or hemosiderin if microbleeds have occurred) or calcium (1-3). Although SWI has been widely used for many clinical applications, it is hampered by the orientation dependence of phase information, especially when high imaging resolution is used (4,5). In that case, there will be errors in visualizing the veins and microbleeds. Besides, the orientation dependence of phase makes it difficult to quantify the iron/calcium content using SWI. On the other hand, susceptibility is known to be (for the most part) independent of orientation (5,6). Thus, mapping the susceptibility distribution, the source of phase information, is of great interest.

Quantitative Susceptibility Mapping (QSM) provides a robust means to elucidate tissue properties and function through tissue susceptibilities, which are related to the changes in

the deposition of paramagnetic (e.g., iron) or diamagnetic (e.g., calcium or myelin content in white matter) substances. Susceptibility changes are also related to the changes in the oxygenation level of venous blood. As a result, QSM has many potential clinical applications, such as the quantification of cerebral iron deposition or calcium (7), visualization and quantification of iron loaded biomarkers such as iron loaded stem cells, as well as quantification of venous oxygen saturation (8,9). In this section, we shall give a brief review of these applications.

Cerebral iron content can be categorized as heme iron and non-heme iron (16). The former is related to hemoglobin and transportation of oxygen, while the latter is related to iron storage or deposition, predominantly in the form of ferritin and hemosiderin macromolecules which are paramagnetic. Excessive iron deposition in deep gray matter structures such as the basal ganglia has been observed in many neurodegenerative diseases including: Alzheimer's disease (10), Parkinson's disease (11,12), and multiple sclerosis (13-16) to name just a few. Increased iron deposition is also present in the normal aging process (17-19). Studies have been performed to investigate the relation between the measured susceptibility and the absolute iron content using *in vitro* ferritin solutions (20). This relation is further compared and validated with that found in cadaver brains, for which the iron content can be measured by both QSM and other quantitative methods such as inductively coupled plasma mass spectrometry (ICP-MS) and x-ray fluorescence (XRF) (20,21). While the quantification of cerebral iron deposition, especially in the basal ganglia structures, helps to monitor the progress of neurodegenerative diseases and to evaluate treatment, a temporal profile and normal

baseline of the cerebral iron deposition in the normal aging process would facilitate the discrimination of the subjects with excessive cerebral iron deposition from normal healthy controls. This could be particularly beneficial for the early diagnosis of neurodegenerative diseases.

Using QSM, it is viable to quantify not only the paramagnetic substances, but also diamagnetic substances such as calcium. Detection and quantification of calcium has long been a topic of interest in MRI. For example, SWI was formerly used to detect calcifications in the breast (3). QSM has also been used to differentiate between diamagnetic and paramagnetic cerebral lesions (7). Moreover, measuring calcification in vessel walls is also of great interest. For example, intracranial arterial calcification has been shown to be highly correlated with coronary artery disease for ischemic stroke patients (22).

Another potential application of QSM is to monitor the cerebral myelination/demyelination process. This may be useful in studying demyelinating diseases such as multiple sclerosis and acute disseminated encephalomyelitis (23). It has been shown that the diamagnetic myelin is the major source of susceptibility differences between white matter and gray matter including phase and T_2^*/R_2^* effects (24,25). This has been shown by comparing the grey and white matter phase contrast between demyelinated shiverer mice and normal control mice using MRI, followed by histological staining of myelin. The contribution of myelin content to grey/white matter phase contrast was also validated using post-mortem studies (26). Meanwhile, orientation dependence of T_2^*/R_2^* was observed and was attributed to the fibre orientation of myelin content in

white matter (25,27,28). This orientation dependence of T_2^* was the strongest in the optic radiation, which is known to have little iron content (27). Susceptibility anisotropy was also observed in the deep white matter and a susceptibility tensor model has been invoked in an attempt to describe the susceptibility behaviour found in the white matter (6).

Finally, the measurement of venous oxygen saturation is another important application of QSM. It has been shown that the changes in venous oxygen saturation can be reflected by the changes in susceptibility(8). Together with the flow information, MRI can be used to quantify cerebral metabolic rate of oxygen (CMRO2) and to examine the cerebral functional changes in stroke and other neurodegenerative diseases. For example, it was shown that the visibility of periventricular veins was reduced in multiple sclerosis patients, due to the reduced brain function and reduced utilization of oxygen (hence more diamagnetic venous blood) (29). Furthermore, it is of great interest to measure the venous oxygen saturation in the spinal cord, in order to study the mechanism of blood flow and oxygen regulation (30,31). All of these applications discussed above depend on proper reconstruction of the susceptibility map.

1.2 Review of QSM techniques

The past few years have witnessed much progress in QSM. Various *in vivo* data acquisition and processing methods have been proposed. The *in vivo* MR data are typically acquired using a gradient echo (GRE) sequence with either single or multiple echoes (8,32,33). Accurate quantification of the susceptibility relies on many factors. The choice of echo time (TE) will affect the phase image signal-to-noise ratio (SNR) and the

level of phase aliasing (8). Meanwhile, T_2^* signal decay and the blooming artefact at long TEs may lead to errors in susceptibility quantification (34,35) due to aliasing of the phase at the edge of the structure of interest. Another important parameter in data acquisition is the resolution. While low resolution leads to more severe partial volume effects and hence a larger error in susceptibility quantification, especially for small objects (35), high resolution generally requires a longer scan time and has reduced SNR. Given the development in fast imaging methods (36,37), it can be expected that data acquired with high resolution will become more and more common in the future. Furthermore, when the focus is the veins, full multi-directional flow compensation is required in order to avoid the spurious phase component induced by blood flow (mostly in the arteries) (5,8,38).

In QSM data processing, the two most important steps are background field removal and the inverse process used to reconstruct the susceptibility map from the local phase information. QSM relies on pristine field (phase) information, which is induced by the local susceptibility distribution. The background field, on the other hand, is mainly induced by the global geometry such as the air/bone-tissue interfaces and main magnetic field inhomogeneity (2,38-40). Background fields lead to phase aliasing and signal decay at a long TE. Typically, the background field is removed through high-pass filtering, due to its low spatial frequency (2). But high-pass filtering causes inevitable signal loss of the local field variation. For a particular object, the signal loss due to high-pass filtering is dependent on both the size of the high-pass filter and the size of the object. Newer algorithms aim to reduce this signal loss of the local field while effectively removing the background field (38,40). One problem with all these algorithms is the loss of information

near the interface between susceptibility sources, such as the edge of the brain and air. Normally an eroded binary mask is used to perform the calculation only for the central regions (38,40). Another common problem is the requirement of phase unwrapping (38,40). Phase unwrapping is sensitive to noise in phase images and is particularly problematic when cusp artefacts are present (41,42). Cusp artefacts are typically caused by an improper combination of multi-channel phase data (1,43,44). Further, multi-dimensional phase unwrapping is usually time-consuming (45,46). Fast phase unwrapping algorithms such as the Laplacian based algorithm can still suffer from errors in regions with rapid field changes, i.e., the edges of the veins or air/tissue interfaces (41,47). The use of double or multi-echo data helps to alleviate the problems related to phase unwrapping (48). Particularly, when a double-echo GRE sequence with a short first TE is used, phase unwrapping can be avoided in the background field removal step, an approach that will be taken later in this thesis.

Using the extracted local phase information, various algorithms have been proposed to reconstruct the susceptibility map, based on the relation between the susceptibility distribution and local field variation. However, the Green's function in the Fourier domain has zeros and thus QSM is an ill-posed inverse problem (8,32,49-52). The singularities of the Green's function lead to streaking artefacts in susceptibility maps even when regularization methods are used. The simplest way of solving this inverse problem is to define a Fourier domain threshold and to use truncated k-space division (8,53). A larger threshold leads to a reduced level of streaking artefacts but also a larger error in the estimated susceptibility due to more signal loss in k-space (8) and more blurring of

individual structures (41). There is always this type of trade-off between the accuracy in the susceptibility estimation and the quality of artefact suppression.

In conclusion, the robustness of QSM processing is usually hampered by the background field removal step. Particularly, the requirement of phase unwrapping in background field removal makes it vulnerable to cusp artefacts in phase images. The accuracy of QSM relies on several factors. Among those is the geometry information which plays an indispensable role. The motivation of this study is to develop fast and robust data processing methods for quantitative susceptibility mapping and to study the accuracy in susceptibility estimation.

1.3 Overview of the thesis

In Chapter 2, we introduce the basic theories, including signal formation mechanisms using a gradient echo sequence, the phase information and magnetic susceptibility. Given an arbitrary susceptibility distribution, the induced field variation can be predicted through a forward field calculation. On the other hand, QSM requires solving an inverse problem. An overview of QSM data processing procedures is given in that chapter. In Chapter 3, we focus on the first important step in QSM data processing: background field removal. Different filtering techniques are discussed in detail, including homodyne high-pass filtering, variable high-pass filtering (VHP), Sophisticated Harmonic Artefact Reduction for Phase data (SHARP) and Projection onto Dipole Fields (PDF). The accuracy of these filters are evaluated and compared. In Chapter 4, a double-echo phase processing algorithm is introduced. The advantages of such an algorithm are its

robustness and time-efficiency. Chapter 5 is focused on the core procedure of QSM, the inverse process. A geometry constrained iterative algorithm for susceptibility mapping is introduced and evaluated. A direct application of QSM is to use the susceptibility map to generate susceptibility weighting masks to improve the visualization of the venous structures, as is discussed in Chapter 6. Chapter 7 deals with the limitation of susceptibility estimation of small objects. In that chapter, we show that even though the accuracy of the susceptibility estimation is limited by the apparent volume, the product of susceptibility and volume (or the effective magnetic moment) is constant. Conclusions and future directions are provided in Chapter 8.

References

1. Haacke EM, Mittal S, Wu Z, Neelavalli J, Cheng YCN. Susceptibility-Weighted Imaging: Technical Aspects and Clinical Applications, Part 1. Am. J. Neuroradiol. 2009;30:19-30.
2. Haacke EM, Xu Y, Cheng YCN, Reichenbach JR. Susceptibility weighted imaging (SWI). Magn. Reson. Med. 2004;52:612-8.
3. Fatemi-Ardekani A, Boylan C, Noseworthy MD. Identification of breast calcification using magnetic resonance imaging. Med. Phys. 2009;36:5429-36.
4. Xu Y, Haacke EM. The role of voxel aspect ratio in determining apparent vascular phase behavior in susceptibility weighted imaging. Magn. Reson. Imaging 2006;24:155-60.
5. Haacke EM, Reichenbach JR, editors. Susceptibility Weighted Imaging in MRI: Basic Concepts and Clinical Applications. 1st ed. Wiley-Blackwell; 2011.
6. Liu C. Susceptibility tensor imaging. Magn. Reson. Med. 2010;63:1471-7.
7. Schweser F, Deistung A, Lehr BW, Reichenbach JR. Differentiation between diamagnetic and paramagnetic cerebral lesions based on magnetic susceptibility mapping. Med. Phys. 2010;37:5165.
8. Haacke EM, Tang J, Neelavalli J, Cheng YC. Susceptibility mapping as a means to visualize veins and quantify oxygen saturation. J. Magn. Reson. Imaging 2010;32:663-76.
9. Jain V, Abdulmalik O, Propert KJ, Wehrli FW. Investigating the magnetic susceptibility properties of fresh human blood for noninvasive oxygen saturation quantification. Magn. Reson. Med. 2012;68:863-7.
10. Langkammer C, Ropele S, Pirpamer L, Fazekas F, Schmidt R. MRI for Iron Mapping in Alzheimer's Disease. Neurodegener. Dis. 2013;
11. Wallis LI, Paley MNJ, Graham JM, Grünewald RA, Wignall EL, Joy HM, et al. MRI assessment of basal ganglia iron deposition in Parkinson's disease. J. Magn. Reson. Imaging 2008;28:1061-7.
12. Wang Y, Butros SR, Shuai X, Dai Y, Chen C, Liu M, et al. Different iron-deposition patterns of multiple system atrophy with predominant parkinsonism and idiopathetic Parkinson diseases demonstrated by phase-corrected susceptibility-weighted imaging. AJNR Am. J. Neuroradiol. 2012;33:266-73.
13. Al-Radaideh AM, Wharton SJ, Lim S-Y, Tench CR, Morgan PS, Bowtell RW, et al. Increased iron accumulation occurs in the earliest stages of demyelinating disease: an ultra-high field susceptibility mapping study in Clinically Isolated Syndrome. Mult. Scler. J. 2013;19:896-903.
14. Haacke EM, Makki M, Ge Y, Maheshwari M, Sehgal V, Hu J, et al. Characterizing iron deposition in multiple sclerosis lesions using susceptibility weighted imaging. J. Magn. Reson. Imaging 2009;29:537-44.
15. Langkammer C, Liu T, Khalil M, Enzinger C, Jehna M, Fuchs S, et al. Quantitative susceptibility mapping in multiple sclerosis. Radiology 2013;267:551-9.
16. Walsh AJ, Lebel RM, Eissa A, Blevins G, Catz I, Lu J-Q, et al. Multiple sclerosis: validation of MR imaging for quantification and detection of iron. Radiology 2013;267:531-42.

17. Haacke EM, Cheng NYC, House MJ, Liu Q, Neelavalli J, Ogg RJ, et al. Imaging iron stores in the brain using magnetic resonance imaging. Magn. Reson. Imaging 2005;23:1-25.
18. Bilgic B, Pfefferbaum A, Rohlfing T, Sullivan EV, Adalsteinsson E. MRI estimates of brain iron concentration in normal aging using quantitative susceptibility mapping. NeuroImage 2012;59:2625-35.
19. Haacke EM, Ayaz M, Khan A, Manova ES, Krishnamurthy B, Gollapalli L, et al. Establishing a baseline phase behavior in magnetic resonance imaging to determine normal vs. abnormal iron content in the brain. J. Magn. Reson. Imaging 2007;26:256-64.
20. Zheng W, Nichol H, Liu S, Cheng Y-CN, Haacke EM. Measuring iron in the brain using quantitative susceptibility mapping and X-ray fluorescence imaging. NeuroImage 2013;78:68-74.
21. Langkammer C, Krebs N, Goessler W, Scheurer E, Ebner F, Yen K, et al. Quantitative MR Imaging of Brain Iron: A Postmortem Validation Study. Radiology 2010;257:455-462.
22. Ahn SS, Nam HS, Heo JH, Kim YD, Lee S-K, Han KH, et al. Ischemic stroke: measurement of intracranial artery calcifications can improve prediction of asymptomatic coronary artery disease. Radiology 2013;268:842-9.
23. Chitnis T. Pediatric demyelinating diseases. Contin. Minneap. Minn 2013;19:1023-45.
24. Liu C, Li W, Johnson GA, Wu B. High-field (9.4 T) MRI of brain dysmyelination by quantitative mapping of magnetic susceptibility. NeuroImage 2011;56:930-8.
25. Lee J, Shmueli K, Kang B-T, Yao B, Fukunaga M, van Gelderen P, et al. The contribution of myelin to magnetic susceptibility-weighted contrasts in high-field MRI of the brain. NeuroImage 2012;59:3967-75.
26. Langkammer C, Krebs N, Goessler W, Scheurer E, Yen K, Fazekas F, et al. Susceptibility induced gray-white matter MRI contrast in the human brain. NeuroImage 2012;59:1413-9.
27. Sati P, Silva AC, van Gelderen P, Gaitan MI, Wohler JE, Jacobson S, et al. In vivo quantification of T_2 anisotropy in white matter fibers in marmoset monkeys. NeuroImage 2012;59:979-85.
28. Lee J, van Gelderen P, Kuo L-W, Merkle H, Silva AC, Duyn JH. T2*-based fiber orientation mapping. NeuroImage 2011;57:225-34.
29. Ge Y, Zohrabian VM, Osa E-O, Xu J, Jaggi H, Herbert J, et al. Diminished visibility of cerebral venous vasculature in multiple sclerosis by susceptibility-weighted imaging at 3.0 Tesla. J. Magn. Reson. Imaging 2009;29:1190-4.
30. Fujima N, Kudo K, Terae S, Ishizaka K, Yazu R, Zaitsu Y, et al. Non-invasive measurement of oxygen saturation in the spinal vein using SWI: quantitative evaluation under conditions of physiological and caffeine load. NeuroImage 2011;54:344-9.
31. Fujima N, Kudo K, Terae S, Hida K, Ishizaka K, Zaitsu Y, et al. Spinal arteriovenous malformation: evaluation of change in venous oxygenation with susceptibility-weighted MR imaging after treatment. Radiology 2010;254:891-9.

32. Liu J, Liu T, de Rochefort L, Ledoux J, Khalidov I, Chen W, et al. Morphology enabled dipole inversion for quantitative susceptibility mapping using structural consistency between the magnitude image and the susceptibility map. NeuroImage 2012;59:2560-8.
33. Wu B, Li W, Avram AV, Gho S-M, Liu C. Fast and tissue-optimized mapping of magnetic susceptibility and T2* with multi-echo and multi-shot spirals. NeuroImage 2012;59:297-305.
34. Liu T, Surapaneni K, Lou M, Cheng L, Spincemaille P, Wang Y. Cerebral microbleeds: burden assessment by using quantitative susceptibility mapping. Radiology 2012;262:269-78.
35. Liu S, Neelavalli J, Cheng Y-CN, Tang J, Mark Haacke E. Quantitative susceptibility mapping of small objects using volume constraints. Magn. Reson. Med. 2013;69:716-23.
36. Xu Y, Haacke EM. An iterative reconstruction technique for geometric distortion-corrected segmented echo-planar imaging. Magn. Reson. Imaging 2008;26:1406-14.
37. Zwanenburg JJM, Versluis MJ, Luijten PR, Petridou N. Fast high resolution whole brain T2* weighted imaging using echo planar imaging at 7T. NeuroImage 2011;56:1902-7.
38. Schweser F, Deistung A, Lehr BW, Reichenbach JR. Quantitative imaging of intrinsic magnetic tissue properties using MRI signal phase: An approach to in vivo brain iron metabolism? NeuroImage 2011;54:2789-807.
39. Neelavalli J, Cheng YN, Jiang J, Haacke EM. Removing background phase variations in susceptibility-weighted imaging using a fast, forward-field calculation. J. Magn. Reson. Imaging 2009;29:937-48.
40. Liu T, Khalidov I, de Rochefort L, Spincemaille P, Liu J, Tsiouris AJ, et al. A novel background field removal method for MRI using projection onto dipole fields (PDF). NMR Biomed. 2011;24:1129-36.
41. Schweser F, Deistung A, Sommer K, Reichenbach JR. Toward online reconstruction of quantitative susceptibility maps: Superfast dipole inversion. Magn. Reson. Med. 2013; 69(6):1582-94;
42. Liu T, Wisnieff C, Lou M, Chen W, Spincemaille P, Wang Y. Nonlinear formulation of the magnetic field to source relationship for robust quantitative susceptibility mapping. Magn. Reson. Med. 2013;69:467-76.
43. Hammond KE, Lupo JM, Xu D, Metcalf M, Kelley DAC, Pelletier D, et al. Development of a robust method for generating 7.0 T multichannel phase images of the brain with application to normal volunteers and patients with neurological diseases. NeuroImage 2008;39:1682-92.
44. Robinson S, Grabner G, Witoszynskyj S, Trattnig S. Combining phase images from multi-channel RF coils using 3D phase offset maps derived from a dual-echo scan. Magn. Reson. Med. 2011;65:1638-48.
45. Jenkinson M. Fast, automated, N-dimensional phase-unwrapping algorithm. Magn. Reson. Med. 2003;49:193-7.

46. Abdul-Rahman HS, Gdeisat MA, Burton DR, Lalor MJ, Lilley F, Moore CJ. Fast and robust three-dimensional best path phase unwrapping algorithm. Appl. Opt. 2007;46:6623-35.
47. Li W, Wu B, Liu C. Quantitative susceptibility mapping of human brain reflects spatial variation in tissue composition. NeuroImage 2011;55:1645-56.
48. Feng W, Neelavalli J, Haacke EM. Catalytic multiecho phase unwrapping scheme (CAMPUS) in multiecho gradient echo imaging: removing phase wraps on a voxel-by-voxel basis. Magn. Reson. Med. 2013;70:117-26.
49. Salomir R, de Senneville BD, Moonen CT. A fast calculation method for magnetic field inhomogeneity due to an arbitrary distribution of bulk susceptibility. Concepts Magn. Reson. Part B Magn. Reson. Eng. 2003;19B:26-34.
50. Tang J, Liu S, Neelavalli J, Cheng YCN, Buch S, Haacke EM. Improving susceptibility mapping using a threshold-based K-space/image domain iterative reconstruction approach. Magn. Reson. Med. 2013;69:1396-407.
51. Schweser F, Sommer K, Deistung A, Reichenbach JR. Quantitative susceptibility mapping for investigating subtle susceptibility variations in the human brain. NeuroImage 2012;62:2083-100.
52. Liu T, Spincemaille P, de Rochefort L, Kressler B, Wang Y. Calculation of susceptibility through multiple orientation sampling (COSMOS): A method for conditioning the inverse problem from measured magnetic field map to susceptibility source image in MRI. Magn. Reson. Med. 2009;61:196-204.
53. Shmueli K, de Zwart JA, van Gelderen P, Li T, Dodd SJ, Duyn JH. Magnetic susceptibility mapping of brain tissue in vivo using MRI phase data. Magn. Reson. Med. 2009;62:1510-22.

Chapter 2 Basic Concepts of Phase, Gradient Echo Imaging and Quantitative Susceptibility Mapping[1]

2.1 The concept of a gradient echo and phase

Gradient recalled echo (GRE) sequence is one of the most frequently used imaging methods in MRI. To start our story, let's first take a look at the gradient echo signal formation mechanism. When placed in an external magnetic field, $\vec{B}_0$, the spins or protons will precess about $\vec{B}_0$ at the Larmor frequency defined as:

$$\omega_0 = \gamma B_0 \qquad [2.1],$$

where γ is the gyromagnetic ratio of protons ($2.68 \cdot 10^8 \cdot rad \cdot s^{-1} \cdot T^{-1}$). Upon the excitation by a radial-frequency (RF) pulse, e.g., a 90^o pulse, the longitudinal magnetization will be tipped into the transverse plane. The longitudinal magnetization will gradually recover

[1]Most of the contents in this chapter are adapted from Haacke EM, et al. Magnetic Resonance Imaging: Physical Principles and Sequence Design. 1st ed. Wiley-Liss; 1999, and Haacke EM, Reichenbach JR, editors. Susceptibility Weighted Imaging in MRI: Basic Concepts and Clinical Applications. 1st ed. Wiley-Blackwell; 2011.

toward the equilibrium state parallel to $\vec{B}_0$. This process is described using the Bloch equations (1). Particularly, there are two important relaxation times involved in this process, being the spin-lattice relaxation time T_1 and the spin-spin relaxation time T_2. While the former relaxation time describes the regrowth rate of the longitudinal magnetization, the latter represents the decaying rate of the magnetization in the transverse plane. Practically speaking, due to global and local field inhomogeneities of various origins, the spins in the transverse plane will experience extra dephasing effects and thus the magnetization will decay much faster. This expedited decay rate is described using the T_2^* time constant, which is defined as:

$$\frac{1}{T_2^*} = \frac{1}{T_2} + \frac{1}{T_2'} \qquad [2.2],$$

where $1/T_2'$, or R_2' corresponds to the dephasing effects caused by field inhomogeneities.

In a 3D imaging experiment with linearly varying gradients $G_x(t)$, $G_y(t)$ and $G_z(t)$ applied in three orthogonal directions, the local magnetic field becomes:

$$B(\vec{x},\vec{y},\vec{z},t) = \vec{B}_0 + G_x(t)\cdot\vec{x} + G_y(t)\cdot\vec{y} + G_z(t)\cdot\vec{z} \qquad [2.3].$$

The spin isochromats will precess at the Larmor frequencies proportional to the local magnetic field, and the accumulated phase induced by the linear gradient can be written as:

$$\phi_G(\vec{x},\vec{y},\vec{z},t) = -\gamma[\int_0^t dt' G_x(t')\vec{x} + \int_0^t dt' G_y(t')\vec{y} + \int_0^t dt' G_z(t')\vec{z}] \qquad [2.4].$$

It is shown that, with relaxation effects neglected, the signal can be written as (1):

$$s(t) = \iiint dx\, dy\, dz\, \rho(\vec{x}, \vec{y}, \vec{z},) e^{i\phi_G(\vec{x},\vec{y},\vec{z},t)} \quad [2.5],$$

where $\rho(x, y, z)$ is the effective proton density. Let's further define:

$$k_x(t) = \gamma\!\!\!^{-} \int_0^t dt' G_x(t'), \quad k_y(t) = \gamma\!\!\!^{-} \int_0^t dt' G_y(t'), \quad k_z(t) = \gamma\!\!\!^{-} \int_0^t dt' G_z(t') \quad [2.6],$$

where $\gamma\!\!\!^{-} = \gamma/2\pi$. Using Eqs. 2.4 and 2.6, Eq. 2.5 becomes:

$$s(k_x, k_y, k_z) = \iiint dx\, dy\, dz\, \rho(\vec{x}, \vec{y}, \vec{z}) e^{-2\pi i(k_x\vec{x} + k_y\vec{y} + k_z\vec{z})} \quad [2.7].$$

Eq. 2.7 clearly indicates that the signal is the Fourier transform of the effective proton density, $\rho(\vec{x}, \vec{y}, \vec{z})$. Therefore we name the signal space defined by Eq. 2.7 as "k-space". With an inverse Fourier transform, the complex data of $\rho(\vec{x}, \vec{y}, \vec{z})$ can be obtained in the spatial domain. Magnitude and phase images can then be extracted from this complex data.

In order to reconstruct the effective proton density, sufficient coverage of k-space is required. This is achieved by varying the duration or amplitude of the gradients $G_x(t)$, $G_y(t)$ and $G_z(t)$. Assuming that $G_x(t)$ is the readout gradient, $G_y(t)$ and $G_z(t)$ are the phase encoding and slab selection gradients, the timing and amplitudes of these gradients can be described by the sequence diagram (2). A typical 3D gradient echo sequence diagram is shown in **Fig. 2.1**.

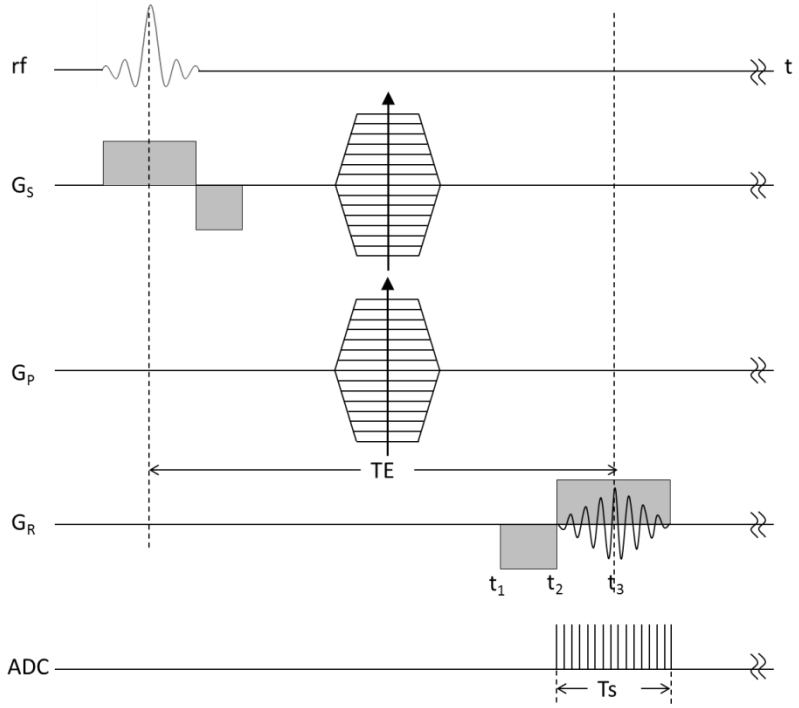

Figure 2.1 Sequence diagram of a single echo 3D gradient echo sequence. G_S: slab selection/partition encoding gradient; G_P: phase encoding gradient; G_R: readout gradient.

The k-space trajectory can be understood from **Fig. 2.2**. Assuming that the duration of both the slab selection gradient G_s and the phase encoding gradient G_P is t_P, the amplitude of G_P is at its maximum $G_{p,max}$, at $t=t_1$, using Eq. 2.6, the k-space data points being sampled can be represented as:

$$k_y = \gamma G_{p,max} t_p = k_{y,max}, \quad k_z = \gamma G_s t_p \qquad [2.8].$$

This corresponds to the data points in the first row in **Fig. 2.2**.

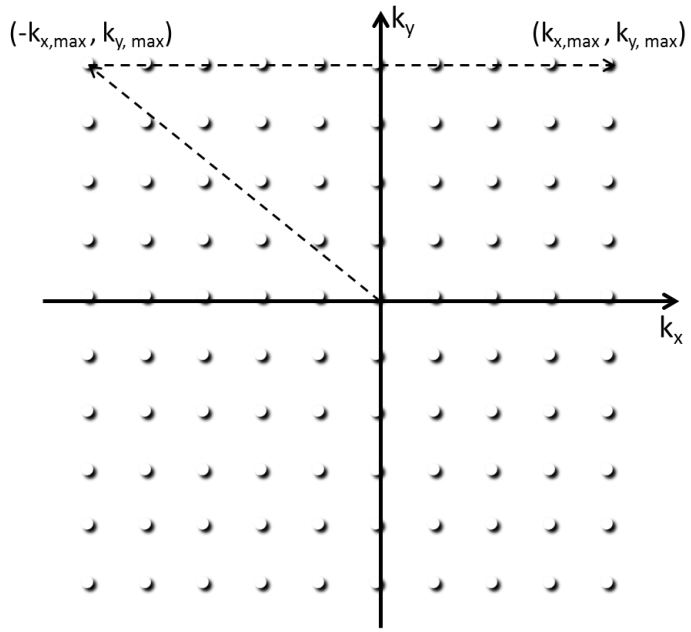

Figure 2.2 Illustration of filling one line in k-space. The k-space trajectory as indicated by the dashed arrows is described using Eqs.2.8 to 2.10.

Starting from $t=t_1$, the negative lobe of the readout gradient (with amplitude $-G_R$) will be applied, using Eq. 2.6 again, the k-space trajectory in x direction can be written as:

$$k_x(t) = -\gamma G_R(t - t_1) \qquad t_1 \le t \le t_2 \qquad [2.9].$$

This corresponds to moving from $k_x = 0$ toward $k_x = -\gamma G_R(t_2 - t_1) = -k_{x,max}$ in k-space. The positive lobe of the readout gradient is applied starting from $t = t_2$. The k-space trajectory in k_x direction becomes:

$$k_x(t) = -\gamma G_R(t_2 - t_1) + \gamma G_R(t - t_2) \quad t \ge t_2 \qquad [2.10].$$

When $t - t_2 = t_2 - t_1$ (that is when $t = t_3$), $k_x = 0$ and an echo is formed. The duration from the RF pulse to t_3 is defined as the echo time (TE), as shown in **Fig. 2.1**. Starting from $t=t_2$, a total of N_x data points will be sampled symmetrically about $k_x = 0$, as illustrated in **Fig. 2.2**. This corresponds to the coverage of $-\gamma G_R(t_2 - t_1)$ to $\gamma G_R(t_2 - t_1)$ in k_x direction (2). The other data points in k-space are sampled similarly, by varying G_s and G_p (hence k_y and k_z) in following RF excitations. The duration between the two RF excitations is the repetition time, TR.

Note that, the sequence shown in **Fig. 2.1** is a simplified gradient echo sequence. For SWI and QSM data acquisition, flow compensation gradients in slab select, partition encoding, phase encoding and readout directions are usually required, in order to reduce the dephasing effects caused by flow (1,2). The sequence diagram of a 3D gradient echo sequence with full flow-compensation is shown in **Fig. 2.3** (2). Before the excitation by the next RF pulse, in the end of the acquisition during one RF excitation, there may be remnant transverse magnetization, which can be destructed through spoiling. This is achieved by keeping the gradient in the readout direction on to properly dephase the remnant transverse magnetization (i.e., gradient spoiling), and by changing the offset angle of the following RF pulse by 117^o (i.e., RF spoiling) (2). Considering the relaxation effects, for a particular voxel with several isochromats, the steady-state signal for the spoiled gradient echo sequence can be written as (1,2):

$$\hat{\rho}(\theta, TE) = \rho_0 sin\theta \frac{1-E_1}{1-E_1 cos\theta} e^{-TE/T_2^*} \quad [2.11],$$

where $\rho_0$is the voxel spin density and $E_1 = e^{-TR/T_1}$.

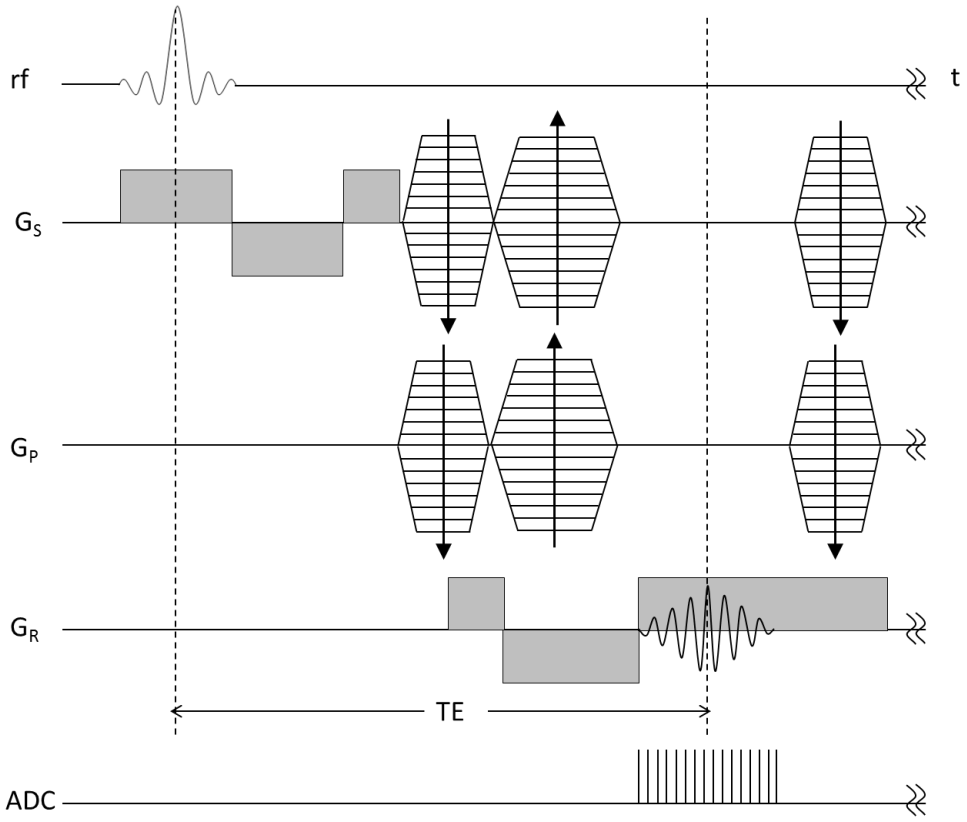

Figure 2.3 Sequence diagram of a single echo 3D gradient echo sequence with flow-compensation in all directions. G_S: slab selection/partition encoding gradient; G_P: phase encoding gradient; G_R: readout gradient.

However, the sequences shown in **Figs. 2.1** and **2.3** are single echo gradient echo sequences. For multi-echo gradient echo sequence, within one RF excitation, the gradients with the same settings can be used again to sample the same line in k-space, but with different echo time (1,3,4).

When there are inhomogeneities in the main magnetic field, at t=TE, with any flow induced effects compensated, the accumulated phase for a right-handed system can be written as (1,2):

$$\phi(\vec{r}, TE) = -\gamma \Delta B(\vec{r}) \cdot TE + \phi_0(\vec{r}) \quad [2.12],$$

where $\phi_0(\vec{r})$ is the time-independent phase offset, related to local conductivity and permittivity (5). The field variation $\Delta B(\vec{r})$ is induced by inhomogeities of the main magnetic field, susceptibility differences in the tissues in the human body and chemical-shift. Particularly, the field variation induced by the susceptibility differences can be predicted through a forward calculation.

2.2 Predicting field variation through forward calculation

As a basic tissue property and important source of imaging contrast, magnetic susceptibility describes the ability of the material to get magnetized when exposed to an external magnetic field (1,2). It is also a measure of how materials change the local magnetic field (2). Based on their induced magnetization, the materials can be categorized as paramagnetic, diamagnetic and ferromagnetic materials. For paramagnetic materials, the induced magnetic moments align parallel with the external magnetic field, while for diamagnetic materials the induced moments align anti-parallel with the external field. For ferromagnetic materials, a magnetic field exists even without the external field (2).

When an object with susceptibility χ is placed in an external magnetic field

$$\vec{B} = \mu \vec{H}, \quad [2.13],$$

where μ is the permeability and $\vec{H}$ (in A/m) is the applied field (1). The actual field inside the object can be written as:

$$\vec{B} = \mu_0(\vec{H} + \vec{M}) \quad [2.14],$$

where $\mu_0 = 4\pi \cdot 10^{-7}$Wb/(A·m) is the permeability of vacuum, and $\vec{M}$ is the induced magnetization, which is related to the H-field through:

$$\vec{M} = \chi\vec{H} \quad [2.15].$$

χ is the magnetic susceptibility. For paramagnetic materials, χ is positive; for diamagnetic materials, χ is negative. In studies on biological tissues such as brain tissues, the reference of susceptibility is usually taken to be the susceptibility of soft tissue or water, with the susceptibility of water being approximately -9 ppm relative to vacuum. Thus, being "paramagnetic" or "diamagnetic" in this thesis, essentially means that being less diamagnetic (paramagnetic relative to water) or more diamagnetic than water (i.e. diamagnetic relative to water) (2,6).

From Eqs. 2.14 and 2.15, assuming that $\chi \ll 1$,

$$\vec{B} = \mu_0(1+\chi)\vec{H} = \mu_0\left(1+\frac{1}{\chi}\right)\vec{M} \approx \mu_0\vec{M}/\chi \quad [2.16].$$

A dipole field will be generated due to the induced magnetization $\vec{M}$. Assuming that the external magnetic field is in the z direction, only the z-components of the dipole field and $\vec{M}$ are important (6–8). This z-component of the field variation can be written as (6–8):

$$\Delta B_z(\vec{r}) = \frac{\mu_0}{4\pi}\int_{V'} d^3r'\left\{\frac{3M_z(\vec{r}')(z-z')^2}{|\vec{r}-\vec{r}'|^5} - \frac{M_z(\vec{r}')}{|\vec{r}-\vec{r}'|^3}\right\} \quad [2.17]$$

Eq. 2.17 can be written as a convolution process (9):

$$\Delta B_z(\vec{r}) = \mu_0 M_z(\vec{r}) * G(\vec{r}) \quad [2.18].$$

The 3D Green's function $G(\vec{r})$ is:

$$G(\vec{r}) = \frac{1}{4\pi} \cdot \frac{3\cos^2\theta - 1}{r^3} \quad [2.19],$$

where θ is the angle subtended by a position vector, relative to the z direction in 3D spherical coordinate system(6–8). Particularly, $\cos^2\theta = \frac{z^2}{r^2}$.

From Eqs. 2.16 to 2.19, given the susceptibility distribution, the induced magnetic field variation can be predicted as:

$$\Delta B_z(\vec{r}) = \mu_0 M_z(\vec{r}) * G(\vec{r}) \approx B_0 \chi(\vec{r}) * G(\vec{r}) \quad [2.20].$$

The convolution in Eq. 2.20 can be efficiently calculated in Fourier domain as:

$$\Delta B_z(\vec{r}) = B_0 \cdot FT^{-1}\{FT[\chi(\vec{r})] \cdot FT[G(\vec{r})]\} \quad [2.21],$$

where FT and FT^{-1}represents the Fourier transform and the inverse Fourier transform, respectively.

It can be shown that the Fourier transform of the Green's function is (6–8):

$$G(\vec{k}) = FT[G(\vec{r})] = \begin{cases} 1/3 - \frac{k_z^2}{k_x^2 + k_y^2 + k_z^2}, & for\ \vec{k} \neq 0 \\ 0, & for\ \vec{k} = 0 \end{cases} \quad [2.22].$$

Given a susceptibility distribution, the induced field variation can be predicted using Eqs. 2.20 to 2.22. This process is referred to as the "forward calculation".

2.3 Quantifying Susceptibility as an inverse problem

The field variation $\Delta B_z(\vec{r})$ can be extracted from $\phi(\vec{r})$, using Eq. 2.12, and susceptibility distribution $\chi(\vec{r})$ can be calculated using $\Delta B_z(\vec{r})$ through Eqs. 2.20 to 2.22. In practice, however, susceptibility quantification is composed of several steps. The QSM data processing procedures are illustrated in **Fig. 2.4**.

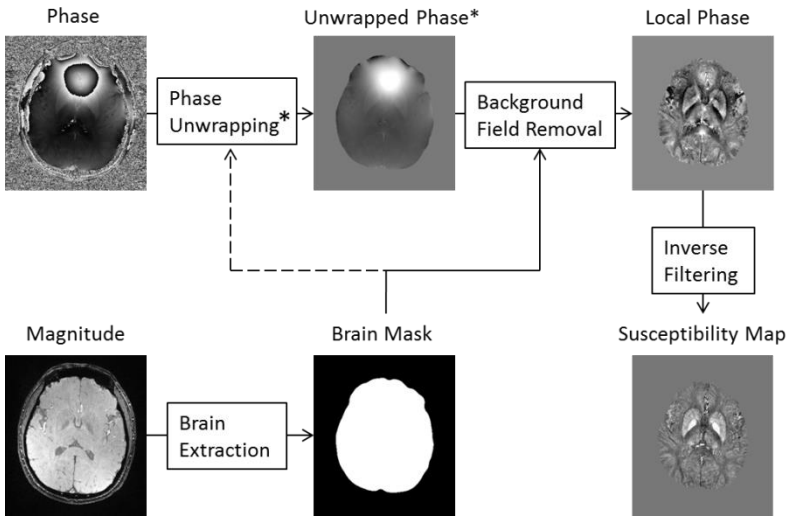

Figure 2.4 QSM data processing procedures. The dashed line indicates that brain masks may not be required for phase unwrapping. The * indicates that the phase unwrapping step can be avoided in certain algorithms and the unwrapped phase is not required for background field removal.

Susceptibility quantification is an ill-posed inverse problem, due to the zeros in $G(\vec{k})$ along the magic angles in the Fourier domain. This inverse problem could be solved through either truncated k-space division (10–12) or other optimization methods (13–16). For the former approach, a regularized inverse filter is used, defined as:

$$G'^{-1}(\vec{k}) = \begin{cases} \left(\frac{1}{3} - \frac{k_z^2}{k^2}\right)^{-1}, & for\ \left|\frac{1}{3} - \frac{k_z^2}{k^2}\right| > th \\ sgn\left(\frac{1}{3} - \frac{k_z^2}{k^2}\right)\left(\frac{1}{3} - \frac{k_z^2}{k^2}\right)^2 th^{-3}, & for\ \left|\frac{1}{3} - \frac{k_z^2}{k^2}\right| \leq th. \end{cases} \quad [2.23],$$

and $\chi(\vec{r})$ can be calculated as:

$$\chi(\vec{r}) = FT^{-1}\{G'^{-1}(\vec{k})FT[\Delta B_z(\vec{r})]\}/B_0 \quad [2.24].$$

In other approaches, $\chi(\vec{r})$ is obtained as:

$$argmin_{\chi(\vec{r})}\{\left\|W\left(\Delta B_z(\vec{r}) - \chi(\vec{r}) * G(\vec{r})\right)\right\|_2^2 + \lambda \cdot R(\chi)\} \quad [2.25],$$

where W is a weighting function which is related to the signal-to-noise ratio (SNR) of the data and $R(\chi)$ is the regularization term. λ is a parameter which controls the trade-off between data fidelity and data regularization (13,17).

In addition, the original phase images are usually aliased. The value range of the original phase images is from –π to π. However, the true value of phase may be outside this range and will be wrapped back into the range of –π to π. This wrapping process can be described as:

$$\phi_{wrapped}(\vec{r}) = \phi_{true}(\vec{r}) + 2\pi \cdot n(\vec{r}) \quad [2.26],$$

where the values of the function $n(\vec{r})$ are integers. In order to obtain $\Delta B_z(\vec{r})$ from the phase images without discontinuities, $\phi_{true}(\vec{r})$ is generated normally through phase unwrapping, in which the function $n(\vec{r})$ is determined.

Furthermore, the original phase information is contaminated by the background field inhomogeneities induced by the air-tissue interfaces. The background field can be removed with appropriate filtering of the data (18,19). The resulting local phase information will be used to calculate susceptibility maps by solving the inverse problem. More details on removing the background field and solving the inverse problem are provided in later chapters.

2.4 Susceptibility and its relations to venous oxygen saturation and iron content

One of the important applications of susceptibility mapping is measuring venous oxygen saturation *in vivo*. Blood can be modeled using two compartments: the plasma and the red blood cells. The susceptibility of the blood system can be written as (1,2):

$$\chi_{blood} = Hct \cdot \left(Y \cdot \chi_{oxy} + (1-Y) \cdot \chi_{deoxy}\right) + (1-Hct) \cdot \chi_{plasma} \qquad [2.27],$$

where *Hct* is the fractional hematocrit, defined as the volume fraction of the red blood cells in blood. The normal value of *Hct* is around 0.45 for men and 0.4 for women (1,2). *Y* is the oxygenation level. χ_{oxy} and $\chi_{deoxy}$are the susceptibilities of fully oxygenated and fully deoxygenated red blood cells, respectively. Using Eq. 2.27, the susceptibility difference between the venous blood (with 0<Y<1) and the fully oxygenated blood (Y=1) can be written as:

$$\chi_v - \chi_{Y=1} = \chi_{do} \cdot (1-Y) \cdot Hct \qquad [2.28],$$

where χ_{do} is the susceptibility difference between fully deoxygenated and fully oxygenated red blood cells, which is approximately $4\pi \cdot 0.27$ ppm per unit *Hct* (2,20,21). Assuming that the susceptibility of fully oxygenated blood is the same as the susceptibility of the surrounding tissue, the difference between the susceptibility of venous blood and the surrounding tissue, $\Delta\chi_v$, can be approximated using Eq. 2.28. Particularly, with *Hct*=0.44, *Y*=70%, $\Delta\chi_v$ is found to be close to 0.45ppm. It is this susceptibility difference that induces the field variation and the phase of the veins.

Apart from measuring venous oxygen saturation, various studies have been performed to study the relation between the measured susceptibility and the iron content. Note that, since the susceptibility maps only provide a relative measure, it is only the slope between the measured susceptibility and iron content that can be determined. For ferritin, when the iron content was measured by Inductively Coupled Plasma Mass Spectrometry (ICP-MS) (22) and X-ray fluorescence (XRF) (23), the slope was found to be 1.1 ppb per μg iron/g wet tissue (23). For the deep grey matter structures in cadaveric brain, however, the slope was found to be 0.8 ppb per μg iron/g wet tissue, with iron measured using XRF (23). The smaller slope found in cadaveric brain than the one found in ferritin phantom was attributed to invisible forms of iron in the cadaveric brain and signal loss or bias caused by the QSM data processing (22,23). Indeed, due to the singularities of the inverse kernel, regularization is required and is known to cause under-estimation of the susceptibility. More importantly, the quality and accuracy of QSM is largely dependent on the extraction of local phase information and hence the efficacy of the background field removal.

References

1. Haacke EM, Brown RW, Thompson MR, Venkatesan R. Magnetic Resonance Imaging: Physical Principles and Sequence Design. 1st ed. Wiley-Liss; 1999.
2. Haacke EM, Reichenbach JR, editors. Susceptibility Weighted Imaging in MRI: Basic Concepts and Clinical Applications. 1st ed. Wiley-Blackwell; 2011.
3. Bernstein MA, King KF, Zhou XJ, editors. Chapter 11 - Signal Acquisition and k-Space Sampling (Internet). In: Handbook of MRI Pulse Sequences. Burlington: Academic Press; 2004 (cited 2014 Jan 22). page 367–442.Available from: http://www.sciencedirect.com/science/article/pii/B9780120928613500170
4. Ye Y, Hu J, Wu D, Haacke EM. Noncontrast-enhanced magnetic resonance angiography and venography imaging with enhanced angiography. J. Magn. Reson. Imaging 2013;38:1539–48.
5. Haacke EM, Petropoulos LS, Nilges EW, Wu DH. Extraction of conductivity and permittivity using magnetic resonance imaging. Phys. Med. Biol. 1991;36:723.
6. Marques J p., Bowtell R. Application of a Fourier-based method for rapid calculation of field inhomogeneity due to spatial variation of magnetic susceptibility. Concepts Magn. Reson. Part B Magn. Reson. Eng. 2005;25B:65–78.
7. Koch KM, Papademetris X, Rothman DL, de Graaf RA. Rapid calculations of susceptibility-induced magnetostatic field perturbations for in vivo magnetic resonance. Phys. Med. Biol. 2006;51:6381–402.
8. Cheng Y-CN, Neelavalli J, Haacke EM. Limitations of calculating field distributions and magnetic susceptibilities in MRI using a Fourier based method. Phys. Med. Biol. 2009;54:1169–89.
9. Deville G, Bernier M, Delrieux JM. NMR multiple echoes observed in solid ^{3}He. Phys. Rev. B 1979;19:5666–88.
10. Shmueli K, de Zwart JA, van Gelderen P, Li T, Dodd SJ, Duyn JH. Magnetic susceptibility mapping of brain tissue in vivo using MRI phase data. Magn. Reson. Med. 2009;62:1510–22.
11. Haacke EM, Tang J, Neelavalli J, Cheng YC. Susceptibility mapping as a means to visualize veins and quantify oxygen saturation. J. Magn. Reson. Imaging 2010;32:663–76.
12. Schweser F, Deistung A, Sommer K, Reichenbach JR. Toward online reconstruction of quantitative susceptibility maps: superfast dipole inversion. Magn. Reson. Med. 2013;69:1582–94.
13. Liu J, Liu T, de Rochefort L, Ledoux J, Khalidov I, Chen W, et al. Morphology enabled dipole inversion for quantitative susceptibility mapping using structural consistency between the magnitude image and the susceptibility map. NeuroImage 2012;59:2560–8.
14. Schweser F, Sommer K, Deistung A, Reichenbach JR. Quantitative susceptibility mapping for investigating subtle susceptibility variations in the human brain. NeuroImage 2012;62:2083–100.
15. Wu B, Li W, Guidon A, Liu C. Whole brain susceptibility mapping using compressed sensing. Magn. Reson. Med. 2012;67:137–47.

16. Tang J, Liu S, Neelavalli J, Cheng YCN, Buch S, Haacke EM. Improving susceptibility mapping using a threshold-based K-space/image domain iterative reconstruction approach. Magn. Reson. Med. 2013;69:1396–407.
17. De Rochefort L, Brown R, Prince MR, Wang Y. Quantitative MR susceptibility mapping using piece-wise constant regularized inversion of the magnetic field. Magn. Reson. Med. 2008;60:1003–9.
18. Liu T, Khalidov I, de Rochefort L, Spincemaille P, Liu J, Tsiouris AJ, et al. A novel background field removal method for MRI using projection onto dipole fields (PDF). NMR Biomed. 2011;24:1129–36.
19. Schweser F, Deistung A, Lehr BW, Reichenbach JR. Quantitative imaging of intrinsic magnetic tissue properties using MRI signal phase: An approach to in vivo brain iron metabolism? NeuroImage 2011;54:2789–807.
20. He X, Yablonskiy DA. Biophysical mechanisms of phase contrast in gradient echo MRI. Proc. Natl. Acad. Sci. U. S. A. 2009;106:13558–63.
21. Jain V, Langham MC, Wehrli FW. MRI estimation of global brain oxygen consumption rate. J. Cereb. Blood Flow Metab. 2010;30:1598–607.
22. Langkammer C, Schweser F, Krebs N, Deistung A, Goessler W, Scheurer E, et al. Quantitative susceptibility mapping (QSM) as a means to measure brain iron? A post mortem validation study. NeuroImage 2012;62:1593–9.
23. Zheng W, Nichol H, Liu S, Cheng YCN, Haacke EM. Measuring iron in the brain using quantitative susceptibility mapping and X-ray fluorescence imaging. NeuroImage 2013;78:68–74.

Chapter 3 Background Field Removal

3.1 The background field

Phase information is proportional to the product of field variation and echo time (TE) (1,2). For a right-handed system, the phase $\phi(\vec{r})$ is related to the total field variation $\Delta B(\vec{r})$ as:

$$\phi(\vec{r}) = -\gamma \Delta B(\vec{r}) TE + \phi_0(\vec{r}) \quad [3.1],$$

where $\phi_0(\vec{r})$ is the phase offset at TE=0. As mentioned in the earlier chapter, the original phase images are usually aliased and phase unwrapping should be performed in order to obtain $\Delta B(\vec{r})$ using Eq. 3.1. The field variation $\Delta B(\vec{r})$ can be considered as a combination of two parts (3–6): the background field $\Delta B_b(\vec{r})$ and the local field $\Delta B_l(\vec{r})$:

$$\Delta B(\vec{r}) = \Delta B_b(\vec{r}) + \Delta B_l(\vec{r}) \quad [3.2].$$

In quantitative susceptibility mapping, it is the local field variation $\Delta B_l(\vec{r})$ that is of interest. The background field is induced by the main magnetic field inhomogeneity and the air-tissue interfaces which have a susceptibility difference of approximately 9.4 ppm relative the brain tissue (4). This is much higher than the susceptibility differences (<1ppm) of the local tissues inside the brain (4–7). At most realistic echo times, this large

field variation leads to phase aliasing, further complicating the problem of background field removal. Another complication occurs in the presence of a local background gradient which will cause a shift of the echo center in k-space which, in turn, induces a linear phase shift in the image domain (1). This can be easily understood through the Fourier shift theorem. For example, if the center of the echo is shifted in k_x by Δk, a linear phase component with gradient $2\pi\Delta k \cdot x/N$ will be created in the image domain. This linear phase component can be easily removed by detecting the position of the signal center (peak value) in k-space and shifting the k-space data such that the signal center occurs at the actual center of k-space (1).

To remove the background field, various algorithms have been proposed. There are mainly four types of methods: geometry dependent artefact correction (GDAC) (4), (homodyne) high-pass filtering (8–10), spherical mean value filtering (3,6,7) and dipole field fitting (5), all with different assumptions of the background field.

If the geometries and susceptibility distributions of the air-tissue interfaces were known, the field variation induced by the air-tissue interfaces could be predicted using the fast forward field calculation (4). Assuming that the susceptibility differences of these air/bone-tissue interfaces are $\Delta\chi_i(\vec{r})$ for the i^{th} interface, with i ranging from 1 to n, the induced field variation can be calculated as:

$$\Delta B_b(\vec{r}) = B_0 \Sigma_{i=1}^{n} (G(\vec{r}) * \Delta X_i(\vec{r})) \qquad [3.3].$$

The geometry of the sinuses can be extracted from the T_1 weighted magnitude image, and the susceptibilities of different sinuses can be found through least squares fitting using

phase images without wraps (4). This method has been shown to effectively reduce the background field. However, obtaining the exact geometries and susceptibility distributions of the air/bone-tissue interfaces, such as the air sinuses in the head, is quite challenging. This is partly solved by assuming constant susceptibilities inside the sinuses. Recently, a method of using short TE's data was proposed, which produce susceptibility maps for the air sinuses and bone structures (11). This can potentially solve the remnant problems of geometry dependent artefact correction.

In the other background field removal algorithms, the background field is reduced, or separated from the local field, without knowing the exact geometries or susceptibility distributions of the air-tissue interfaces. These filtering methods are discussed in following sections. Note that, since phase is a linear function of field variation, as shown in Eq. 3.1, the filters discussed in this thesis are operated directly on the (unwrapped) phase images rather than the field maps.

3.2 Homodyne high-pass filter

3.2.1 Theory

Homodyne high-pass filtering is the traditional way for background field suppression (10). It is widely used in susceptibility weighted imaging (SWI), due to its robustness and effectiveness. It makes use of the fact that the background field has relatively low spatial frequency. Consequently, the background field can be reduced through high-pass filtering. In homodyne high-pass filtering, low-pass filtered data are created by applying Hanning window to the central part of k-space (2,12).

$$\hat{\rho}_{lp} = FT^{-1}\{FT[\hat{\rho}] \cdot Hann\} \quad [3.4],$$

Where $\hat{\rho} = mag \cdot e^{i\cdot\phi}$ is the original complex data and $Hann$ is a zero-filled 2D Hanning window defined as:

$$Hann(k_x, k_y) = \begin{cases} \frac{1}{4}\left[1 - \cos\left(\frac{2\pi\left(k_x + \frac{N_x}{2}\right)}{N_x}\right)\right]\left[1 - \cos\left(\frac{2\pi\left(k_y + \frac{N_y}{2}\right)}{N_y}\right)\right], \\ \qquad for -\frac{N_x}{2} \le k_x \le \frac{N_x}{2} - 1, -\frac{N_y}{2} \le k_y \le \frac{N_y}{2} - 1 \\ 0, \ \ for\ k_x < -\frac{N_x}{2}\ or\ k_x > \frac{N_x}{2} - 1, k_y < -\frac{N_y}{2}\ or\ k_y > \frac{N_x}{2} - 1 \end{cases} \quad [3.5].$$

Then the low-pass filtered data, $\hat{\rho}_{lp}$, are complex divided into the original complex data $\hat{\rho}$, to produce high-pass filtered complex data $\hat{\rho}_{hp}$. The high-pass filtered phase images, ϕ_{hp}, are generated as:

$$\phi_{hp} = arg(\hat{\rho}_{hp}) = arg(\hat{\rho}/\hat{\rho}_{lp}) \quad [3.6],$$

where "/" represents pixel-wise division. The whole process of homodyne high-pass filtering is shown in **Fig. 3.1**.

One advantage of homodyne high-pass filtering is that no phase unwrapping is required. This is due to the use of the complex data in the high-pass filtering. On the other hand, the phase images can also be unwrapped first and then a high-pass filter can be applied in the image domain, e.g., applying a Gaussian or boxcar window function to the unwrapped phase images (2). Both the homodyne high-pass filtering and image domain high-pass filtering have edge artefacts, since there is low/no reliable signal outside the brain.

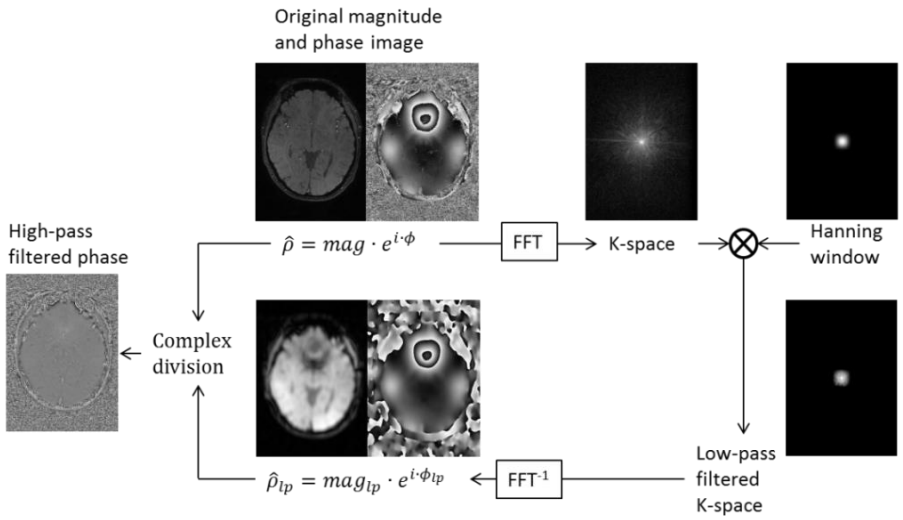

Figure 3.1 Illustration of the processing steps in homodyne high-pass filtering.

3.2.2 Effects of object orientation in homodyne high-pass filtering

Homodyne high-pass filtering has been used successfully in SWI, especially for venography, in which the objects of interest are the veins. However, high-pass filtering also leads to signal loss, especially for objects with relatively large size, such as those basal ganglia structures. This will cause underestimation of the susceptibility of those basal ganglia structures (2,13). Apart from the filter size, the accuracy of homodyne high-pass filtering is also dependent on the direction along which the high-pass filter is applied, since the homodyne high-pass filter is typically applied in 2D. This may lead to different levels of signal loss to structures with different orientation (14).

In order to study the effect of homodyne high-pass filtering, phase images of cylinders and spheres with different radii were simulated in a 256×256×256 matrix, with B=3T, TE=20ms. The cylinders were used as a surrogate for veins, and spheres for microbleeds.

The susceptibilities inside the cylinders and spheres were set to 0.45ppm and 1ppm, respectively. The radii of the cross section of the cylinders range from 1 to 32 pixels. The radii of the spheres are in the same range. For the cylinders, the long axis was set to be 30, 45, 60, and 90 degrees with respect to the main field direction. Homodyne high-pass filter with different sizes were applied to the cylinders in 90^o with respect to the main field direction, in order to show the effects of filter size. Next, to show the effects of orientation of the object, homodyne high-pass filter with size 32×32 were applied in axial, coronal and sagittal views of the phase images of cylinders and spheres. Susceptibility maps were generated using truncated k-space division (15), with a k-space threshold of 0.1, using both the original and filtered phase images. Mean susceptibility values were measured for the regions inside the cylinders and spheres.

The relative errors in susceptibilities as a function of object size for different filter sizes, for cylinders perpendicular to the main magnetic field are shown in **Fig.3.2.a**. As expected, the larger the filter size, the greater the signal loss and hence the greater the underestimation in the estimated susceptibility values.

The relative errors plotted in **Fig. 3.2.b** to **3.2.f** are dependent on the object and filtering orientations. For cylinders, the least error in the estimated susceptibilities was obtained when the HP filter was applied in the direction which is perpendicular to the long axis of the cylinder. For example, in **Fig. 3.2.b**, the cylinders were aligned along the x direction. When the HP filter is applied to the view perpendicular to the long axis of the cylinders (the y-z view of the dataset), the errors were smaller than HP filtering in other views. For the 30^o, 45^o and 60^o cases, none of the slice orientations were perpendicular to the long

axis of the cylinders. Hence varying error profiles were observed for each case, as shown in **Fig. 3.2.c** to **3.2.e**. For these cases, the least errors in the estimated susceptibilities were obtained when the HP filter was applied in the orientation which is closest to be perpendicular to the long axis of the cylinder. This can be seen from **Fig. 3.2.c** and **3.2.e**. In **Fig. 3.2.c**, the least error is obtained when the HP filter is applied to the sagittal view, while in **Fig. 3.2.d** to the coronal view.

When the angle between the long axis of the cylinders and the field direction is 45^{o}, as would be expected, both axial and coronal views give the same error profile (**Fig. 3.2.d**). This relation between errors in susceptibility estimation and HP filtering orientation was further confirmed by **Fig. 3.2.f**, in which the errors for spheres were independent to the filtering orientation.

2D homodyne high-pass filtering, which is currently used in SWI data processing, leads to orientation-dependent errors to the estimated susceptibilities of cylinders. Consequently, when the homodyne high-pass filtering was used in the quantification of susceptibilities of veins, the orientation of the filtering with respect to the veins should be considered. This orientation dependence can be potentially removed by using a 3D homodyne high-pass filter. For data collected which were already filtered using a 2D homodyne high-pass filter, an additional homodyne high-pass can be applied in the through-plane direction, to form an effective 3D high-pass filtering.

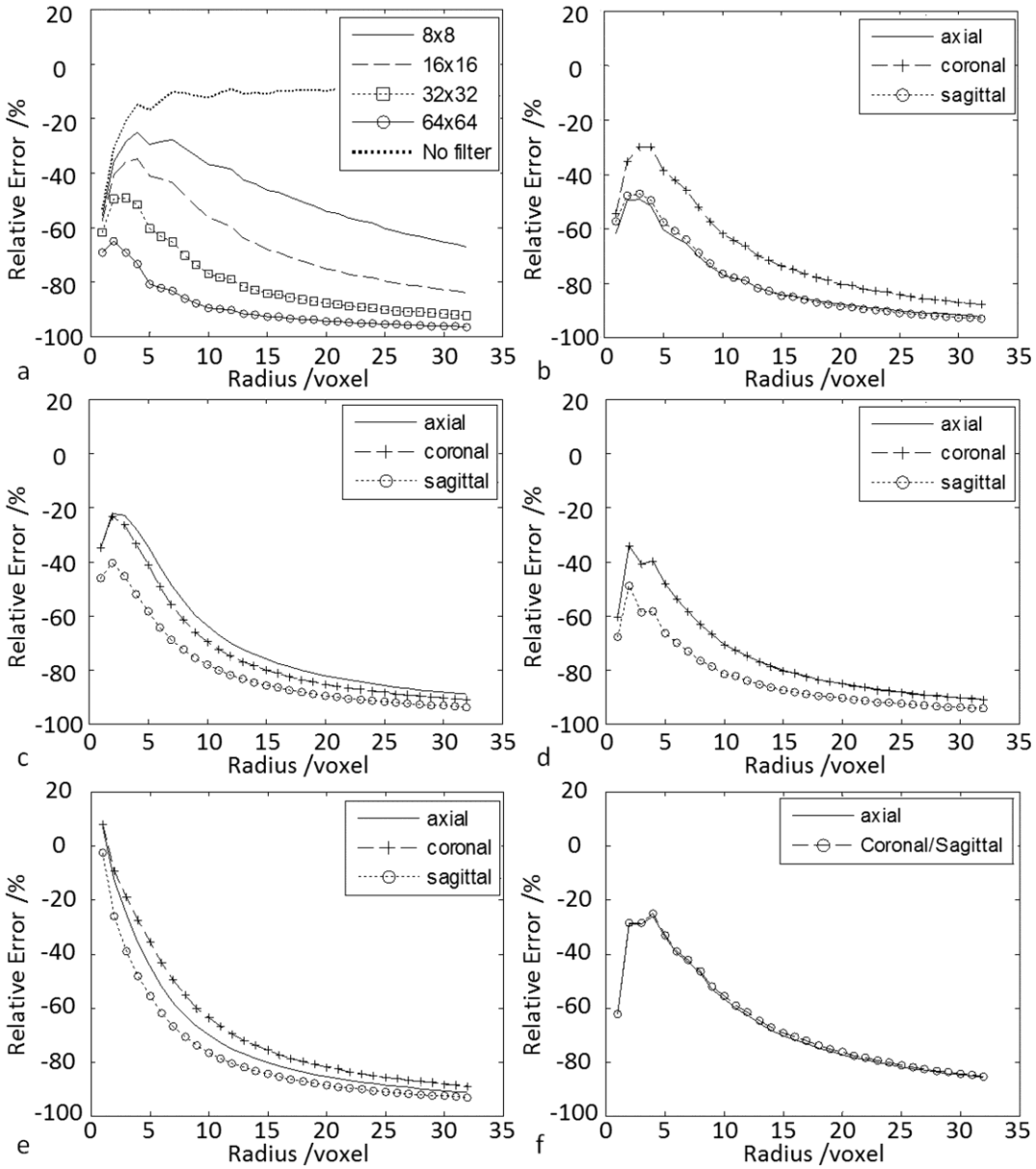

Figure 3.2 Relative error in estimated susceptibilities induced by high-pass filtering in different orientations. The relative errors induced by homodyne high-pass filtering with different sizes, for cylinders in the 90^o case, are shown in **a**. **b** to **e** show the effects of the orientation of high-pass filtering for cylinders in the 90^o case (**b**), in the 30^o case (**c**), in the 45^o case (**d**), and in the 60^o case (**e**). Relative errors for the spheres are shown in **f**.

3.3 Variable high-pass filter (VHP)

3.3.1 Theory

It is known that homodyne high-pass filtering leads to signal loss and underestimation of the susceptibilities of structures with relatively large sizes, such as the basal ganglia structures. In fact, variable filter sizes can be used for different regions of the brain (16). The main idea is to apply mild filtering to the central part of the brain, where most of the relatively large structures are located, and to apply stronger filtering to the periphery of the brain, especially to the regions close to the air sinuses, where the background field has relatively higher spatial frequency.

A major advance in this area of research on background field removal occurred, when it was recognized that the background field can be considered as a harmonic function inside the brain (3,6). Using the mean value property of harmonic functions,

$$\Delta B_b(\vec{r}) * s = \Delta B_b(\vec{r}) \quad [3.7],$$

where "s" is a normalized sphere with uniform values and the sum of all the values of the pixels inside the sphere equals 1. "*" represents the convolution operation. From Eqs. 3.2 and 3.7,

$$\Delta B(\vec{r}) * s = \Delta B_b(\vec{r}) * s + \Delta B_l(\vec{r}) * s = \Delta B_b(\vec{r}) + \Delta B_l(\vec{r}) * s \quad [3.8].$$

Eq. 3.8 can also be viewed as a low-pass filtering process using a spherical symmetric window function, s. Next, the background field could be removed by subtracting the low-pass filtered field map from the original field map:

$$\Delta B_{HP}(\vec{r}) = \Delta B(\vec{r}) - \Delta B(\vec{r}) * s = \Delta B_l(\vec{r}) * (\delta - s) \quad [3.9],$$

where δ is the delta function.

However, using the above equation, the regions within a distance of *R* to the edge of the brain do not have correct convolution results (6,7), where *R* is the radius of the spherical kernel. Those regions will be set to 0 using a 3D eroded mask. To reduce the area of the lost regions, we applied spherical kernels with variable size, similar to the strategy used in (7). Specifically, for the periphery region of the brain, the size of the kernel at certain pixel is chosen to be the distance from that pixel to the nearest edge pixel of the brain. While for the central region of the brain, a large kernel with constant size was applied. This is essentially a high-pass filtering process, and is referred to as variable high-pass filtering (VHP) in this thesis.

The procedures of variable high-pass filtering are as follows:

1. Preprocessing: generate $\phi_{uw}(\vec{r})$ through phase unwrapping; obtain the brain masks $M(r)$ defining the region inside the brain.

2. Spherical averaging: apply the normalized spherical kernels with different radii to $\phi_{uw}(\vec{r})$. $\phi_{LP}(\vec{r})$ will be produced by combining the results generated using different spherical kernels.

3. High-pass filtering: $\phi_{HP}(\vec{r})$ will be generated as $\phi_{HP}(\vec{r}) = \phi_{uw}(\vec{r}) - \phi_{LP}(\vec{r})$.

3.3.2 Evaluating the accuracies of VHP using a simulated brain model

Brain model data simulation

In order to evaluate the accuracy of VHP, phase images of a 3D brain model were simulated using the forward field calculation (17,18), at B_0=3T, TE=10ms. The background field variation induced by these air-tissue interfaces were introduced by setting the susceptibility of the air sinuses to 9.4 ppm. Different susceptibility values were set to different brain structures. The phase induced by the brain structures $\phi_{l,sim}$ (the local phase) and the phase induced by the sinuses $\phi_{b,sim}$ (the background phase) were calculated independently. Then the phase images of the brain model (ϕ_{sim}) were generated by taking the sum of these two components. The magnitude images were assumed to be constant. White Gaussian noise was added to real and imaginary parts of the complex data, and the SNR in the final magnitude images was 10:1. This is equivalent to Gaussian noise with standard deviation 0.1 radians in phase images (1,19). The brain masks were generated which covers all the structures inside the brain. A reference region was obtained by eroding the brain masks 16 pixels. This reference region was used to calculate the root-mean-square-error (RMSE) in the processed phase images and in the generated susceptibility maps. The simulated phase images and the binary masks are shown in **Fig. 3.3**.

The simulated phase images with background phase component and random noise were processed using VHP with largest spherical kernel radius 32 pixels and smallest spherical kernel radius 1 pixel. The processed phase images were compared with the simulated

phase of the structures inside the brain ($\phi_{l,sim}$), without any background phase or random noise. Root-mean-square-error (RMSE) was calculated for the reference region as:

$$RMSE = \sqrt{\Sigma\left(\phi_{processed} - \phi_{l,sim}\right)^2 / N_{total}} \quad [3.10],$$

where N_{total} is the total number of pixels in the reference region.

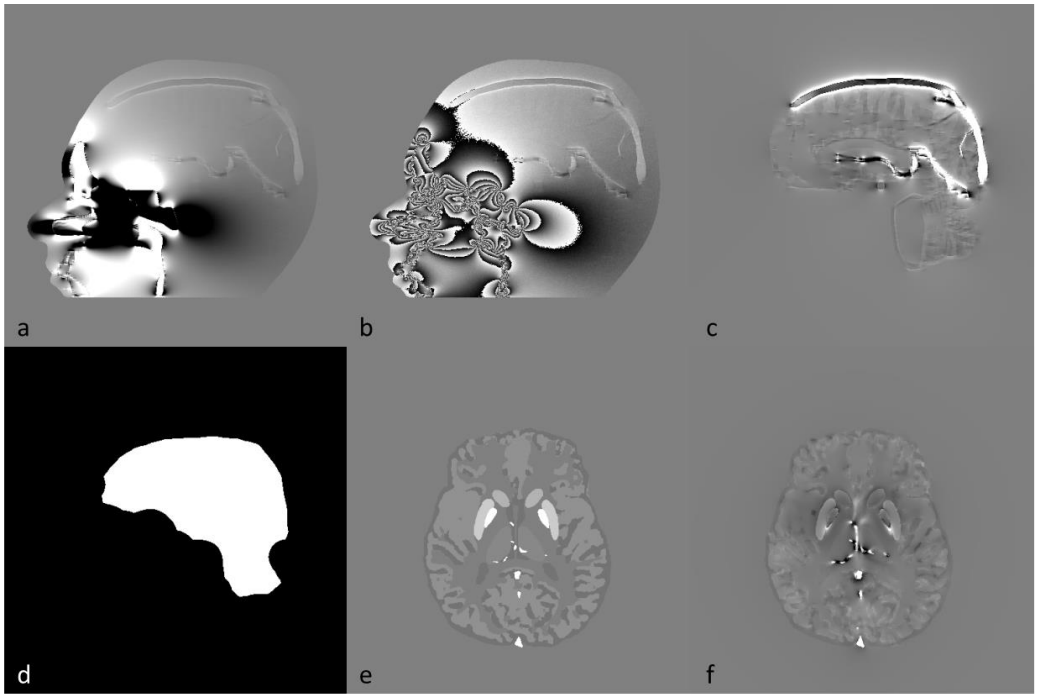

Figure 3.3 a). Simulated phase image with background phase but without random noise. **b)**. Simulated phase with background phase and random noise. **c)**. The local phase information without random noise. This is used as the true answer to evaluate the accuracies of the processed phase images. **d)**. The reference region used for calculating the RMSEs in the processed phase images. **e)**. The susceptibility map in axial view. **f)**. The phase image corresponds to **e**.

In order to evaluate the accuracy of susceptibility quantification using VHP processed phase images, susceptibility maps were generated using the truncated k-space division approach (15). The mean susceptibility values were measured for a total of 9 structures, as listed in **Table 3.3**. The relative error in the susceptibility quantification of each structure was calculated as: $(\chi_{mean} - \chi_{true})/|\chi_{true}|$, where $\chi_{mean}$is the measured mean susceptibility value and $\chi_{true}$is the true susceptibility value of certain structure. However, this error is a combination of both the errors caused by background field removal and the errors by the truncated k-space division susceptibility mapping algorithm. To analyze the error purely caused by background field removal, reference susceptibility maps were generated with the same algorithm using the phase images with ideal background field removal, i.e., the local brain structures induced phase with random noise.

Simulated data results

As expected, both the RMSEs of the processed phase image and the susceptibility maps reduce as the radius of the spherical kernel increases, as shown in **Fig. 3.4**. This can be understood as a reduction of signal loss related directly to an increase in the size of the spherical kernel in image domain. The results shown in **Fig. 3.4** correspond to the global errors.

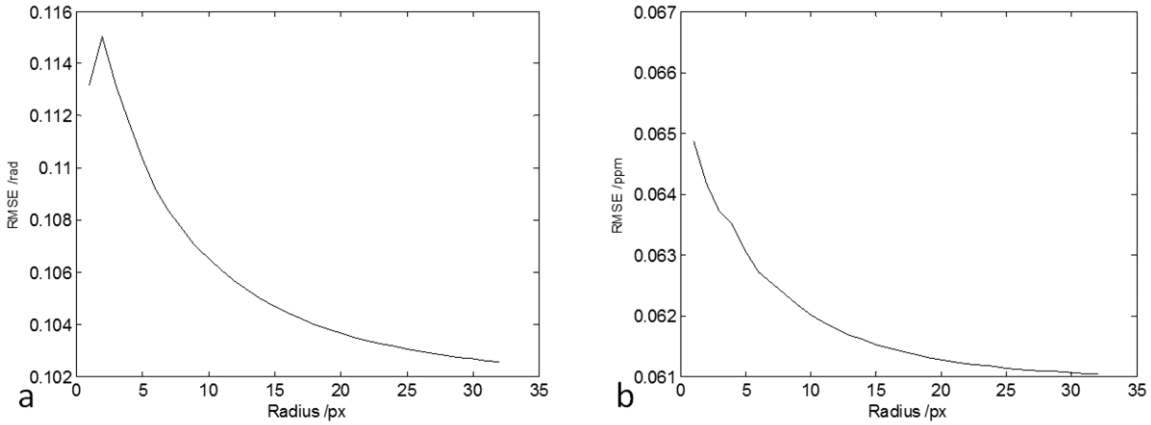

Figure 3.4 Overall RMSEs of the processed phase images (**a**) and susceptibility maps (**b**) generated using VHP.

The relative errors in the susceptibility maps for different structures are plotted in **Fig. 3.5**. For small structures such as veins, as the radius of the spherical kernel increases, the relative error reduces much faster than for other bigger structures such as the globus pallidus. Compared with the error in the susceptibilities estimated from the original phase (as indicated by the dashed lines in **Fig. 3.5**), when variable high-pass filtering was applied, the additional under-estimation could be around 20% to 30% for big structures such as putamen.

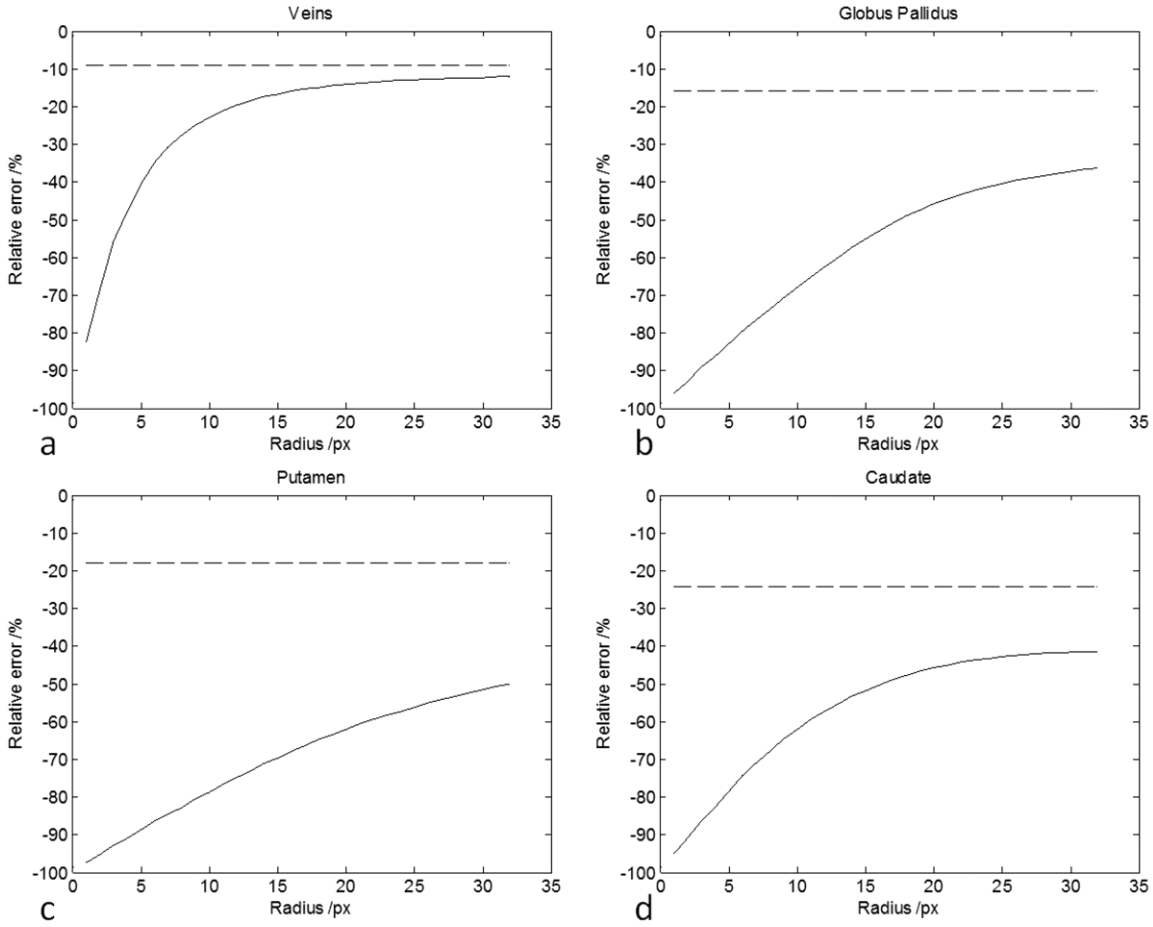

Figure 3.5 Relative errors in the estimated susceptibilities of different structures using phase images processed by VHP. a) Veins. b) Globus pallidus. c) Putamen. d) Caudate. The dashed lines indicate the errors in estimated susceptibilities for different structures using the phase images with ideal background field removal.

For the processed phase images, the larger the radius of the spherical kernel, the smaller the error caused by spherical filtering. When spherical kernels with different radii were applied to different regions, the error in the estimated susceptibility of a certain structure can be different due to the different locations of the structures. The most affected structures are those which extend significantly spatially, e.g., putamen. Compared with

traditional high-pass filtering with a single filter size, this variable high-pass filter helps to preserve the low spatial frequency signal of the big structures while providing accurate phase information of the veins.

3.4 Sophisticated Harmonic Artifact Reduction for Phase data (SHARP)

3.4.1 Theory

The same set of equations used in VHP, Eqs. 3.7 to 3.9, are used in SHARP to remove the background field, since SHARP is also based on the spherical mean value property of the background field. Nonetheless, as can be seen from Eq. 3.9, the obtained local field variation is essentially high-pass filtered. Thus, the last step in SHARP is to solve Eq. 3.9 for the local field variation $\Delta B_l(\vec{r})$ as an inverse problem (6). This deconvolution process is done typically using a truncated version of the filter in Fourier domain, similar to the truncated k-space division method for QSM described in Chapters 2 and 5. Again, the pixels close to the edges will not have the correct convolution result, and will have to be removed using an eroded brain mask *M*. The last step in SHARP can be written as:

$$\Delta B_l(\vec{r}) \approx FT^{-1}\{FT[M \cdot \Delta B(\vec{r}) * (\delta - s)] \cdot s'^{-1}(\vec{k})\} \qquad [3.11],$$

where the regularized inverse filter $s'^{-1}(\vec{k})$ is defined as:

$$s'^{-1}(\vec{k}) = \begin{cases} \{FT[(\delta - s)]\}^{-1}, & if \ \ |FT[(\delta - s)]| > th \\ 0, & otherwise \end{cases} \qquad [3.12].$$

Another way is to solve this inverse problem as an optimization problem with *a priori* information incorporated (20).

3.4.2 The influences of processing parameters on the accuracy of SHARP

The accuracy of SHARP is dependent on both the radius of the spherical kernel and the deconvolution process. In this study, the deconvolution was done using the regularized inverse filter shown in Eq. 3.11. In order to evaluate the effects of both the radius of the spherical kernel and the regularization threshold *th*, and to determine the optimal processing parameters in SHARP, SHARP with different spherical kernel sizes and different threshold values were tested using the simulated phase images of the 3D brain model. The same 3D brain model which was used to evaluate the accuracy of VHP was also used in this section. Particularly, the radii of the spherical kernel ranged from 1 pixel to 16 pixels with step size 1 pixel, and the values of *th* ranged from 0.005 to 0.1 with step size 0.005. Again, RMSEs in the processed phase images and the susceptibility maps were used to evaluate the accuracy of SHARP. The relative errors in the measured susceptibilities for different structures were used to assess the effects of SHARP on susceptibility quantification of different structures.

Fig. 3.6.a shows the overall RMSE in the phase images processed using SHARP. The overall RMSE in the susceptibility map, generated using the SHARP processed phase images is shown in **Fig. 3.6.b.** Generally speaking, spherical kernels with larger radii lead to smaller errors. For individual structures, the optimal spherical kernel radius and regularization threshold may vary a lot, as shown in **Figs 3.7** and **3.8**.

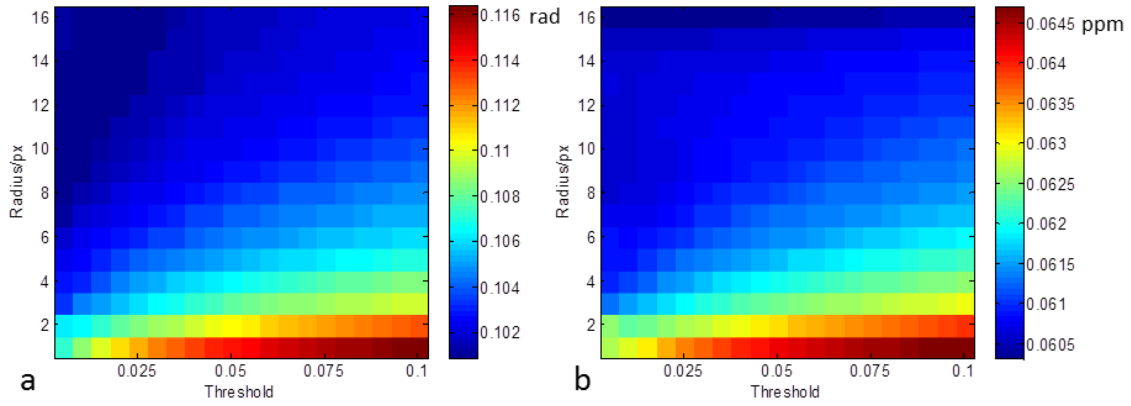

Figure 3.6 a) Overall RMSEs for different radii of the spherical kernel and different values of ***th*** in SHARP. **b)** Overall RMSE in susceptibility quantification for different kernel sizes and different thresholds in SHARP.

The relative errors in the measured susceptibilities for different structures are illustrated in **Fig. 3.7**. Large relative error in the estimated susceptibility was observed for thalamus, where the error was higher than 50%. This could be caused by the low susceptibility value of the thalamus and by the streaking artefacts from the veins nearby. For the other structures, in order to maintain a low level of error, the proper choice of the kernel size depends on the sizes of the structures. For veins, spherical kernel with radius larger than 3 pixels leads to reasonable accuracy. But for larger structures, such as the putamen, the radius of the spherical kernel has to be at least 6 pixels.

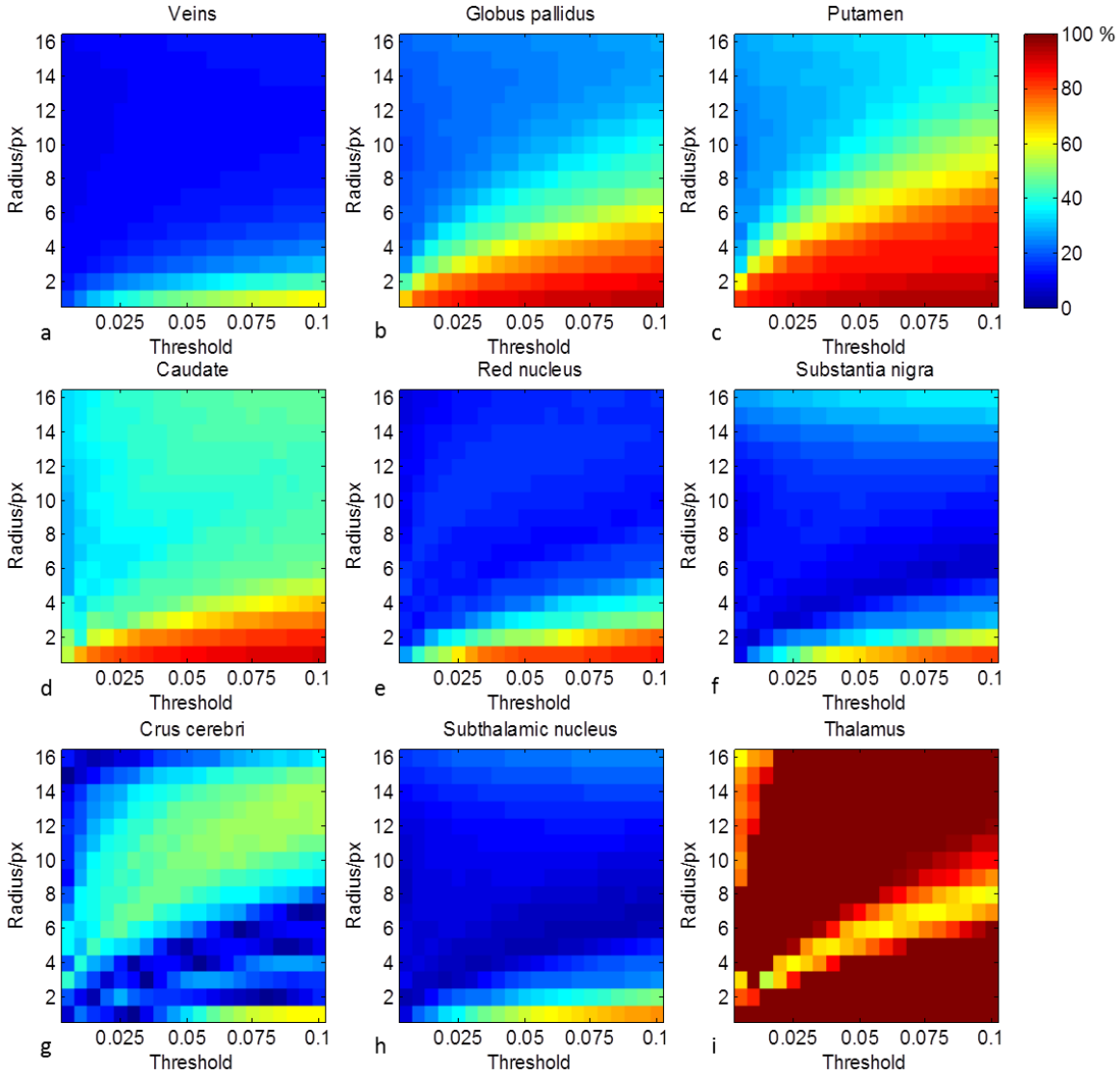

Figure 3.7 Relative errors in measured susceptibilities using different parameters in SHARP for different structures.

For different structures, the minimal relative errors in the estimated susceptibility values as functions of the radius of the spherical kernel are plotted in **Fig. 3.8**. The minimal errors in susceptibility estimates decreases as the radius of the spherical kernel increases for all the structures, except for substantia nigra, crus cerebri and subthalamic nucleus.

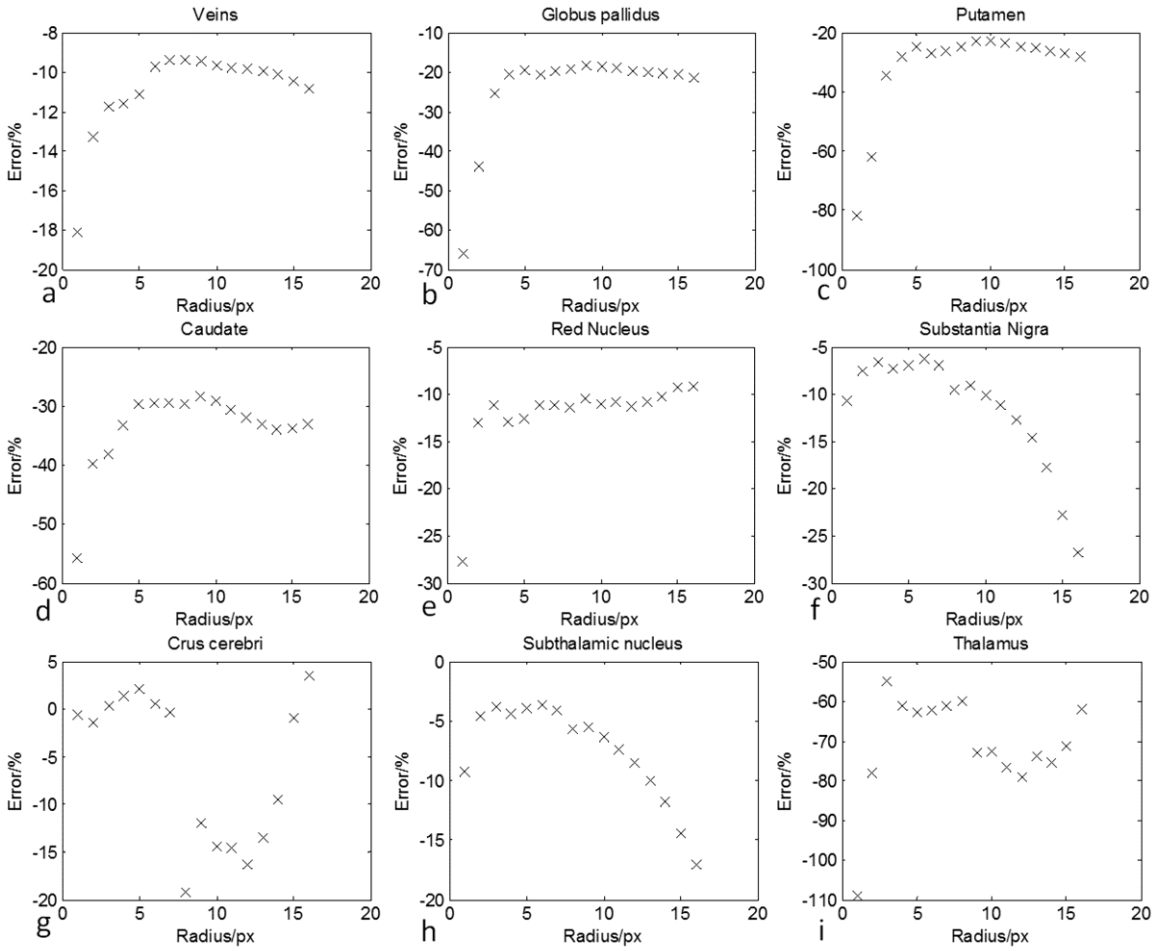

Figure 3.8 The minimal RMSEs for different structures at different radii of the spherical kernel in SHARP.

Considering the relatively higher signal loss at larger kernel sizes, a reasonable choice for the size of the spherical kernel in SHARP should be around 6-10 pixels (16). For the simulated data used in this study, the regularization threshold should be kept as small as possible (th<=0.05). However, for *in vivo* data, a higher threshold may be desired, in order to suppress non-harmonic phase components (6), e.g., the phase offset term $\phi_0(\vec{r})$. Examples of the phase images processed with SHARP are available in the next section.

3.5 Comparison of different background field removal algorithms

In addition to homodyne high-pass filtering, VHP, and SHARP, another popular background field removal algorithm is Projection onto the Dipole Field (PDF). In PDF, the background field inside the brain is assumed to be caused by the point-dipole sources outside the brain (5). And the background susceptibility distribution is estimated as:

$$argmin_{\Delta\chi_b(r)}\left||\Delta B(r)/B_0 - \Delta\chi_b(r) * g(r)|\right|_2^2 \quad [3.13].$$

Once $\Delta\chi_b(r)$ is known, the background field can be calculated using the forward calculation and subsequently removed. However, the estimated $\Delta\chi_b(r)$ does not reflect the actual background susceptibility distribution, but is only used for the purpose of removing the background field (5). Moreover, an additional high pass filter using spherical kernel is usually applied to the PDF processed phase images to further reduce the low spatial frequency phase artefacts.

3.5.1 Simulations and *in vivo* data studies

In this section, different background field removal algorithms are compared using the 3D brain model and *in vivo* data. The data of the 3D brain model were created in the same way as in the previous section. For the *in vivo* data, 5 datasets were collected on the same healthy volunteer using the parameters shown in **Table 3.1.** Except for the last dataset, which was collected using a double-echo sequence (only the longer TE's data were used here), all the other datasets were collected using single echo gradient echo sequences. The original phase images of the *in vivo* data were first unwrapped using a path-following 3D

phase unwrapping algorithm (21). Binary brain masks were generated using Brain Extraction Tool (BET) in FSL (22). Other processing parameters used in different algorithms are listed in **Table 3.2**. For homodyne high-pass filtering, only the 64x64 filter was applied to the *in vivo* data, in order to avoid any remnant aliasing near the air-tissue interfaces. For both the brain model and *in vivo* data, susceptibility maps were generated using truncated k-space division with threshold 0.1, using the phase images processed with different algorithms. This algorithm was chosen, primarily because of its simplicity and well understood systematic error. The susceptibilities were measured for 9 structures in the brain model, as shown in **Table 3.3**. For the *in vivo* data, the mean value of the susceptibilities were measured for a total of 7 structures, including veins, globus pallidus (GP), putamen (PUT), caudate nucleus (CN), substantia nigra (SN), red nucleus (RN) and thalamus (THA) using manually drawn ROIs. One-way ANOVA was used to test the differences seen in the measured susceptibilities obtained using different phase processing algorithms, for each structure. $p<0.05$ was considered as significant.

3.5.2 Simulated data results

For simulated data, VHP, SHARP and PDF led to similar level of errors in the estimated susceptibilities for different structures, as shown in **Table 3.3**. For basal ganglia structures, the truncated k-space division algorithm for susceptibility mapping will cause an underestimation around 10-20%. The VHP, SHARP and PDF processed phase images lead to an additional 20% error for basal ganglia structures. For other structures such as veins, the underestimation was smaller. The most severe error was seen in the results for

thalamus, for which the underestimations in the measured susceptibilities were large for all three phase processing methods. Even using the phase images with ideal background field removal in susceptibility quantification, the error was still large. This suggests that this error is largely caused by the truncated k-space division algorithm itself.

Table 3.1 Imaging parameters for the *in vivo* data.

Datasets	1	2	3	4	5
TE (in ms)	14.3	17.3	12.8	19.2	17.6
TR (in ms)	26	26	34	34	30
BW (in Hz/px)	121	121	130	130	425
Voxel Size (in mm^3)	0.5×0.5×0.5	0.5×0.5×0.5	0.6×0.6×1.2	0.6×0.6×1.2	0.6×0.6×1.2
Matrix Size	512×368×256	512×368×196	512×336×112	512×336×112	512×368×144
Flip Angle (in degrees)	15	15	15	15	15

Table 3.2 Data processing parameters in different algorithms.

	Simulated data	*In vivo* data
Homodyne high-pass filter	k-space window sizes 32x32 and 64x64	k-space window sizes 64x64
VHP	Spherical kernel radii: 32 px (largest), 1 px (smallest)	Spherical kernel radii: 32 px (largest), 1 px (smallest)
SHARP	Spherical kernel radius: 8 px, Regularization thresholds: 0.02 and 0.05	Spherical kernel radius: 8 px, Regularization threshold: 0.05
PDF	Convergence tolerance: 10^{-3}	Convergence tolerance: 10^{-2} Spherical kernel radius: 32px

Table 3.3 The estimated susceptibilities (mean ± std. in ppm) for different structures in the brain model using different phase processing methods. "Original Phase" represents using the simulated phase images without any background field.

	$\Delta\chi_{true}$	Original Phase	HP32	HP64	VHP	SHARP th=0.02	SHARP th=0.05	PDF
Veins	0.45	0.41 ±0.07	0.36 ±0.09	0.33 ±0.09	0.40 ±0.07	0.40 ±0.07	0.40 ±0.07	0.40 ±0.07
Thalamus	0.01	0±0.06	-0.02 ±0.06	-0.01 ±0.06	0 ±0.06	0 ±0.06	0 ±0.06	0 ±0.06
Red Nucleus	0.13	0.12 ±0.06	0.07 ±0.06	0.07 ±0.06	0.11 ±0.06	0.11 ±0.06	0.11 ±0.06	0.11 ±0.06
Substantia Nigra	0.16	0.15 ±0.06	0.09 ±0.07	0.09 ±0.07	0.13 ±0.06	0.14 ±0.06	0.14 ±0.06	0.14 ±0.06
Subthalamic Nucleus	0.20	0.19 ±0.06	0.15 ±0.07	0.14 ±0.06	0.18 ±0.06	0.18 ±0.06	0.18 ±0.06	0.19 ±0.06
Crus Cerebri	-0.03	-0.03 ±0.06	-0.04 ±0.07	-0.03 ±0.06	-0.04 ±0.06	-0.04 ±0.06	-0.04 ±0.06	-0.03 ±0.06
Caudate	0.06	0.05 ±0.06	0.03 ±0.07	0.02 ±0.06	0.04 ±0.06	0.04 ±0.06	0.04 ±0.06	0.04 ±0.06
Putamen	0.09	0.07 ±0.06	0.02 ±0.08	0.01 ±0.07	0.05 ±0.06	0.06 ±0.06	0.05 ±0.06	0.06 ±0.06
Globus Pallidus	0.18	0.15 ±0.06	0.06 ±0.07	0.05 ±0.07	0.11 ±0.06	0.14 ±0.06	0.12 ±0.06	0.13 ±0.06

On the other hand, the homodyne high-pass filters caused much larger error, especially for bigger structures such as those basal ganglia structures. Using homodyne high-pass filter with window size 32×32 caused smaller error than using a window size 64×64, as expected.

Moreover, the susceptibilities obtained using the simulated phase images without background field are plotted against the susceptibilities obtained using the phase images processed with different algorithms, as shown in **Fig. 3.9**. This figure reflects the effects of different phase processing methods on susceptibility mapping. Particularly, if no additional errors are caused by the phase processing methods, the susceptibilities estimated using the processed phase images should be almost the same as those estimated using the original phase images. This can be indicated by the slopes and the correlation coefficients of the linear regressions shown in **Fig. 3.9**. The smaller the slope, the more underestimation in susceptibilities the filter causes. The smaller the correlation coefficient, the more uncertainty the filter induces. The homodyne high-pass filtering leads to more underestimation in the estimated susceptibilities than the other phase processing methods, and 32x32 homodyne high-pass filter causes less underestimation than 64x64 high-pass filter does. Using the phase images processed by VHP, SHARP and PDF, the estimated susceptibilities are almost the same as those obtained using the original unfiltered phase images.

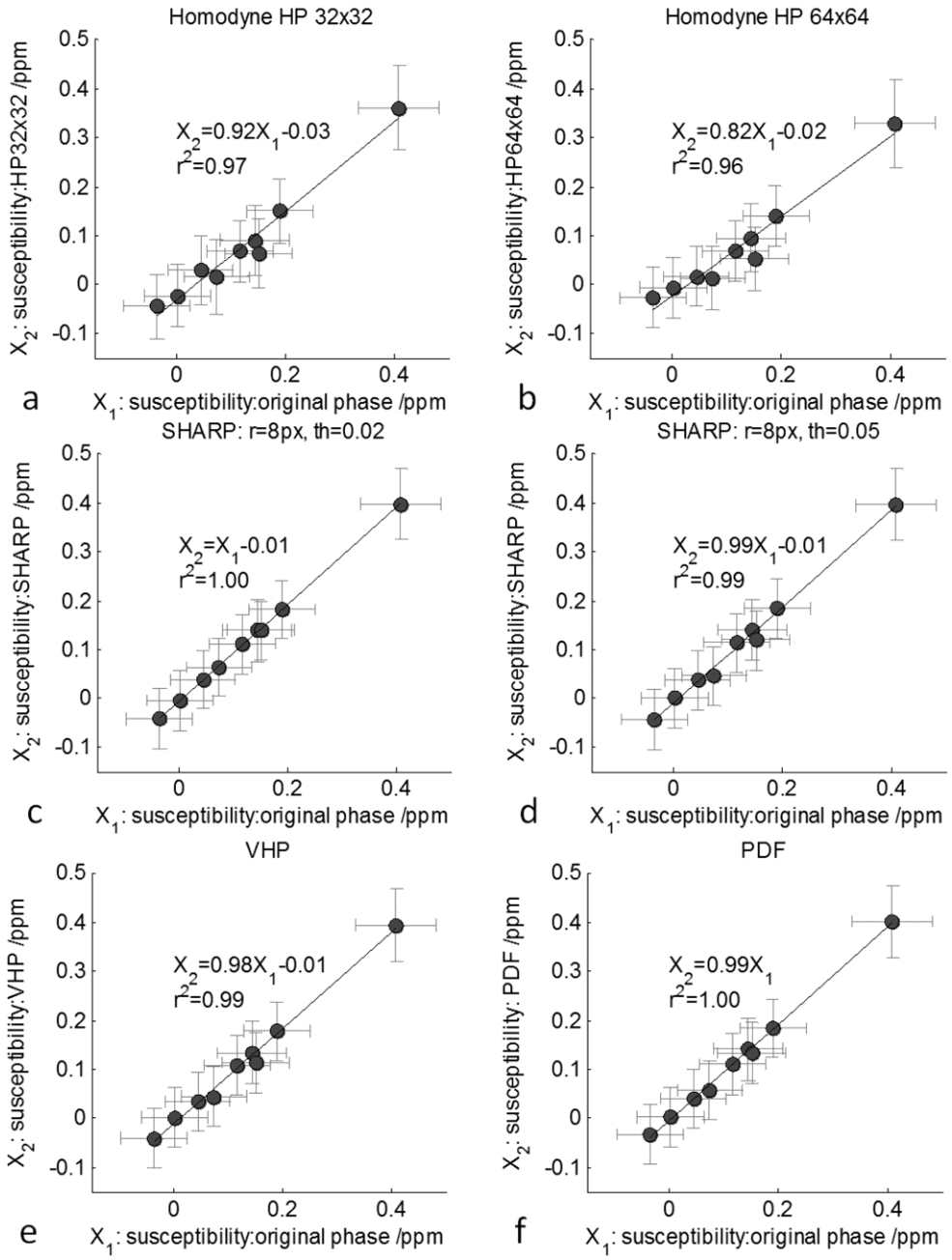

Figure 3.9 Susceptibility estimated using the original phase vs. the susceptibility estimated using different phase processing methods: **a)** Homodyne HP32×32, **b)** Homodyne HP64×64, **c)** SHARP (radius=8px, th=0.02), **d)** SHARP (radius=8px, th=0.05), **e)** Variable HP, and **f)** PDF.

3.5.3 *In vivo* data results

The phase images in Dataset 1 processed using different algorithms are shown in **Fig. 3.10**. Edge artefacts were observed in the homodyne high-pass filter processed phase images. The edge artefact was propagated into the susceptibility maps, as can be seen from **Fig. 3.11.a** and **3.11.e**. The VHP processed phase images (**Fig. 3.11.b** and **3.11.f**) show good agreement with the SHARP processed phase images. However, the regions close to the edge of the brains have signal loss due to the strong high-pass filter that is applied to these regions. The SHARP processed phase images have severe error near the superior sagittal sinus (SSS), as shown in **Fig. 3.11.c**. This is due to the partial removal of the SSS by the brain mask. Even though a mild high-pass filter was applied, a slowly varying remnant background profile was still observed in the PDF processed phase images, as can be seen from **Fig. 3.10.d** and **3.10.h**. A relatively large error was found for the structures close to the edge of the brain, using PDF processed phase images.

Using different background field removal algorithms, the measured susceptibilities for different structures in the *in vivo* data are compared in **Fig. 3.12**. Compared with other algorithms, homodyne high-pass filter caused more under-estimation in the measured susceptibilities for all the structures ($p<<0.05$), except for the caudate nucleus ($p=0.8717$). For homodyne high-pass filtering, the large variation in the measured susceptibility for the same structure across different datasets is partly caused by the remnant phase aliasing artefacts in the high-pass filtered phase images. VHP, SHARP, and PDF led to almost the same susceptibility estimates for all the structures, except for the thalamus ($p=0.0182$).

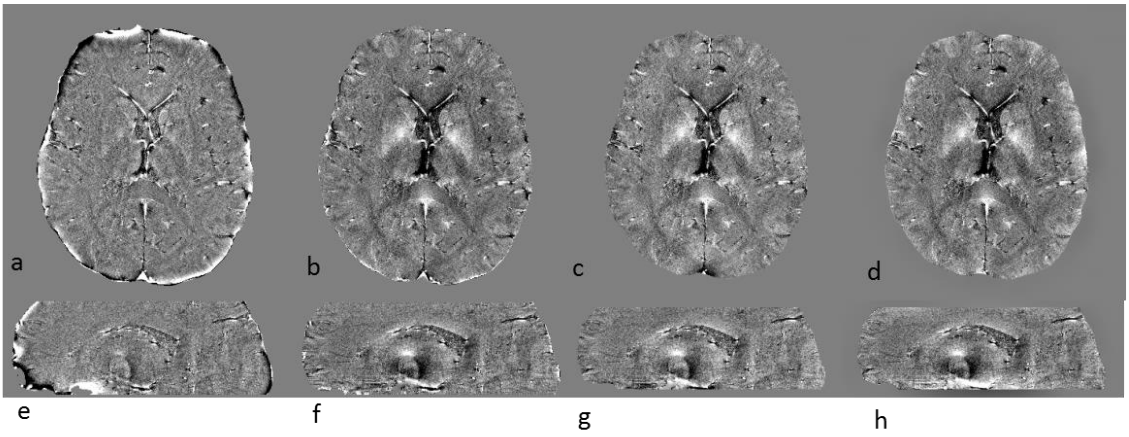

Figure 3.10 Phase images processed with different algorithms in Dataset 1. **a** and **e**. 64x64 Homodyne high-pass filter. **b** and **f**: VHP. **c** and **g**: SHARP. **d** and **h**: PDF.

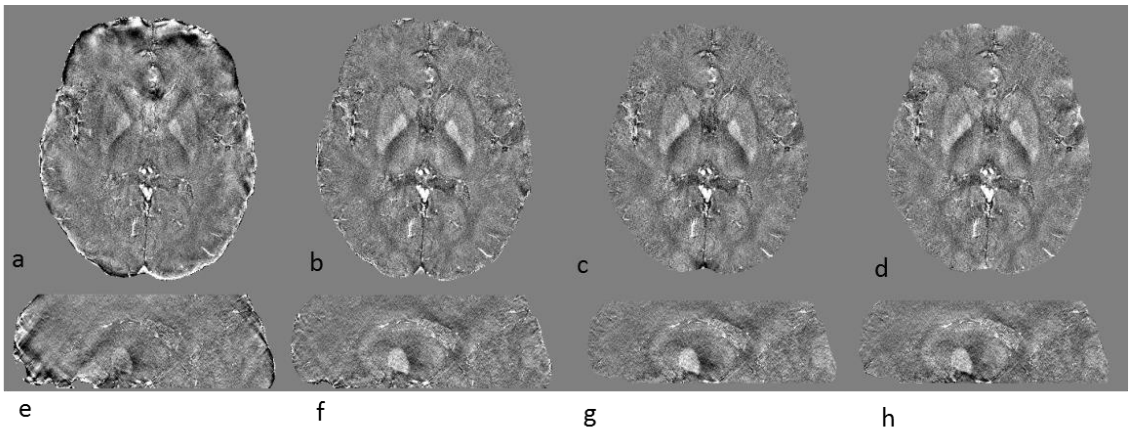

Figure 3.11 Susceptibility maps generated with different algorithms in Dataset 1. **a** and **e**. 64×64 Homodyne high-pass filter. **b** and **f**: VHP. **c** and **g**: SHARP. **d** and **h**: PDF.

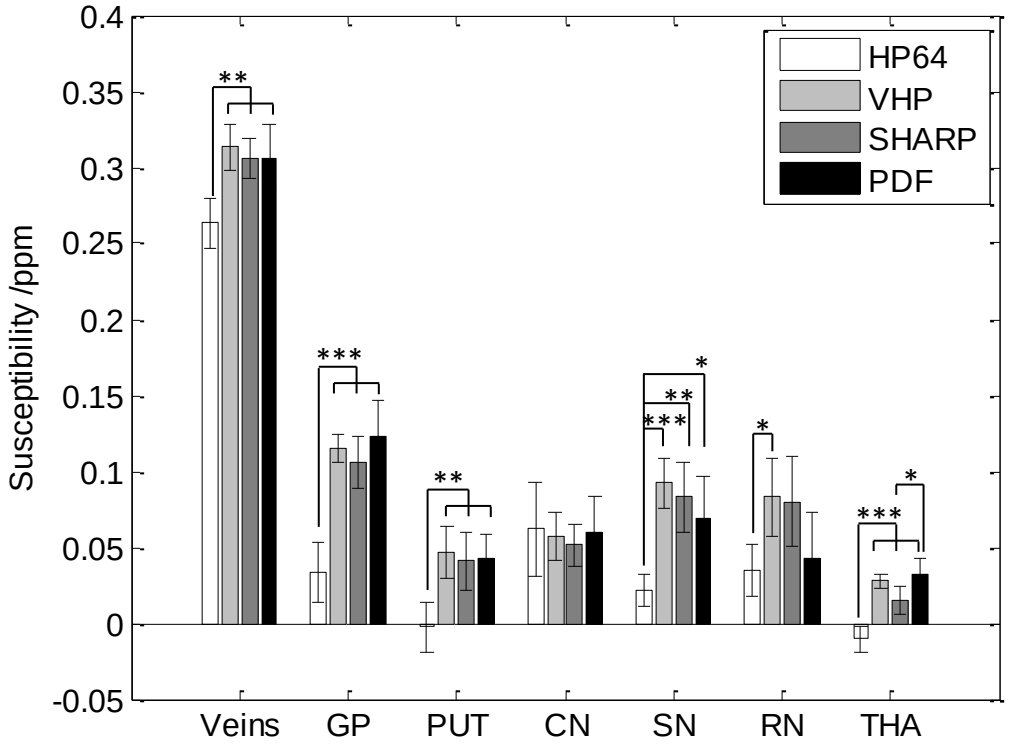

Figure 3.12 The means and standard deviations of the measured susceptibility values for different structures in different *in vivo* datasets. The error bars represent the standard deviations of the measured susceptibilities in different datasets. GP: globus pallidus, PUT: putamen, CN: caudate nucleus, SN: substantia nigra, RN: red nucleus, and THA: thalamus. The asterisks indicate Tukey's HSD significance: * $p<0.05$, ** $p<0.01$, *** $p<0.001$.

3.5.4 Discussion and conclusions

Clearly, the variable high-pass filtering (VHP) leads to less underestimation in the susceptibility estimation, compared with the traditional homodyne high-pass filtering. In

VHP, the spherical kernel is used to generate a low-pass filtered phase image (the averaged phase image) which is close to the background phase. As can be seen from the results, variable high-pass filtering leads to similar results as SHARP. The only difference between VHP and SHARP is that, no additional deconvolution is required in VHP. This helps to avoid any amplification of noise due to the deconvolution. In addition, there is no need to select any regularization parameter for deconvolution, as it is done in SHARP.

It can be concluded that the error in SHARP processed phase images reduces as the size of the spherical kernel increases. This is mainly due to the deconvolution process, as larger spherical kernel leads to less amplification of any remnant background field. However, as the size of the spherical kernel increases, more of the brain region will be affected by edge artefacts. The erosion of the brain mask leads to signal loss and is a particular limitation of SHARP. One possible solution is to extend the field continuously to the regions outside of the brain (16, 23).

Both SHARP and VHP processed phase images lead to small errors in the estimated susceptibilities for most structures, except for the thalamus. This might be due to the low susceptibility and the large size of the thalamus. For veins and basal ganglia structures, the error is relatively more stable.

PDF processed phase images are also affected by edge artefacts. This large error close to the edge was explained to be caused by the violation of the assumption of PDF, that is, the field induced by the dipole sources located within the brain is orthogonal to the field induced by the dipole sources outside the brain. Further, a remnant slowly varying

background phase component was observed for the PDF processed phase images, for the *in vivo* data. This might be caused by the phase offset, ϕ_0, which could be removed when data were collected with a multi-echo gradient echo sequence.

Generally speaking, if the original phase images are unwrapped properly, SHARP is found to be the most efficient background field removal algorithm among all the available algorithms. However, if a region with noisy phase values were included in the region of interest, the phase unwrapping may fail (2) and accuracy of SHARP processed phase images could be deteriorated by the deconvolution step (24). For instance, when there is cusp artefact/open-ended fringe lines in the phase images, most phase unwrapping algorithm will fail. In such cases, it would be better to simply use the variable high-pass filter which does not perform any deconvolution, in order to avoid any amplification of the artefacts coming from the noisy region included in the region of interest.

References

1. Haacke EM, Brown RW, Thompson MR, Venkatesan R. Magnetic Resonance Imaging: Physical Principles and Sequence Design. 1st ed. Wiley-Liss; 1999.
2. Haacke EM, Reichenbach JR, editors. Susceptibility Weighted Imaging in MRI: Basic Concepts and Clinical Applications. 1st ed. Wiley-Blackwell; 2011.
3. Li L. Magnetic susceptibility quantification for arbitrarily shaped objects in inhomogeneous fields. Magn. Reson. Med. 2001;46:907–16.
4. Neelavalli J, Cheng YCN, Jiang J, Haacke EM. Removing background phase variations in susceptibility-weighted imaging using a fast, forward-field calculation. J. Magn. Reson. Imaging 2009;29:937–48.
5. Liu T, Khalidov I, de Rochefort L, Spincemaille P, Liu J, Tsiouris AJ, et al. A novel background field removal method for MRI using projection onto dipole fields (PDF). NMR Biomed. 2011;24:1129–36.
6. Schweser F, Deistung A, Lehr BW, Reichenbach JR. Quantitative imaging of intrinsic magnetic tissue properties using MRI signal phase: An approach to in vivo brain iron metabolism? NeuroImage 2011;54:2789–807.
7. Li W, Wu B, Liu C. Quantitative susceptibility mapping of human brain reflects spatial variation in tissue composition. NeuroImage 2011;55:1645–56.
8. Reichenbach JR, Venkatesan R, Schillinger DJ, Kido DK, Haacke EM. Small vessels in the human brain: MR venography with deoxyhemoglobin as an intrinsic contrast agent. Radiology 1997;204:272–7.
9. Reichenbach JR, Essig M, Haacke EM, Lee BC, Przetak C, Kaiser WA, et al. High-resolution venography of the brain using magnetic resonance imaging. MAGMA 1998;6:62–9.
10. Haacke EM, Xu Y, Cheng YN, Reichenbach JR. Susceptibility weighted imaging (SWI). Magn. Reson. Med. 2004;52:612–8.
11. Buch S, Ye Y, Cheng Y, Neelavalli J, Haacke EM. Susceptibility mapping of air, bone and calcium in the head using short echo times. Magn. Reson. Med. 2013;
12. Haacke EM, Mittal S, Wu Z, Neelavalli J, Cheng Y-CN. Susceptibility-Weighted Imaging: Technical Aspects and Clinical Applications, Part 1. Am. J. Neuroradiol. 2009;30:19–30.
13. Tang J, Liu S, Neelavalli J, Cheng YCN, Buch S, Haacke EM. Improving susceptibility mapping using a threshold-based K-space/image domain iterative reconstruction approach. Magn. Reson. Med. 2013;69:1396–407.
14. Neelavalli J, Liu S, Cheng Y, Haacke EM, Kou Z. Effect of Orientation of 2D Phase High-Pass Filter on Susceptibility Mapping of Veins and Microbleeds. Proc. 19th Annu. Meet. ISMRM Montr. Quebec Canada. 2011:4517.
15. Haacke EM, Tang J, Neelavalli J, Cheng YC. Susceptibility mapping as a means to visualize veins and quantify oxygen saturation. J. Magn. Reson. Imaging 2010;32:663–76.
16. Li W, Avram AV, Wu B, Xiao X, Liu C. Integrated Laplacian-based phase unwrapping and background phase removal for quantitative susceptibility mapping. NMR Biomed. 2013; DOI: 10.1002/nbm.3056

17. Cheng Y-CN, Neelavalli J, Haacke EM. Limitations of calculating field distributions and magnetic susceptibilities in MRI using a Fourier based method. Phys. Med. Biol. 2009;54:1169–89.
18. Marques J p., Bowtell R. Application of a Fourier-based method for rapid calculation of field inhomogeneity due to spatial variation of magnetic susceptibility. Concepts Magn. Reson. Part B Magn. Reson. Eng. 2005;25B:65–78.
19. Gudbjartsson H, Patz S. The Rician distribution of noisy MRI data. Magn. Reson. Med. 1995;34:910–4.
20. Sun H, Wilman AH. Background field removal using spherical mean value filtering and Tikhonov regularization. Magn. Reson. Med. 2013; DOI: 10.1002/mrm.24765
21. Abdul-Rahman HS, Gdeisat MA, Burton DR, Lalor MJ, Lilley F, Moore CJ. Fast and robust three-dimensional best path phase unwrapping algorithm. Appl. Opt. 2007;46:6623–35.
22. Smith SM. Fast robust automated brain extraction. Hum. Brain Mapp. 2002;17:143–55.
23. Topfer, R., Schweser, F., Deistung, A., Reichenbach, J. R. and Wilman, A. H. (2014), SHARP edges: Recovering cortical phase contrast through harmonic extension. Magn Reson Med. doi: 10.1002/mrm.25148
24. Schweser F, Deistung A, Sommer K, Reichenbach JR. Toward online reconstruction of quantitative susceptibility maps: superfast dipole inversion. Magn. Reson. Med. 2013;69:1582–94.

Chapter 4 Fast and Robust Background Field Removal using Double-echo Data

4.1 Introduction

Quantitative susceptibility mapping (QSM) has great potential in elucidating tissue properties and providing functional information *in vivo*. It has already found various applications, such as the quantification of cerebral iron content (1,2), venous oxygen saturation (3,4), and monitoring the changes of cerebral lesions and microbleeds (5,6). To extract the susceptibility distribution, normally the phase images from a gradient echo sequence are required. However, the phase images are contaminated by background field inhomogeneities. The background field induced phase component is referred to as the background phase in this study. Various algorithms have been proposed to remove the background phase and to extract the local phase which contains the field variation induced by local susceptibility changes (7-11). Most of these approaches require phase unwrapping, which can be time-consuming or sensitive to noise (12). To further

complicate the problem, any improper combination of the phase data collected with multi-channel coil will lead to signal cancelation and open-ended fringe lines/cusp artefacts in the phase images (13-15), which may severely affect the accuracy of phase unwrapping and, hence, background phase removal. Any error in background phase removal will propagate into the susceptibility maps (16,17). Consequently, reliable background phase removal is a critical step, as it directly determines the quality and accuracy of QSM.

Currently, there are mainly four types of background field/phase removal algorithms: homodyne high-pass filtering (7), geometry dependent artefact correction (GDAC) (8), projection onto the dipole field (PDF) (9) and sophisticated harmonic artefact reduction for phase data (SHARP) (10). The homodyne high-pass filtering has been successfully applied in susceptibility weighted imaging (SWI), due to its robustness and effectiveness. However, it also causes loss of low spatial frequency phase information to structures with relatively big size. The high-pass filter size could be reduced in the geometry dependent artefact correction (GDAC) method, but the accuracy of GDAC is largely dependent on the *a priori* information of the geometries of the air-tissue interfaces. Both PDF and SHARP utilize the fact that the background phase originated from the susceptibility sources outside the brain satisfies Laplace's equation (9,10). Particularly, SHARP, or spherical mean value filtering based techniques have been shown be computationally efficient in removing the background phase (10). Except for homodyne high-pass filtering, all of these algorithms require phase unwrapping.

Phase unwrapping could be done through either spatial or temporal domain algorithms (18,19). For temporal phase unwrapping, multiple echoes are required (19,20). The

choices of the echo times may be restricted by the requirement of applying 3D flow compensation gradient, when studying susceptibilities of veins (7,21). For spatial domain methods, path-following and quality-guided algorithms are typically used (18,22-24). In these algorithms, the spatial smoothness of the phase images is assumed. Since the Laplacian of phase can be calculated directly from the original phase images, another common strategy is to use Laplacian based phase unwrapping or to use the Laplacian of phase directly in background field removal (11,17). However, when the Laplacian is directly used, the accuracy of the extracted local phase information will be reduced (25); when the Laplacian based phase unwrapping algorithm is used, there are errors in the regions near the edges of the brain or major veins (11,17,25).

In this study, we propose a background field removal algorithm in which the local phase unwrapping and background phase removal are performed simultaneously, and the global phase unwrapping is bypassed. For the best performance of this algorithm, multi-echo data, in this case double-echo data are used. We also show that the artefacts induced by T_2^* effects at a long echo time, as well as the phase singularities can be reduced when handled properly.

4.2 Theory

For a left-handed system, the phase information in a gradient echo sequence with echo time TE can be written as:

$$\phi_w(\vec{r}) = \gamma \Delta B(\vec{r}) TE + \phi_0(\vec{r}) + 2n(\vec{r})\pi \qquad [4.1],$$

where $\phi_0(\vec{r})$ is the phase offset at TE=0. This phase offset is related to the coil sensitivity and conductivity of the tissues (26,27). Usually, the original phase images are aliased and should be unwrapped. This is done by determining $n(\vec{r})$ and subtracting $2n(\vec{r})\pi$ from the original phase images:

$$\phi(\vec{r}) = \phi_w(\vec{r}) - 2n(\vec{r})\pi \quad [4.2].$$

The unwrapped phase information can be viewed as two components, the background phase $\phi_b(\vec{r})$ and the local phase $\phi_l(\vec{r})$:

$$\phi(\vec{r}) = \phi_b(\vec{r}) + \phi_l(\vec{r}) \quad [4.3].$$

The background phase and the local phase are directly proportional to the background field and the local field, respectively. Using the spherical mean value property of the background field, it was shown that (28):

$$\phi_b(\vec{r}) - \phi_b(\vec{r}) * s = 0 \quad [4.4],$$

where "s" is a normalized spherical kernel and * represents the convolution operation. The background phase can be removed using Eqs. 4.3 and 4.4:

$$\phi(\vec{r}) - \phi(\vec{r}) * s = \phi_l(\vec{r}) - \phi_l(\vec{r}) * s \quad [4.5].$$

Eq. 4.5 is the critical step to remove the unwanted background phase variations. This is referred to as spherical mean value filtering (SMV) (28). To calculate the convolution in Eq. 4.5, there should not be any discontinuities in the original phase images, i.e., phase unwrapping is required. Denoting the result of Eq. 4.5 as $\phi_{SMV}(\vec{r})$, it is essentially the difference between the phase value of a given pixel and the mean phase value in the local

spherical VOI and, hence, is not dependent on the baseline. Consequently, it is only necessary to unwrap the local spherical VOI. When the maximal phase difference between any pixel and the central pixel in the spherical VOI does not exceed π, the local phase unwrapping can be achieved through baseline shifting:

$$\phi_{w,shifted}(\vec{r}) = arg(\{exp[i(\phi_w(\vec{r}) + \phi_{shift})]\}) - \phi_{shift} \quad [4.6].$$

For each ϕ_{shift}, $\phi_{SMV}(\vec{r})$ can be calculated using Eq. 4.5, but only for those pixels which are sufficiently far away (i.e., with a distance larger than the radius of the spherical kernel) from any phase wraps. The remnant unresolved pixels are those where the phase gradients are too big, e.g., the regions close to the air-tissue interfaces, or those which are close to phase singularities/noisy phase pixels. In the former case, the phase images cannot be unwrapped locally using baseline shifting and $\phi_{SMV}(\vec{r})$ will be set to 0. In the latter case, for a particular pixel at $\vec{r}_0$, $\phi_{SMV}(\vec{r}_0)$ was calculated through local complex division:

$$\phi_{SMV}(\vec{r}_0) = \sum_{i=1}^{N} arg\{exp[i * (\phi_w(\vec{r}_0) - \phi_w(\vec{r}_i))]\}/N \quad [4.7],$$

where *N* is the total number of pixels of the spherical kernel *s* centered at $\vec{r}_0$.

Combining all the steps, we obtain $\phi_{SMV}(\vec{r})$ and then the local phase $\phi_l(\vec{r})$ is extracted via the deconvolution process:

$$\phi_l(\vec{r}) = \phi_{SMV}(\vec{r}) * (\delta - s)^{-1} \quad [4.8].$$

The regularized deconvolution can be performed in the Fourier domain through thresholded division or other regularized inversion algorithms (10,29).

In the above calculations, it is assumed that TE is sufficiently short or the gradient of total field variation is sufficiently low. For the phase data at a long TE, TE_2, $\phi_{\Delta TE}(\vec{r})$ with a short effective echo time can be constructed through complex division using the phase images at the shorter TE, TE_1:

$$\phi_{\Delta TE}(\vec{r}) = arg(exp\{i[\phi_{TE2}(\vec{r}) - \alpha\phi_{TE1}(\vec{r})]\}) \quad [4.9],$$

where α is an integer. The choices of α is dependent on the TEs and the SNRs of the phase data. Now $\phi_{\Delta TE}(\vec{r})$ can be processed in the same way as described above to obtain $\phi_{SMV,\Delta TE}(\vec{r})$, then $\phi_{SMV,TE2}(\vec{r})$ can be calculated as:

$$\phi_{SMV,TE2}(\vec{r}) = \phi_{SMV,\Delta TE}(\vec{r}) + \alpha\phi_{SMV,TE1}(\vec{r}) \quad [4.10].$$

Finally, the local phase $\phi_{l,TE2}(\vec{r})$ can be solved using $\phi_{SMV,TE2}(\vec{r})$ through Eq. 4.8. Alternatively, both $\phi_{l,TE1}(\vec{r})$ and $\phi_{l,\Delta TE}(\vec{r})$ can be generated first, then $\phi_{l,TE2}(\vec{r})$can be calculated in a way similar to Eq. 4.10. We refer to the whole process (Eqs. 4.5 to 4.10) as Local Spherical Mean Value filtering (LSMV) in this thesis.

4.3 Materials and Methods

4.3.1 3D brain model simulation

A 3D brain model was created to study the robustness of LSMV and to compare with other phase unwrapping algorithms for processing the phase images with single short echo at different noise levels. Various structures such as basal ganglia structures, grey/white matter, CSF as well as the air-sinuses were included in this brain model. To

simulate the background phase, the susceptibility in the air-sinuses was set to 9.4 ppm. The phase images were calculated using the forward calculation (8,30–32) at B_0=3T, TE=7.5ms. Magnitude images were also created with different T_1, T_2^*, proton density values assigned to different structures. White Gaussian noise was added to real and imaginary parts of the complex data and the SNR of the magnitude in the white matter region ranged from 5:1 to 20:1. The phase images with different noise levels were processed using the same steps as described in the *in vivo* data acquisition and processing section.

4.3.2 3D cylinder simulation

In order to evaluate the effects of T_2^* signal decay and partial volume on the proposed algorithm, the phase images of a 3D cylinder, as surrogate for the vein were created at two different TEs at B_0=3T. The susceptibility inside the cylinder was set to 0.45ppm and outside 0. The main field direction was set to be perpendicular to the long axis of the cylinder. The two TEs were chosen to be TE_1=7.5ms and TE_2=22.5ms. The magnitude was set to uniformly 1 initially, and then the regions inside the cylinder experienced T_2^* signal decay as a function of TE, with T_2^*=25ms. A background field, varying linearly along the main field direction, was added to the field map of the cylinder. The gradient of the background field was chosen such that the induced phase increment is 2π at TE_1 within the full FOV. The partial volume effects were simulated by first creating the magnitude and phase images of a 2D cylinder in an 8192×8192 matrix, then cropping the central 256×256 pixels of k-space. The radius of the cylinder in the final 256×256 matrix was 8

pixels. Finally, the phase images of the 3D cylinder were generated by stacking the phase images of the 2D cylinder along the long axis of the cylinder. Gaussian noise was added to real and imaginary channels of the complex data, and the SNR in the magnitude images varied from 5:1 to 20:1. For phase processing using LSMV, the phase images at TE_1 were complex divided twice into the phase images at TE_2 to create phase images with ΔTE of 7.5ms, i.e., $\alpha = 2$ in Eq. 4.9. The noisy pixels in the phase images at TE_2 were detected as where phase singularity occurred and where the SNR in magnitude images was less than 2:1. For the deconvolution step in Eq. 4.8, a regularization threshold 0.001 was used. Other processing steps are the same as described in the *in vivo* data processing section.

4.3.3 *In vivo* data acquisition and processing

The proposed method was tested on three *in vivo* datasets collected with 3D fully flow compensated double-echo gradient echo sequence (21), with GRAPPA acceleration factor of 2. Other imaging parameters are listed in **Table 4.1**. While higher spatial resolution was used in the first *in vivo* study, the lower through-plane resolutions used in the second and third *in vivo* studies are closer to the situations in most clinical applications. For the combination of multi-channel data, the linear gradients of the phase images from each channel were first corrected by shifting the echo center (the position of the pixel which has the maximum magnitude in k-space) to the actual center of k-space. The baseline of each channel was estimated from the center of k-space and removed subsequently. Finally, the phase data were combined through averaging of the complex data weighted by the magnitude images (13,14).

Table 4.1 Imaging parameters for the *in vivo* data. Datasets 1 and 2 were collected on the same volunteer.

	Dataset 1	Dataset 2	Dataset 3
Echo Time (ms)	TE_1=7.38, TE_2=17.6	TE_1=7.38, TE_2=22.14	TE_1=7.38, TE_2=22.14
TR	30	30	30
Flip Angle	15	15	15
Bandwidth (Hz/px)	425	425	425
Head-coil	32-channel	12-channel	32-channel
Voxel size (mm^3)	0.6×0.6×1.2	0.5×0.5×2	0.5×0.5×2
Matrix size	512×368×144	512×384×72	512×384×72

The local phase images at TE_1 and TE_2 were obtained using the following steps.

1. Generating the binary brain masks. This was done using the Brain Extraction Tool (BET) (33) in FSL, to the magnitude images at TE_2. In order to refine the brain masks, quality maps were generated (24) as a function of the local average number of phase singularities /poles which can be detected using the method described in (34). The brain masks were set to 0 where the values of the quality maps were below an empirically determined threshold.

2. Detecting the noisy pixels in the phase images

   There may be noisy pixels inside the brain with unreliable phase values, which could be induced by the phase singularities or T_2^* effects at a long TE. To detect these noisy

pixels, the phase singularities detected in Step 1 were used as candidates. Then the noisy pixels were determined as those where the SNR in magnitude image was less than 3:1. These noisy pixels were excluded from the calculation of the SMV filtered results.

3. Spherical mean value filtering (SMV) through global baseline shifting

   The SMV filtered results (ϕ_{SMV}) were first calculated using the original phase images, only for the pixels which were not affected by any phase wraps in the original phase images, using Eq. 4.5. The radius of the spherical kernel was set to 8 pixels. The phase wraps were detected when the absolute value of the phase difference between two neighboring pixels was greater than 0.9π. The pixels affected by the phase wraps were determined as those which were within 8 pixels to any phase wraps in 3D. Then the baseline of all the pixels in the original phase images were shifted by π using Eq. 4.6. Since most pixels close to the phase wraps in the original phase images have phase values close to π or $-\pi$, a baseline shift of π is most effective in shifting the baseline of those pixels to 0 and creating locally unwrapped regions. Then SMV filtered results were obtained using the baseline shifted phase images, using the same procedures as described above. After this step 3, there might be remnant pixels which are still affected by phase wraps. These pixels will be resolved in the next step.

4. Spherical mean value (SMV) filtering through local baseline shifting

   For a particular pixel, *P*, the phase value of all the pixels in the spherical VOI centered at *P* were complex divided by the phase value of *P*. After this local baseline shifting, if no phase wrap was detected in the local spherical VOI, the value of ϕ_{SMV} at *P* will be

calculated using Eq. 4.7. If phase wraps were detected, it suggests that either that local phase gradient is too big, or *P* is affected phase singularities. In the former case, ϕ_{SMV} cannot be calculated using this proposed method and was set to 0. In the latter case, ϕ_{SMV} was calculated again using Eq. 4.7.

5. Obtaining the local phase information through deconvolution

Finally, the local phase images (ϕ_l) were calculated through truncated Fourier domain division with regularization threshold 0.05, using Eq. 4.8. The whole process is illustrated in **Fig. 4.1**.

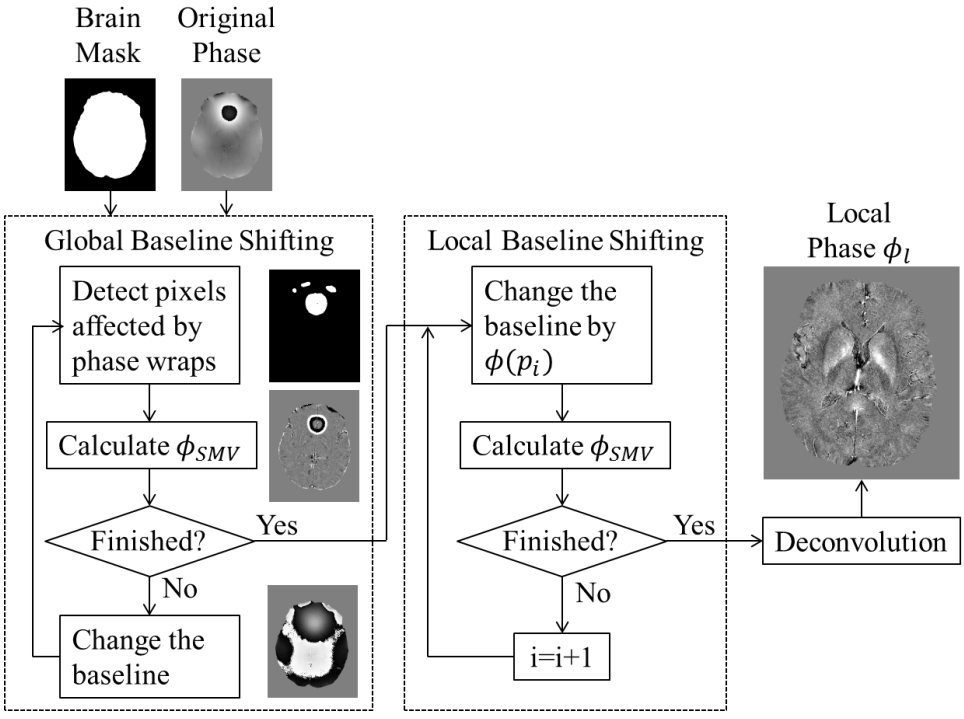

Figure 4.1 Processing steps in LSMV for single echo phase data with short TE.

To generate the local phase images at TE_2, the phase images at TE_1 were complex divided twice into those at TE_2 to create phase images at ΔTE. Then $\phi_{SMV,\Delta TE}$ was calculated using steps 2 to 5 as described above, and $\phi_{SMV,TE2}$ was calculated as $\phi_{SMV,\Delta TE} + 2\phi_{SMV,TE1}$. For any noisy pixels which were present only in the phase images at ΔTE but not in the phase images at TE_1, the values of $\phi_{SMV,\Delta TE}$ were obtained by projecting the values of $\phi_{SMV,TE1}$ from TE_1 to ΔTE as: $\phi_{SMV,TE1}/TE_1 \times \Delta TE$, assuming that the influence of the ϕ_0 term is sufficiently small.

4.3.4 Comparison with other phase unwrapping algorithms

The proposed algorithm was compared with two commonly used phase unwrapping algorithms. One is the quality guided 3D phase unwrapping algorithm (3DSRNCP) (23) and the other the Laplacian based phase unwrapping (18,35). For the comparison, the phase images were first unwrapped using these two algorithms and then processed using SHARP. The other parameters, such as the spherical kernel size and the regularization threshold were the same between SHARP and LSMV. Thus, the differences in the results were purely caused by the phase unwrapping algorithms. In order to evaluate the influences of different algorithms on the accuracy of susceptibility quantification, susceptibility maps were generated using the processed phase images, through truncated k-space division with a k-space threshold 0.1 (3).

For the simulated 3D brain model and cylinder data, the root-mean-square-errors (RMSEs) were calculated by comparing the processed phase images with the ideal phase without background phase or random noise. RMSEs were also calculated for the

generated susceptibility maps. For *in vivo* data, root-mean-square-deviations (RMSDs) was calculated for both processed phase images and susceptibility maps, by comparing the results obtained using LSMV and those obtained using the other two phase unwrapping algorithms. Specifically, the RMSEs for simulated data or RMSDs for *in vivo* data were calculated in two regions-of-interest (ROIs): all the regions inside the brain and the regions close to the veins. For evaluating the processed phase images, the second ROI consisted of both the regions inside the veins and the surrounding regions within 4 pixels to the veins (for the 3D cylinder simulation, the second ROI was a cylindrical region with radius 12 pixels, being concentric with the 3D cylinder); while for evaluating the generated susceptibility maps, the second ROI was taken to be the regions inside the veins (or cylinder) only. All the tests were performed in MATLAB R2010a on a desktop equipped with Intel i7-2600 CPU, 16 G of RAM.

4.4 Results

4.4.1 3D brain model simulation results

The RMSEs of the processed phase images generated using different algorithms were plotted in **Fig. 4.2**. For both the processed phase images and the susceptibility maps, LSMV and 3DSRNCP lead to almost the same RMSEs. When SNR was lower than 10, Laplacian phase unwrapping leads to slightly lower over-all RMSE, but higher RMSE for the veins, compared with the other two algorithms.

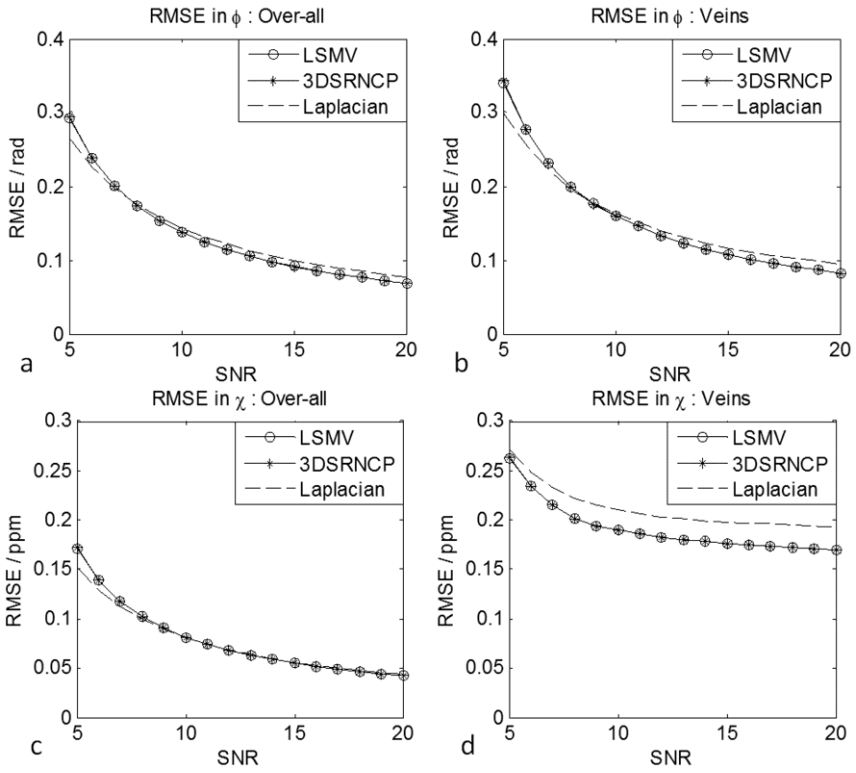

Figure 4.2 RMSEs of the processed phase images (**a** and **b**) and the susceptibility maps (**c** and **d**) at different noise levels for the simulated 3D brain model. The RMSEs in **a** and **c** were calculated using all the pixels inside the brain, while the RMSEs in **b** and **d** were calculated using only the pixels close to (or inside) the veins. The SNR represents the signal-to-noise ratio in the magnitude images.

The processing times using different algorithms were also measured, as shown in **Fig. 4.3**. For all noise levels, Laplacian phase unwrapping was the fastest among the three tested algorithms. When SNR was lower than 10, the proposed algorithm LSMV cost more time than 3DSRNCP. But for higher SNRs, the processing time for LSMV gradually reduced. This is due to the reduced number of noisy pixels in the phase images. At SNR=20:1, the processing time of LSMV was roughly 2/3 of that using 3DSRNCP.

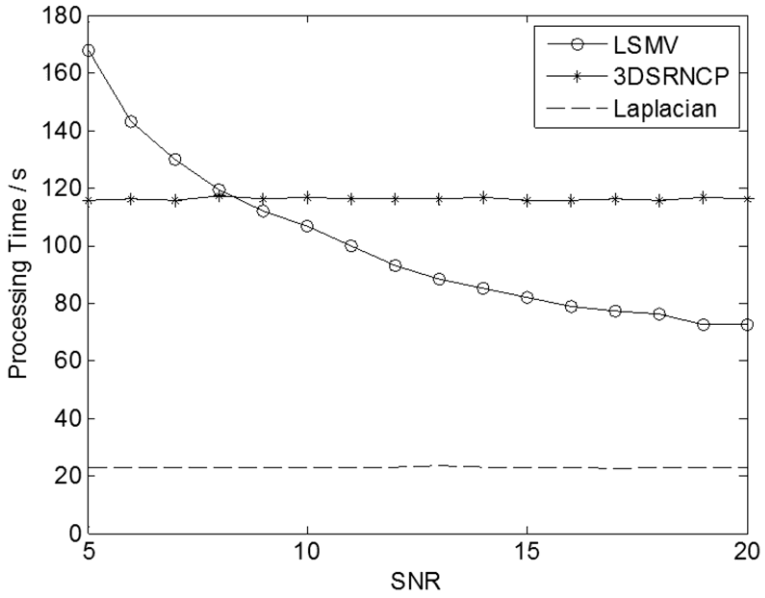

Figure 4.3 A comparison of the processing times using different algorithms at different noise levels.

4.4.2 Cylinder simulation results

The RMSEs in the phase images and susceptibility maps of the cylinders processed with different algorithms are plotted in **Fig. 4.4**. At both TEs, LSMV led to the smallest RMSEs among the three algorithms, for both the processed phase images and the susceptibility maps. When SNR was higher than 8, at both TEs, Laplacian phase unwrapping caused the largest RMSEs among the three algorithms, for both the processed phase images and the susceptibility maps. At TE_1, 3DSRNCP and LSMV induced similar level of RMSEs. At TE_2, when SNR was lower than 8, phase unwrapping using 3DSRNCP failed and this led to much larger RMSE in the processed phase images, as shown in **Figs. 4.4.b** and **4.5**. This error was propagated into the susceptibility maps, as indicated by the large RMSE in the susceptibility maps at TE_2 (**Fig. 4.4.d**).

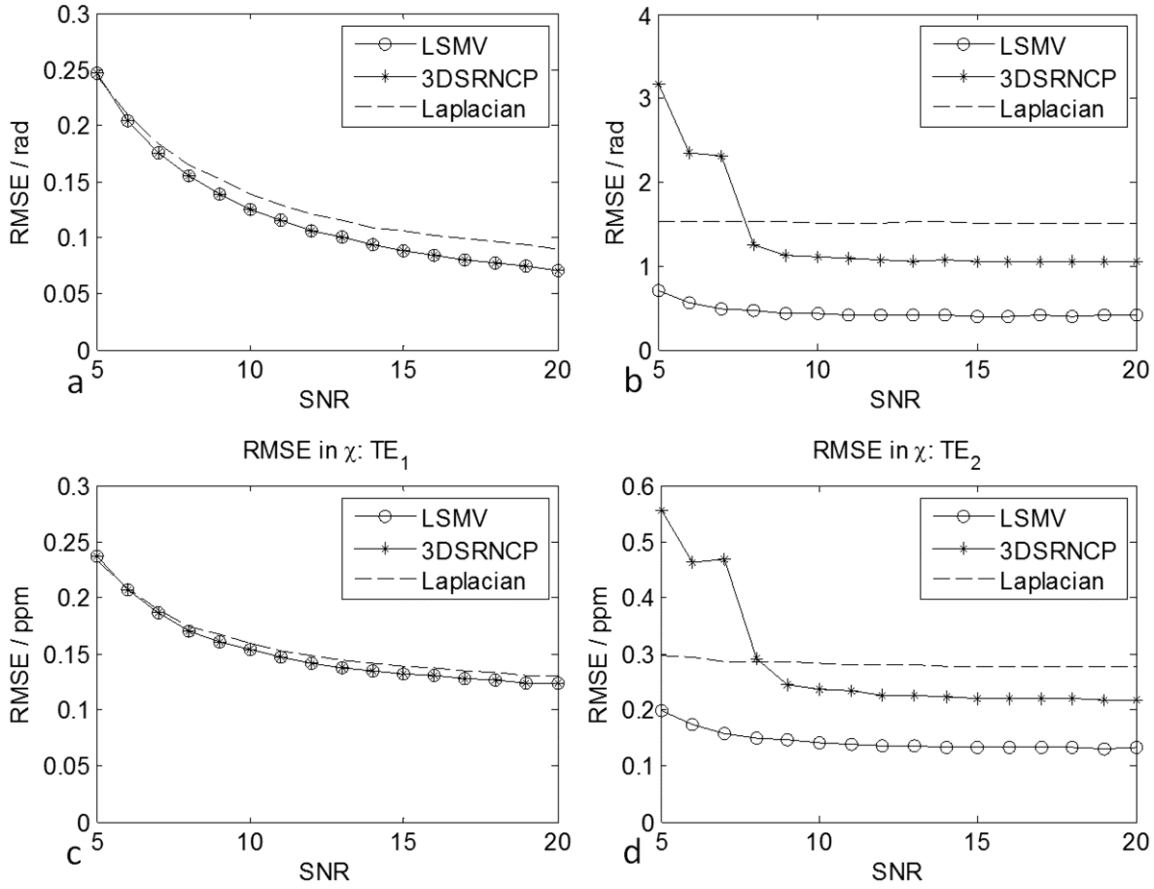

Figure 4.4 RMSEs in the processed phase images (**a** and **b**) and susceptibility maps (**c** and **d**) of the cylinders at two TEs. The SNR represents the signal-to-noise ratio in the magnitude images.

The original and the processed phase images of the cylinder are shown in **Fig. 4.5**. When SNR was 5:1, both 3DSRNCP and Laplacian phase unwrapping failed to unwrap the phase at TE_2. When SNR was 20:1, it was noticed that the 3DSRNCP failed to recover a few pixels at the edge of the cylinder, as indicated by the black arrows in **Fig. 4.5**. This is due to the low SNR at those pixels caused by T_2^* signal decay. The Laplacian phase unwrapping caused large error inside the cylinder at TE_2 again. On the other hand, for both

low and high SNRs, the LSMV algorithm had successfully extracted the local phase information for the cylinder.

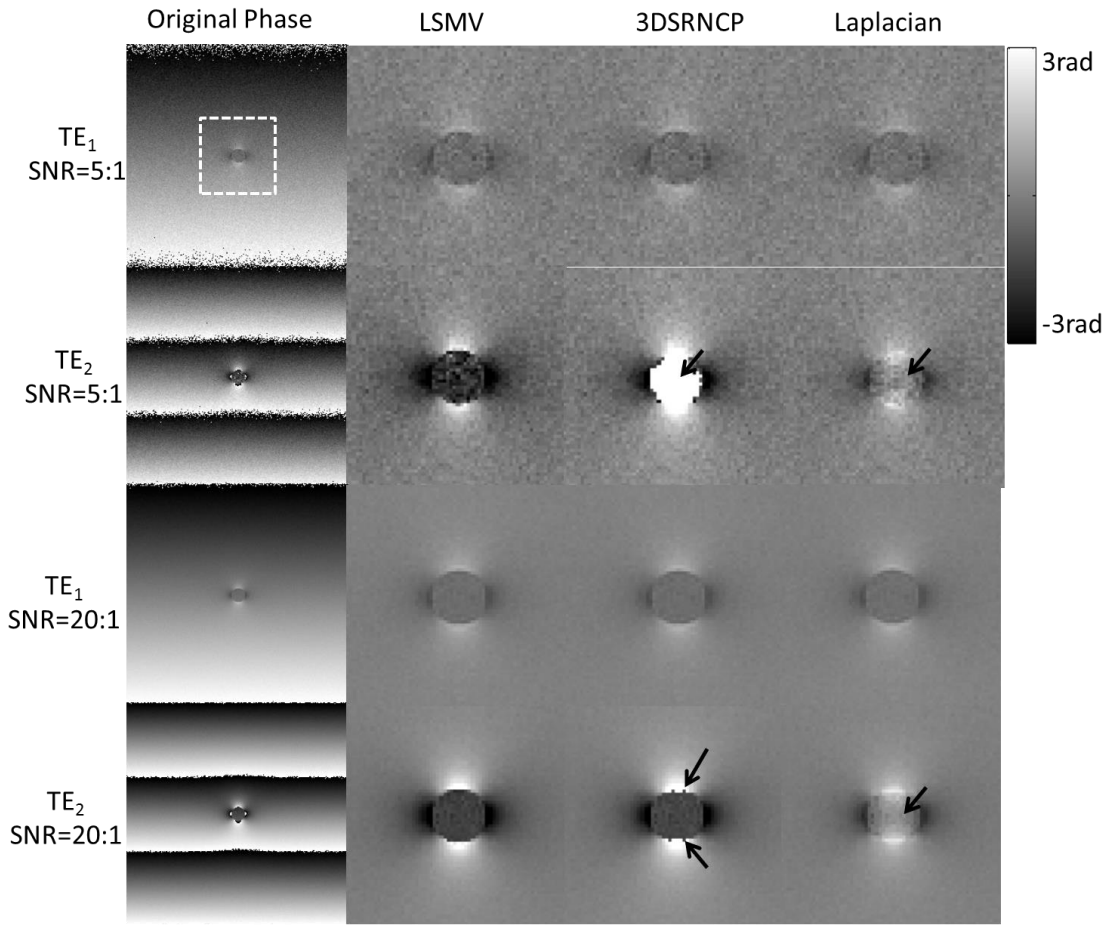

Figure 4.5 The original phase images and the local phase images generated using different algorithms for the simulated cylinder at SNR=5:1 and SNR=20:1. The SNR represents the signal-to-noise ratio in the magnitude images. The images in the second to fourth columns are the central 64×64 pixels in the processed local phase images, as indicated by the white dashed box in the top-left image. The errors in the local phase images obtained using 3DSRNCP and Laplacian phase unwrapping are indicated by the black arrows.

4.4.3 *In vivo* data results

The original and processed phase images, together with the SMV filtered images for Dataset 1 are shown in **Fig. 4.6**.

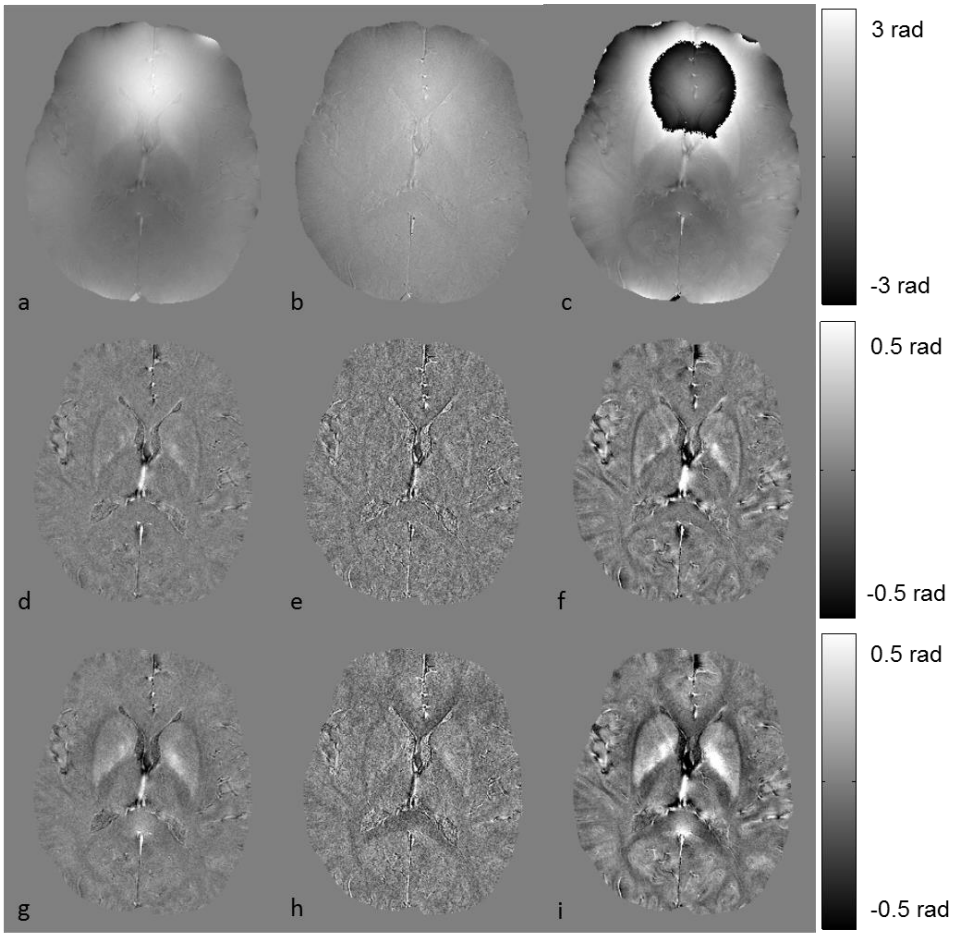

Figure 4.6 The original and processed phase images for **Dataset 1**. **a**) Original phase image at TE_1=7.38ms. **b**) Complex divided phase image with effective TE=2.84ms. **c**) Original phase images at TE_2=17.6ms. **d**) SMV filtered result (φ_{SMV}) at TE_1. **e**) SMV filtered result at ΔTE. **f**) SMV filtered result at TE_2, calculated using the images shown in ***e*** and ***d*** as ***e*+*2*×*d***. **g**) Local phase image at TE_1. **h**) Local phase image at ΔTE. **i**) local phase image at TE_2.

The LSMV led to almost the same local phase images as those obtained using 3DSRNCP, as shown in **Fig. 4.7**. The major difference between LSMV and 3DSRNCP is seen at the edges of the veins, especially at the longer TE, with the LSMV produced a more continuous phase profile. This continuous phase profile also helps to reduce the streaking artefacts in susceptibility maps, as shown in **Fig. 4.7.i**.

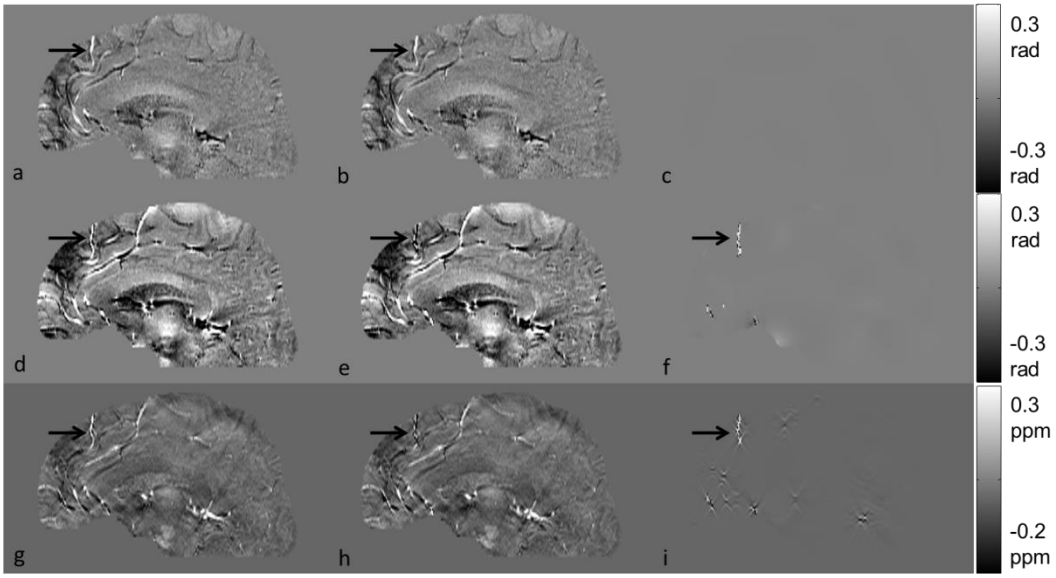

Figure 4.7 Comparison between the local phase images and susceptibility maps generated using LSMV (**a, d** and **g**) and those generated using 3DSRNCP (**b**, **e** and **h**) for Dataset 1. The difference images are shown in **c**, **f** and **i**. The phase images in the first row are at TE_1, and the phase images in the second row are at TE_2. The images in the third row are susceptibility maps (SM) obtained using the phase images at TE_2 (**d** and **e**). The scale bars are for the difference images **c**, **f** and **i** only. Note the improvement in the SM using LSMV thanks to the better recovery of phase around the veins.

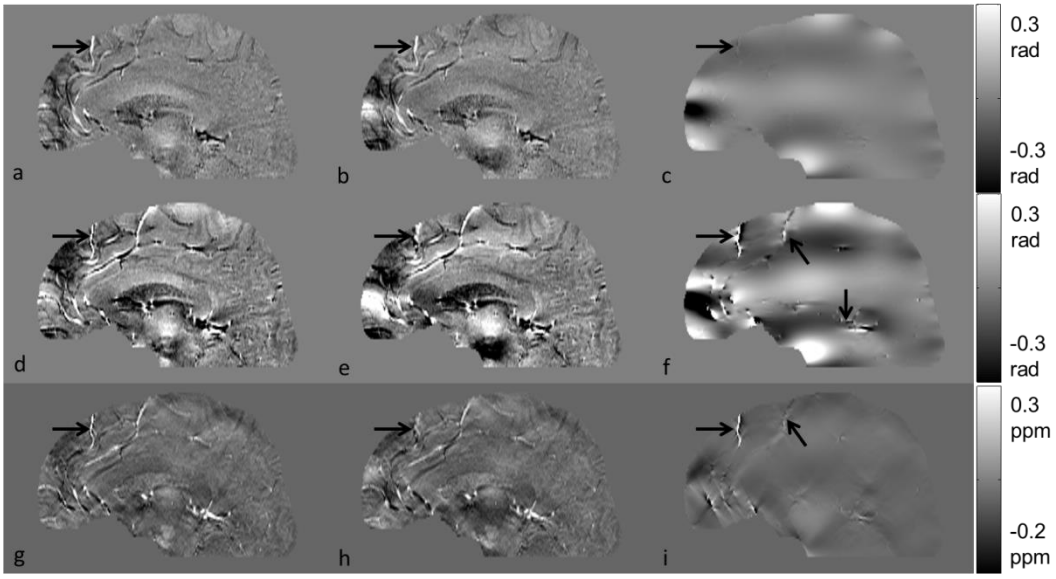

Figure 4.8 Comparison between the local phase images and susceptibility maps generated using LSMV (**a**, **d** and **g**), and those generated using Laplacian phase unwrapping (**b**, **e** and **h**) for Dataset 1. The difference images are shown in **c**, **f** and **i**. The phase images in the first row are at TE_1, and the phase images in the second row are at TE_2. The images in the third row are susceptibility maps obtained using the phase images at TE_2 (**d** and **e**). The scale bars are for the difference images **c**, **f** and **i** only.

Compared with the LSMV generated results, the Laplacian phase unwrapping caused remnant low spatial-frequency background field, especially for regions close to the air-tissue interfaces, as shown in **Fig 4.8**. Large differences were also seen at the edges of the veins. This could be due to the partial volume effects and discretization errors.

The quantitative measures of the differences between different phase processing methods for all the *in vivo* data are shown in **Table 4.2**. For all three datasets, the processed phase images at TE_1 obtained using LSMV are almost the same as those obtained using the

3DSRNCP. However, the processed phase images at TE_2 show a slight difference between LSMV and 3DSRNCP. This may be due to the difference of the pixels at the edges of the veins, caused by T_2^* signal decay. This difference in the processed phase images was propagated into the difference in susceptibility maps, especially for the vein regions. Meanwhile, a relatively large difference was seen between the processed phase images obtained using Laplacian phase unwrapping and those obtained using LSMV. This also caused a large difference between the susceptibility maps. As for the processing time, still Laplacian phase unwrapping with SHARP was the fastest among the three. The time cost by LSMV for processing the phase images at two TEs was close to the time cost by 3DSRNCP for processing the phase images at a single TE.

The proposed algorithm LSMV is able to handle noisy phase images and reduce the effects of the cusp artefacts. Signal cancelation and cusp artefacts occur when the multi-channel phase data is not combined properly. As an example, in **Fig. 4.9.a,** we show the original phase images at TE_2 from Dataset 2, combined using the built-in algorithm on the scanner. The improper combination caused cusp artefacts and locally severely reduced SNR on the phase images, as indicated by the white arrows in **Fig. 4.9**. The cusp artefact caused failure of phase unwrapping using 3DSRNCP (**Fig. 4.9.b**), which was propagated into the extracted local phase images (**Fig. 4.9.e**). On the other hand, both LSMV and Laplacian phase unwrapping handled the cusp artefact properly (**Fig. 4.9.d** and **4.9.f**).

Table 4.2 A comparison of phase images and susceptibility maps processed using different algorithms for the *in vivo* data.

		Dataset 1		Dataset 2		Dataset 3	
		TE1	TE2	TE1	TE2	TE1	TE2
RMSD in Phase Images: Overall (in rad)	LSMV vs. 3DSRNCP+SHARP	0	0.04	0	0.07	0	0.07
	LSMV vs. Laplacian+SHARP	0.05	0.13	0.02	0.09	0.02	0.09
RMSD in Phase Images: Veins (in rad)	LSMV vs. 3DSRNCP+SHARP	0.03	0.20	0.04	0.46	0	0.46
	LSMV vs. Laplacian+SHARP	0.06	0.24	0.05	0.47	0.03	0.45
RMSD in Susceptibility Maps: Overall (in ppm)	LSMV vs. 3DSRNCP+SHARP	0	0.01	0	0.01	0	0.01
	LSMV vs. Laplacian+SHARP	0	0.02	0	0.02	0	0.02
RMSD in Susceptibility Maps: Veins (in ppm)	LSMV vs. 3DSRNCP+SHARP	0.02	0.11	0.02	0.18	0	0.15
	LSMV vs. Laplacian+SHARP	0.02	0.12	0.01	0.18	0	0.15
Processing time (s)	LSMV	44 (two TEs)		28(two TEs)		26(two TEs)	
	3DSRNCP+SHARP	32	31	20	20	20	20
	Laplacian+SHARP	7	7	4	4	4	4

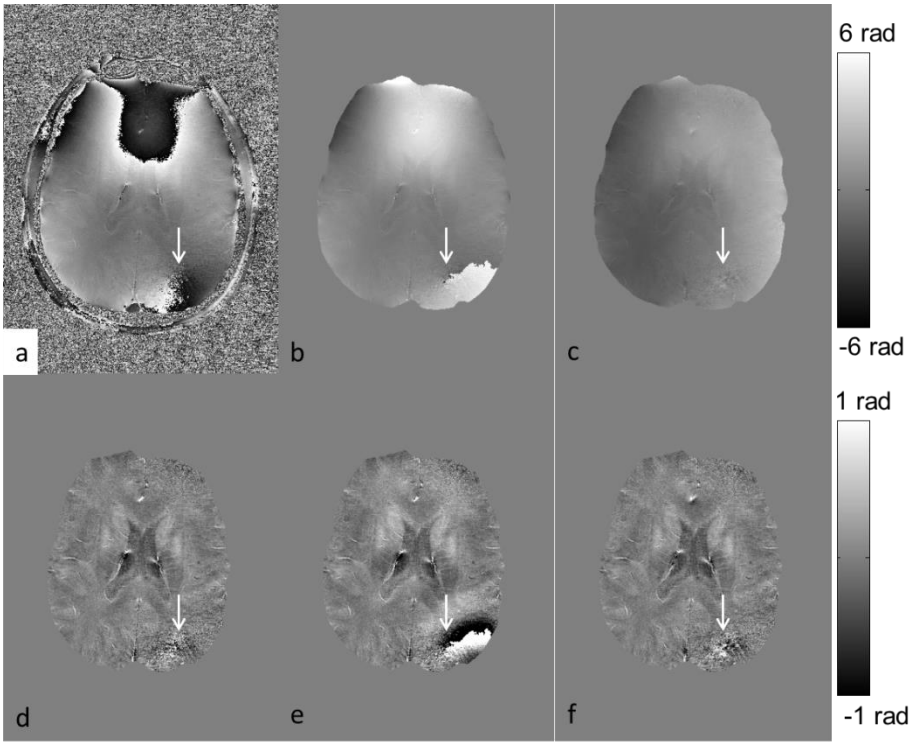

Figure 4.9 a) Original phase image at TE_2 from Dataset 2 with cusp artefact. Note that, this image was obtained using the built-in multi-channel data combination algorithm on the scanner. **b)** Unwrapped phase image using 3DSRNCP. **c)** Unwrapped phase image using Laplacian phase unwrapping. **d)** Local phase image generated using LSMV. **e)** Local phase image generated using the unwrapped phase image shown in **b**. **f)** Local phase image obtained using the unwrapped phase image shown in **c**. Cusp artefact caused errors in the processed phase images, as indicated by the white arrows.

4.5 Discussion

Background field removal in QSM could be affected by several factors. The robustness of background field removal is usually hampered by the requirement of phase unwrapping, especially for phase images at a relatively long TE. For short TE phase images, however, most regions inside the brain are not affected by phase aliasing. Thus the short TE's phase images could be used to accelerate the processing of the phase images at a longer TE. While the shorter TE's phase has less T_2^* decay induced noisy pixels, the longer TE's phase has higher overall phase SNR. The signal loss due to T_2^* signal decay could be reduced by projecting the phase obtained at the shorter TE to a longer TE. It was shown that the effective magnetic moment is constant (36). Thus, recovering the lost pixels near the edge of the veins is important, since these pixels will affect the estimation of the geometries of the veins and consequently affect the estimation of susceptibility. This is the main advantage of using a combination of short TE and long TE in a double-echo sequence.

Multi-channel phase data combination also plays an indispensable role in QSM. For phase data collected with a multi-channel phased array coil, a simple weighted sum of the complex data usually leads to severe signal cancelation and cusp artefacts in the phase images (13,14), which will deteriorate the accuracy of background field removal. This problem is attributed to the coil sensitivity induced phase component in different channel's data (13-15), and can be partly solved by applying high-pass filtering to each channel's phase data before the data combination. But the combined phase data will be effectively high-pass filtered and this in turn will lead to under-estimation of the susceptibilities (14).

A correction of the constant baseline shifts for different channel's data is an effective way to alleviate the problem (13). However, the accuracy of the baseline shift correction is also dependent on the selection of the reference region that is used for estimating the phase baseline shifts between channels (14). In a recently proposed method, the coil sensitivity induced phase components were estimated using reference scan or double-echo data and subsequently removed before combining the data from different channels (14). Instead of using the combined phase data, the phase data from individual channels can also be used directly in QSM processing, followed by weighted average of the susceptibility maps (37). The latter two methods are more sophisticated, but are computationally more extensive, since both of them requires phase unwrapping or background field removal for each channel's phase data. From our experiences, if the focus is the brain, linear gradients and baseline correction for each channel's phase will be sufficient to avoid any cusp artefacts or signal cancelation in phase images. The selection of a reference channel can be avoided, if the baseline of each channel is estimated from the center of k-space.

The time cost by background field removal is mainly determined by the phase unwrapping process. For the currently available phase unwrapping algorithms, the processing time varies a lot, so does the robustness of these algorithms (12).

The Laplacian phase unwrapping is the most time-efficient. However, no matter whether a Laplacian operator is directly used to remove the background field, or the phase is unwrapped first using Laplacian followed by other background field removal algorithms, errors are usually found in the extracted local phase information, especially for the regions near the edge of the veins. This is attributed to discretization errors in calculating the

Laplacian of phase (11,17,25). Despite its inability in producing reliable phase for the veins, Laplacian phase unwrapping is usually found to be a robust algorithm, especially when there are cusp artefacts in the phase images.

On the other hand, the 3D path-following and quality guided phase unwrapping algorithms are able to produce relatively more reliable phase information, especially for the veins, even though these phase unwrapping algorithms are usually time-consuming. Particularly, when there are cusp artefacts, these phase unwrapping algorithms will eventually fail (15,17), as validated in this study.

The proposed LSMV algorithm leads to almost the same results as those 3D quality guided phase unwrapping algorithms, with the advantage that phase singularities and noisy pixels are properly handled. For processing the phase images at two TEs, the time cost by LSMV is roughly half of the time cost by the fast 3D phase unwrapping algorithm.

The effectiveness of the proposed algorithm is dependent on the TEs used in the double-echo sequence. A proper combination of the TEs should satisfy the following conditions. First, the TE of the first echo should be short enough, so that only a few pixels close to the air-tissue interfaces need to be removed due to too rapid field changes. This helps to reduce the loss of the regions close to the air-sinuses. Second, the TE of the second echo should not be too far away from the first TE. i.e., the values of α in Eq. 4.9 should not be too big. A bigger α means more complex divisions using the phase images at the two TEs, and hence more amplification of the random noise in the phase images. Under the above two conditions, and assuming that the effective TE of the complex divided phase, $0 < \Delta TE \leq TE_1$, we have $TE_2 - \alpha TE_1 \leq TE_1$, or $TE_2 \leq (1+\alpha)TE_1$. The lower bound of

TE_2 is usually restricted by the requirement of applying the flow compensation gradient. This restriction can be removed by using an interleaved double-echo sequence (21), but with prolonged scan time. In the cases when two relatively long TEs (with short TE spacing) are used, temporal phase unwrapping can be achieved by projecting the phase at the short effective TE to a much longer TE, as proposed in former studies (19,20). However, the accuracy of the processed phase at the longer TE may be compromised by the amplification of noise due to the projection.

The quality of SHARP processed phase images is also dependent on the deconvolution process as shown in Eq. 4.8. In this study, we used the truncated k-space division for the deconvolution, due to its simplicity and time-efficiency. The deconvolution could also be done through a Tikhonov regularization process (29). It should be noted that the SMV filtered results generated from this algorithm can be easily used as the input to other deconvolution algorithms to further improve the accuracy of background field removal.

In addition, the phase component ϕ_0 could be used to extract the conductivity of different tissues (26,27). For the purpose of QSM, the effects of ϕ_0 should also be considered, since it may not satisfy the Laplace's equation and thus may not be fully suppressed by the spherical mean value filtering. For the algorithm proposed in this study, the effects of ϕ_0 can be determined through a linear fitting using the processed phase images. Ideally, ϕ_0 should be determined even before the phase images were processed (14). ϕ_0 can be determined through a weighted linear fitting using multiple echoes, but it was also shown in a previous study that nonlinear fitting of the phase may help to avoid any noise amplification at longer echo times (16).

Finally, the limitations to the proposed method are mainly associated with the regions near the sinuses, where the field is changing too rapidly. These regions cannot be fully resolved using baseline shifting or local complex division. Current techniques of using a forward model to remove more of the air/tissue interface would reduce the rapid field variations and hence make it possible to apply this new approach even in those regions.

In conclusion, using the proposed algorithm based on double-echo data, global phase unwrapping is avoided and the noisy pixels in phase images (e.g., phase singularities/cusp artefacts) are better handled. This improves the efficiency and robustness of background field removal in QSM.

References

1. Bilgic B, Pfefferbaum A, Rohlfing T, Sullivan EV, Adalsteinsson E. MRI estimates of brain iron concentration in normal aging using quantitative susceptibility mapping. NeuroImage 2012;59:2625–35.
2. Li W, Wu B, Batrachenko A, Bancroft-Wu V, Morey RA, Shashi V, et al. Differential developmental trajectories of magnetic susceptibility in human brain gray and white matter over the lifespan. Hum. Brain Mapp. 2013;
3. Haacke EM, Tang J, Neelavalli J, Cheng YC. Susceptibility mapping as a means to visualize veins and quantify oxygen saturation. J. Magn. Reson. Imaging 2010;32:663–76.
4. Fan AP, Bilgic B, Gagnon L, Witzel T, Bhat H, Rosen BR, et al. Quantitative oxygenation venography from MRI phase. Magn. Reson. Med. 2013; DOI: 10.1002/mrm.24918
5. Schweser F, Deistung A, Lehr BW, Reichenbach JR. Differentiation between diamagnetic and paramagnetic cerebral lesions based on magnetic susceptibility mapping. Med. Phys. 2010;37:5165.
6. Liu T, Surapaneni K, Lou M, Cheng L, Spincemaille P, Wang Y. Cerebral microbleeds: burden assessment by using quantitative susceptibility mapping. Radiology 2012;262:269–78.
7. Haacke EM, Xu Y, Cheng YN, Reichenbach JR. Susceptibility weighted imaging (SWI). Magn. Reson. Med. 2004;52:612–8.
8. Neelavalli J, Cheng YN, Jiang J, Haacke EM. Removing background phase variations in susceptibility-weighted imaging using a fast, forward-field calculation. J. Magn. Reson. Imaging 2009;29:937–48.
9. Liu T, Khalidov I, de Rochefort L, Spincemaille P, Liu J, Tsiouris AJ, et al. A novel background field removal method for MRI using projection onto dipole fields (PDF). NMR Biomed. 2011;24:1129–36.
10. Schweser F, Deistung A, Lehr BW, Reichenbach JR. Quantitative imaging of intrinsic magnetic tissue properties using MRI signal phase: An approach to in vivo brain iron metabolism? NeuroImage 2011;54:2789–807.
11. Li W, Avram AV, Wu B, Xiao X, Liu C. Integrated Laplacian-based phase unwrapping and background phase removal for quantitative susceptibility mapping. NMR Biomed. 2013; DOI: 10.1002/nbm.3056.
12. Li N, Wang W-T, Sati P, Pham DL, Butman JA. Quantitative assessment of susceptibility-weighted imaging processing methods. J. Magn. Reson. Imaging 2013; DOI: 10.1002/jmri.24501.
13. Hammond KE, Lupo JM, Xu D, Metcalf M, Kelley DAC, Pelletier D, et al. Development of a robust method for generating 7.0 T multichannel phase images of the brain with application to normal volunteers and patients with neurological diseases. NeuroImage 2008;39:1682–92.

14. Robinson S, Grabner G, Witoszynskyj S, Trattnig S. Combining phase images from multi-channel RF coils using 3D phase offset maps derived from a dual-echo scan. Magn. Reson. Med. 2011;65:1638–48.
15. Haacke EM, Reichenbach JR, editors. Susceptibility Weighted Imaging in MRI: Basic Concepts and Clinical Applications. 1st ed. Wiley-Blackwell; 2011.
16. Liu T, Wisnieff C, Lou M, Chen W, Spincemaille P, Wang Y. Nonlinear formulation of the magnetic field to source relationship for robust quantitative susceptibility mapping. Magn. Reson. Med. 2013;69:467–76.
17. Schweser F, Deistung A, Sommer K, Reichenbach JR. Toward online reconstruction of quantitative susceptibility maps: superfast dipole inversion. Magn. Reson. Med. 2013;69:1582–94.
18. Ghiglia DC, Pritt MD. Two-dimensional phase unwrapping: theory, algorithms, and software. Wiley; 1998.
19. Feng W, Neelavalli J, Haacke EM. Catalytic multiecho phase unwrapping scheme (CAMPUS) in multiecho gradient echo imaging: removing phase wraps on a voxel-by-voxel basis. Magn. Reson. Med. 2013;70:117–26.
20. Robinson S, Schödl H, Trattnig S. A method for unwrapping highly wrapped multi-echo phase images at very high field: UMPIRE. Magn. Reson. Med. 2013; doi: 10.1002/mrm.24897
21. Ye Y, Hu J, Wu D, Haacke EM. Noncontrast-enhanced magnetic resonance angiography and venography imaging with enhanced angiography. J. Magn. Reson. Imaging 2013;38:1539–48.
22. Jenkinson M. Fast, automated, N-dimensional phase-unwrapping algorithm. Magn. Reson. Med. 2003;49:193–7.
23. Abdul-Rahman HS, Gdeisat MA, Burton DR, Lalor MJ, Lilley F, Moore CJ. Fast and robust three-dimensional best path phase unwrapping algorithm. Appl. Opt. 2007;46:6623–35.
24. Witoszynskyj S, Rauscher A, Reichenbach JR, Barth M. Phase unwrapping of MR images using Phi UN--a fast and robust region growing algorithm. Med. Image Anal. 2009;13:257–68.
25. Li W, Wu B, Liu C. Quantitative susceptibility mapping of human brain reflects spatial variation in tissue composition. NeuroImage 2011;55:1645–56.
26. Haacke EM, Petropoulos LS, Nilges EW, Wu DH. Extraction of conductivity and permittivity using magnetic resonance imaging. Phys. Med. Biol. 1991;36:723.
27. Kim D-H, Choi N, Gho S-M, Shin J, Liu C. Simultaneous imaging of in vivo conductivity and susceptibility. Magn. Reson. Med. 2013; doi: 10.1002/mrm.24759
28. Li L, Leigh JS. High-precision mapping of the magnetic field utilizing the harmonic function mean value property. J. Magn. Reson. 1997 2001;148:442–8.
29. Sun H, Wilman AH. Background field removal using spherical mean value filtering and Tikhonov regularization. Magn. Reson. Med. 2013; DOI: 10.1002/mrm.24765
30. Salomir R, de Senneville BD, Moonen CT. A fast calculation method for magnetic field inhomogeneity due to an arbitrary distribution of bulk susceptibility. Concepts Magn. Reson. Part B Magn. Reson. Eng. 2003;19B:26–34.

31. Marques J p., Bowtell R. Application of a Fourier-based method for rapid calculation of field inhomogeneity due to spatial variation of magnetic susceptibility. Concepts Magn. Reson. Part B Magn. Reson. Eng. 2005;25B:65–78.
32. Koch KM, Papademetris X, Rothman DL, de Graaf RA. Rapid calculations of susceptibility-induced magnetostatic field perturbations for in vivo magnetic resonance. Phys. Med. Biol. 2006;51:6381–402.
33. Smith SM. Fast robust automated brain extraction. Hum. Brain Mapp. 2002;17:143–55.
34. Cusack R, Papadakis N. New Robust 3-D Phase Unwrapping Algorithms: Application to Magnetic Field Mapping and Undistorting Echoplanar Images. NeuroImage 2002;16:754–64.
35. Schofield MA, Zhu Y. Fast phase unwrapping algorithm for interferometric applications. Opt. Lett. 2003;28:1194–6.
36. Liu S, Neelavalli J, Cheng YCN, Tang J, Mark Haacke E. Quantitative susceptibility mapping of small objects using volume constraints. Magn. Reson. Med. 2013;69:716–23.
37. Wu B, Li W, Guidon A, Liu C. Whole brain susceptibility mapping using compressed sensing. Magn. Reson. Med. 2012;67:137–47.

Chapter 5 Solving the Inverse Problem of Susceptibility Quantification

5.1 Susceptibility mapping using truncated k-space division

5.1.1 Theory

As previously discussed in Chapters 2 and 3, the field variation in the main field direction can be considered as the convolution of the susceptibility distribution and the point-dipole field response (the Green's function) as (1,2):

$$\Delta B_z(\vec{r}) = B_0 \chi(\vec{r}) * G(\vec{r}) \quad [5.1].$$

The main field direction is assumed to be in z direction. This convolution can be calculated through convolution theorem by taking the Fourier transform of Eq. 5.1:

$$\Delta B_z(\vec{k}) = B_0 \chi(\vec{k}) G(\vec{k}) \quad [5.2].$$

The Fourier transform of the Green's function, $G(\vec{k})$, has a simple form of $1/3 - k_z^2/k^2$, when $\vec{k} \neq 0$. $G(\vec{k}) = 0$, when $\vec{k} = 0$ (1–3).

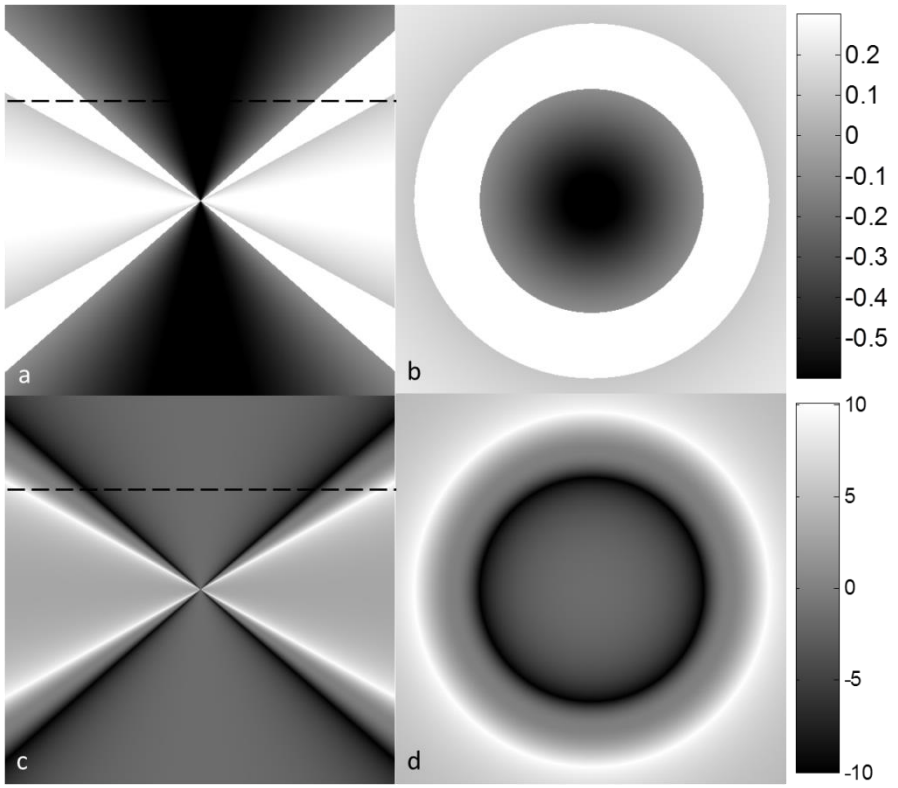

Figure 5.1 The cross-sections of $G(\vec{k})$ (**a** and **b**) and $G'^{-1}(\vec{k})$ (**c** and **d**). In **a** and **c**, the cross-sections are parallel to the main field direction, in **b** and **d**, the cross-sections are perpendicular to the main field direction. The white regions in **a** and **b** correspond to the regions where $|G(\vec{k})| < 0.1$. The black dashed lines in **a** and **c** indicate the positions of the cross-sections shown in **b** and **d**.

Susceptibility quantification is the inverse problem, in which Eq. 5.1 is solved for $\chi(\vec{r})$, given $\Delta B_z(\vec{r})$. The inverse problem is ill-posed, due to the zeros in the Green's function in Fourier domain. This inverse problem can be solved by using a regularized inverse filter(4), $G'^{-1}(\vec{k})$, defined as:

$$G'^{-1}(\vec{k}) = \begin{cases} \left(\frac{1}{3} - \frac{k_z^2}{k^2}\right)^{-1}, & when \left|\frac{1}{3} - \frac{k_z^2}{k^2}\right| > th \\ sgn\left(\frac{1}{3} - \frac{k_z^2}{k^2}\right)\left(\frac{1}{3} - \frac{k_z^2}{k^2}\right)^2 th^{-3}, & when \left|\frac{1}{3} - \frac{k_z^2}{k^2}\right| \leq th. \end{cases} \quad [5.3].$$

The cross-sections of $G(\vec{k})$ and $G'^{-1}(\vec{k})$ are shown in **Fig. 5.1**.

The regularized inverse filtering leads to two problems: streaking artefacts and underestimation of the susceptibility (4,5). Consequently, the choice of the regularization threshold is usually a trade-off between the level of the streaking artefact and the underestimation of the susceptibility.

The systematic underestimation can be estimated, as proposed in (6). Consider the ideal solution to the inverse problem as:

$$\chi_{ideal}(\vec{k}) = \frac{\Delta B(\vec{k})}{B_0 G(\vec{k})} \quad [5.4],$$

and the solution using the regularized inverse kernel as:

$$\chi_{reg}(\vec{k}) = \frac{\Delta B(\vec{k})}{B_0} G'^{-1}(\vec{k}) \quad [5.5],$$

From Eqs. 5.4 and 5.5,

$$\frac{\chi_{reg}(\vec{k})}{\chi_{ideal}(\vec{k})} = G'^{-1}(\vec{k}) G(\vec{k}) \quad [5.6].$$

If the systematic underestimation was considered as a constant scaling factor in image domain, using the inverse Discrete Fourier Transform, it could be estimated as the average value of $G'^{-1}(\vec{k})G(\vec{k})$.

5.1.2 Optimal choice of the regularization threshold

In order to determine the optimal choice of the regularization threshold (*th* in Eq. 5.3), cylinders with different radii ranging from 2 pixels to 16 pixels were simulated in a 256×256 matrix, at B_0=3T, TE=5ms. The susceptibility of the cylinders was set to 1 ppm. Partial volume effects were simulated by first creating the complex data in a 4096×4096 matrix, and then cropping the central 256×256 pixels in k-space. Gaussian noise was added to real and imaginary channels of the complex data and the SNR in the magnitude images ranged from 2:1 to 20:1. Means and standard deviations of the susceptibilities of the both the regions inside and outside the cylinder were measured.

When no random noise was added, the level of underestimation as a function of the regularization threshold *th* is plotted in **Fig. 5.2.a** and **5.2.b**, for cylinders with different radii. When *th* is small, the predicted underestimation (**Figure 5.2.a**) agrees better with the measured underestimation of the relatively bigger cylinders; when *th* gets bigger, the predicted underestimation agrees better with the measured underestimation of the smaller cylinders. The underestimation of the susceptibilities of the cylinders is increasing as the threshold value *th* increases, while the uncertainty is decreasing.

When different levels of random noise were added, the levels of underestimation for different cylinders were almost the same as those when no noise was added, as can be seen from **Figure 5.2.c** and **5.2.e**. It was also noticed that, for the smallest cylinder, when *th* is low, there could be a significant increase of the level of underestimation, as indicated in **Figure 5.2.c**. and **5.2.e**. The standard deviations of the measured susceptibilities inside

the cylinders were increased (**Fig. 5.2.d** and **5.2.f**), compared with the standard deviations inside the cylinders without any random noise (**Fig. 5.2.b**).

The measured susceptibilities of the regions outside the cylinders are mainly attributed to streaking artefacts and Gibbs ringing. As shown in **Fig. 5.3.a** and **5.3.b**, the mean and standard deviations of the susceptibility values measured outside the cylinders were close to 0, but the standard deviation can be quite large when random noise was added and when *th* is small (**Fig. 5.3.d**and **5.3.f**). The standard deviation measured outside the cylinders quickly decreases as *th* increases.

In order to find the optimal threshold value, with the standard deviation outside the cylinders used as a measure of the level of streaking artefacts, a cost function could be defined as:

$$R(th) = \sqrt{U(th)^2 + N(th)^2} \qquad [5.7],$$

where U(*th*) is the underestimation as a function of *th*, for cylinder with certain radius r, and for a certain SNR; N(*th*) is the standard deviation measured outside the cylinder. The function R(*th*) is plotted in **Fig. 5.4**, for cylinders with different radii. The optimal *th* can be selected as the one which minimizes the cost function R(*th*). The optimal *th* was found to be close to 0.1 for small structures and 0.14 for relatively bigger structures. Besides of underestimation, bigger structures may also lead to blurring of the susceptibility maps (5,6). Consequently, 0.1 is the over-all optimal *th* when structures with different sizes are considered.

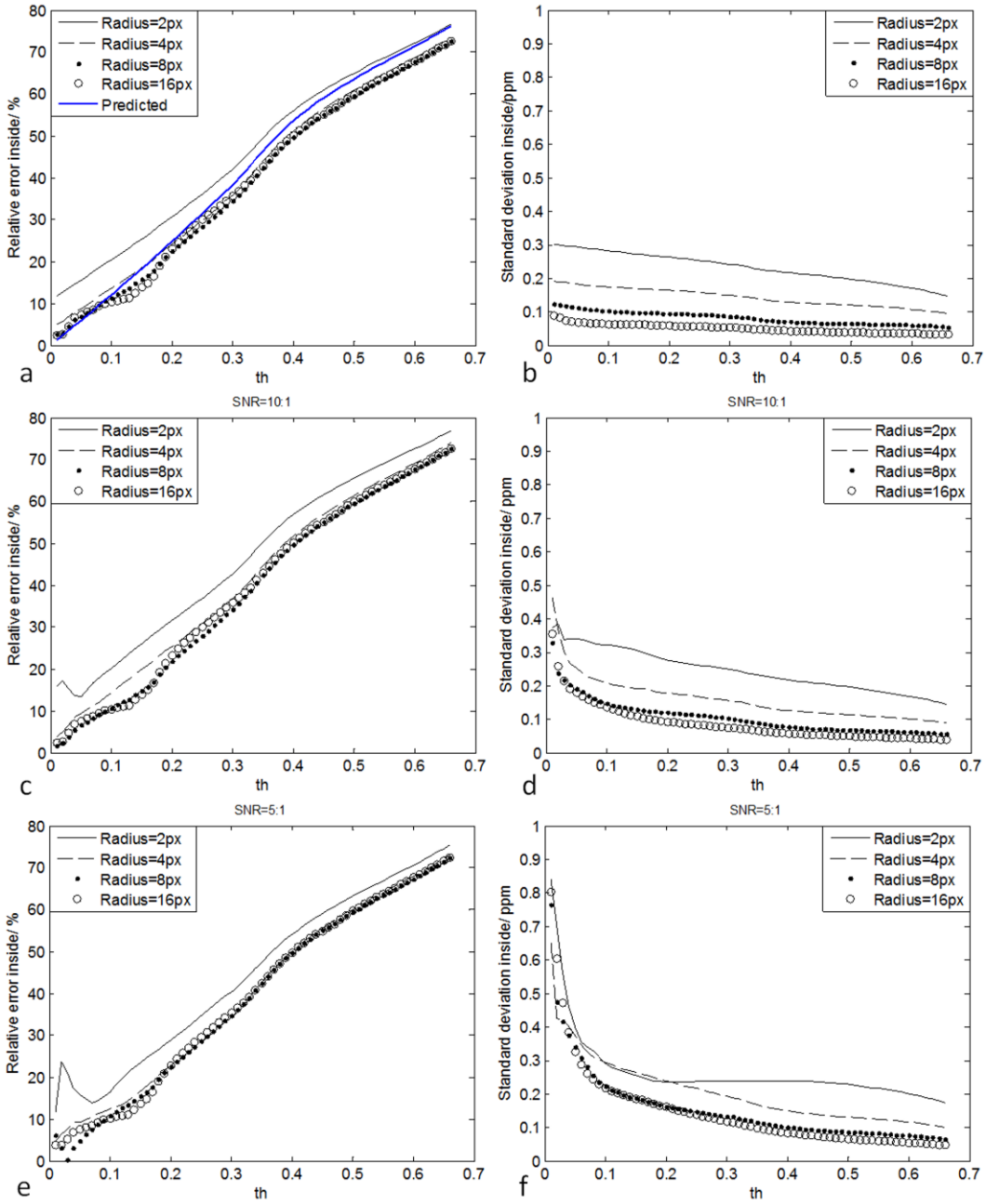

Figure 5.2 The underestimation in the susceptibility values measured inside the cylinders with different radii (**a, c** and **e**) and the standard deviations (**b, d** and **f**). **a** and **b** were generated when no noise was added. For **c** and **d**, SNR=10:1 in the magnitude images; while for **e** and **f**, SNR=5:1.

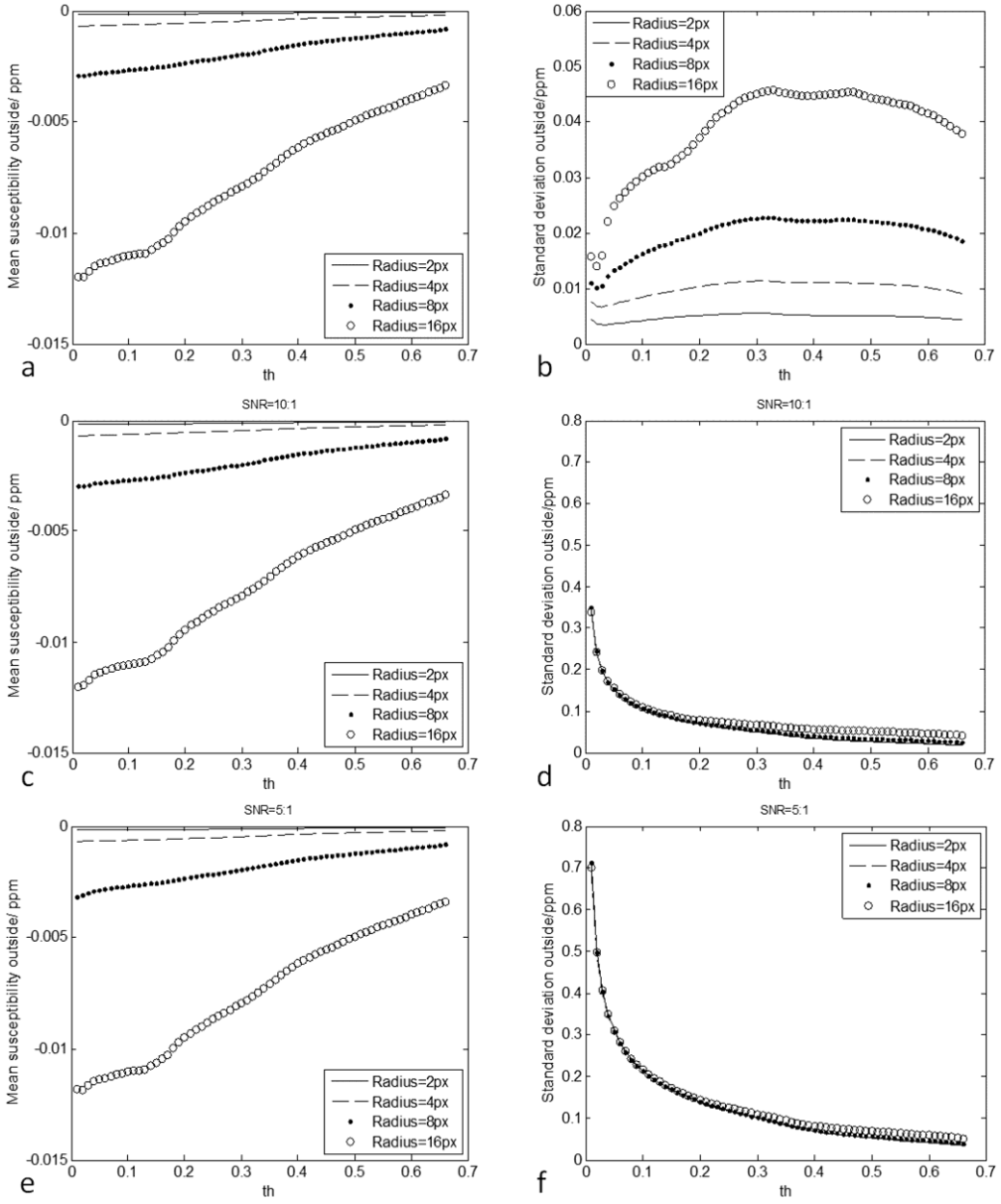

Figure 5.3 The mean susceptibility values (**a**, **c** and **e**) and the standard deviations (**b**, **d** and **f**) measured in the background regions outside the cylinders. **a** and **b** were generated when no noise was added. For **c** and **d**, SNR=10:1 in the magnitude images; while for **e** and **f**, SNR=5:1.

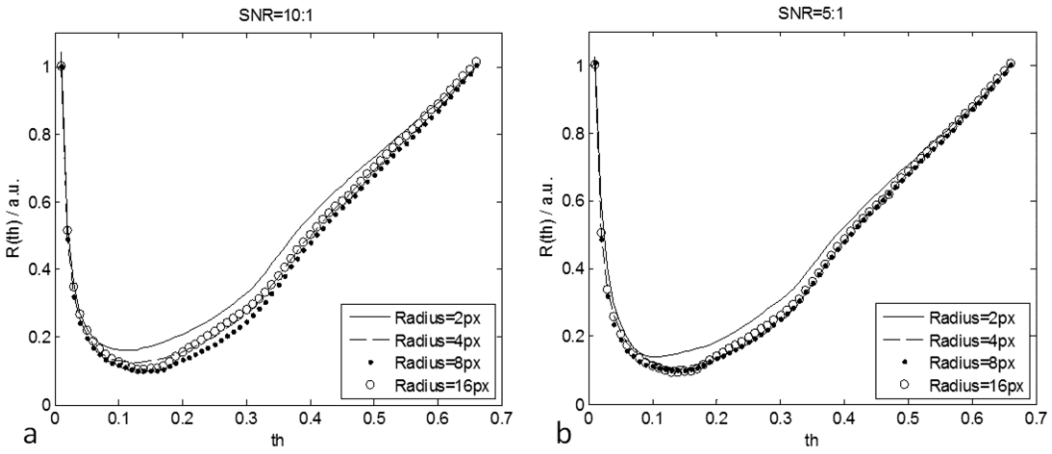

Figure 5.4 The cost function R(*th*) for different cylinders. R(*th*) was calculated using **Eq. 5.7**. The optimal *th* was determined as when *R(th)* was minimized. Particularly, when SNR=10:1, the optimal *th*s were 0.12 (r=2px), 0.13(r=4px), 0.14 (r=8px), and 0.14 (r=16px). When SNR=5:1, the optimal *th*s were 0.1 (r=2px), 0.13(r=4px), 0.13 (r=8px), and 0.14 (r=16px).

5.2 Geometry constrained iterative reconstruction

5.2.1 Theory and methods

Even though the regularized inverse filtering helps to avoid amplification of the noise, the streaking artefacts are inevitable and they may severely affect the quality of susceptibility maps. In order to obtain susceptibility maps with reduced streaking artefacts, additional information such as the geometries obtained from magnitude or phase images can be used as constraints, and the inverse problem could be formularized as an optimization process (7–9):

$$argmin_{\chi(\vec{r})}\{\left\|W\left(\Delta B_z(\vec{r}) - \chi(\vec{r}) * G(\vec{r})\right)\right\|_2^2 + \lambda \cdot R(\chi)\} \quad [5.8],$$

where W is a weighting function and $R(\chi)$ is the regularization function. The first part of Eq. 5.8 is related to data fidelity and the second part of Eq. 5.8 is related to regularization. When $\lambda = 0$, Eq. 5.8 reduces to a least-squares fit (3). The $R(\chi)$ is usually taken to be the L^p-norm the gradients of the susceptibility maps within a low-gradient mask, M_{geo}.

$$R(\chi) = ||M_{geo}\nabla\chi||_p \quad [5.9].$$

The low-gradient mask could be generated by setting threshold to the gradients found in magnitude images (7), gradients and Laplacian of the phase images, or a combination of both the gradients in magnitude and phase images (8). The optimization problem in Eq. 5.8 can be solved using iterative solvers such as LSQR in Matlab (10). Alternatively, a k-space/image domain iterative algorithm, referred to as iterative SWIM, can be used.

The main idea of iterative SWIM is to reduce the streaking artefacts associated with structures with relatively high susceptibility values and to update the k-space data in the singularity regions (i.e., where $\left|G\left(\vec{k}\right)\right| < th$). The iterative SWIM algorithm consists of the following steps:

1. Extraction of the high-susceptibility structures from the initial susceptibility maps. This can be done by setting threshold χ_{th} to the initial susceptibility map, $\Delta\chi_{initial}(\vec{r})$. A high value of χ_{th} is used at the beginning to extract structures with relatively high susceptibility values (such as veins in the brain). A denoising filter, e.g., median filter, is typically applied before extracting the high susceptibility structures through thresholding. For the extraction of the veins, a high-pass filter could be applied too.

This facilitates the suppression of any other bigger structures from being included in the veins masks. Then the veins can be extracted by thresholding the high-pass filtered susceptibility maps using χ_{th}. Morphological operations such as opening and closing were performed after the thresholding to remove the noisy pixels. In the end, a binary mask M_χ is created which equals one for the high susceptibility regions and zero everywhere else. This mask is applied to the original susceptibility map $\Delta\chi_i(\vec{r})$ to get the extracted susceptibility map $\Delta\chi_i'(\vec{r})$. In order to reduce the streaking artefacts inside the veins, an edge-preserving low-pass filter will be applied, to only the pixels inside the veins. $\Delta\chi_i'(\vec{r})$ is Fourier transformed to get $\Delta\chi_i'(\vec{k})$.

2. Merging the k-space data. The original k-space data ($\Delta\chi_i(\vec{k})$) in the cone of singularities (i.e. $|G(\vec{k})| < th$) is merged with the k-space data $\Delta\chi_i'(\vec{k})$. Particularly, $\Delta\chi_i(\vec{k})$ and $\Delta\chi_i'(\vec{k})$ are merged to get new k-space data $\Delta\chi_{i,new}(\vec{k})$ as:

$$\Delta\chi_{i,new}(\vec{k}) = \begin{cases} \Delta\chi_i(\vec{k}), & for\ |G(\vec{k})| > th \\ \Delta\chi_i'(\vec{k}), & for\ |G(\vec{k})| \leq th \end{cases} \quad [5.10],$$

3. Steps 1 and 2 will be repeated until the relative change of the susceptibility value of the extracted structures is less than a pre-defined threshold σ. σ was chosen to be 0.01 in this study.
4. Once converged, the threshold χ_{th} will be lowered to include structures with lower susceptibility values (but still significantly higher than the background), such as the basal ganglia structures. Then Step 1 to 3 will be repeated.

The whole process is illustrated in **Fig. 5.5**.

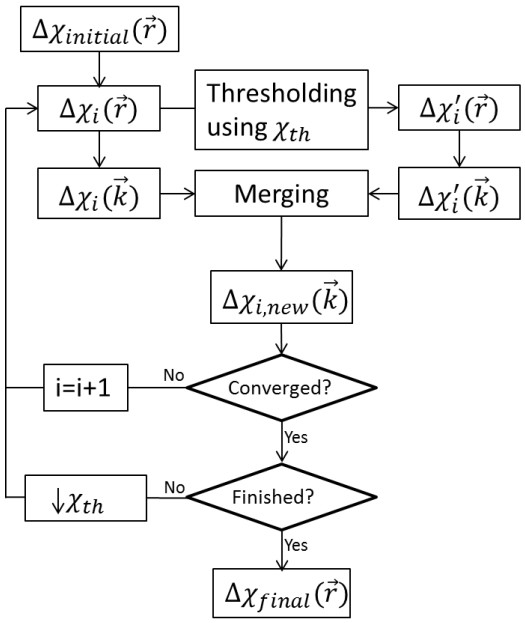

Figure 5.5 Illustration of the processing steps of Iterative SWIM algorithm.

5.2.2 Simulations

This algorithm was first evaluated using the 3D brain model. The phase images of this model were created using the forward calculation at B_0=3T and TE=10ms, without any background field. Uniform magnitude images were used in this simulation. White Gaussian noise was added to real and imaginary channels of the data and SNR in the final magnitude images is 20:1. The exact geometries of the veins and other grey matter structures were used in the iterative algorithm, in order to evaluate the errors purely caused by the updating of k-space data. First, only the geometries of the veins were input to the iterative SWIM algorithm. This corresponds to when a high χ_{th} is used to extract the veins. Next, the geometries of veins and other grey matter structures were input to the algorithm. This corresponds to when a relatively low χ_{th} is used. The mean and standard deviations of the susceptibility values of the veins, as well as other grey matter structures

(globus pallidus, putamen, caudate nucleus and red nucleus) were measured for each iteration step. To study the effects of the k-space truncation threshold, different values of *th* were tested, with *th* ranging from 0 to 0.2, with step size 0.01.

5.2.3 *In vivo* data studies

The iterative SWIM algorithm was also tested using *in vivo* data collected on a 3T scanner with TE=14.3ms, voxel size 0.5×0.5×0.5mm^3. For this *in vivo* data, the veins were extracted with χ_{th}=0.16 ppm. The grey matter structures were extracted using χ_{th}=0.06 ppm. The accuracy of using these parameters for extracting the geometries was evaluated using the 3D brain model. Means and standard deviations of the susceptibilities were measured for veins and grey matter structures including globus pallidus, caudate nucleus, putamen, red nucleus and substantia nigra. For the veins, the vein masks extracted in the iterative SWIM algorithm were used for measuring susceptibility, while for the grey matter structures, manually drawn ROIs were used. The susceptibility maps generated using the iterative SWIM algorithm were also compared with those generated using Morphology Enabled Dipole Inversion (MEDI) (7). In MEDI, It is assumed that the low gradient regions found in magnitude images correspond to the low gradient regions in susceptibility maps. The nonlinear formulation of MEDI (11) was used, together with model error reduction through iterative tuning (MERIT). To suppress the gradients induced by noise in magnitude images, the magnitude images were processed using anisotropic diffusion filtering (12) with 2 iterations, step size 0.05, gradient threshold 100. The gradient masks were generated assuming that 30% of the pixels correspond to actual

gradients, according to (7). The results of MEDI are largely dependent on the regularization parameter λ. Note that, the definition of λ in the MEDI algorithm is slightly different than the "λ" shown in Eq. 5.8. In MEDI, λ is placed together with the data fidelity term, instead of the regularization term (7,11). Thus, a low λ in MEDI leads to over-regularized results, and a large λ leads to under-regularized results. In this study, we tested different values of λ in MEDI, with $\log_{10}$ λ ranging from 1 to 3, with step size 0.25. The optimal λ was chosen according to the discrepancy principle (13) to match the residual with the expected noise power, as was used in the previous studies (7,11) on MEDI.

5.2.4 Simulated Data Results

First of all, the effect of the parameter *th* is shown in **Fig. 5.6**, in which the relative errors in the susceptibility values (measured from the converged susceptibility maps) are plotted for different structures. As *th* increases, the relative error in the measured susceptibility values increases while the standard deviation decreases. In order to reduce the relative errors and to have low uncertainties in the estimated susceptibility values, in this study we chose *th* as 0.1.

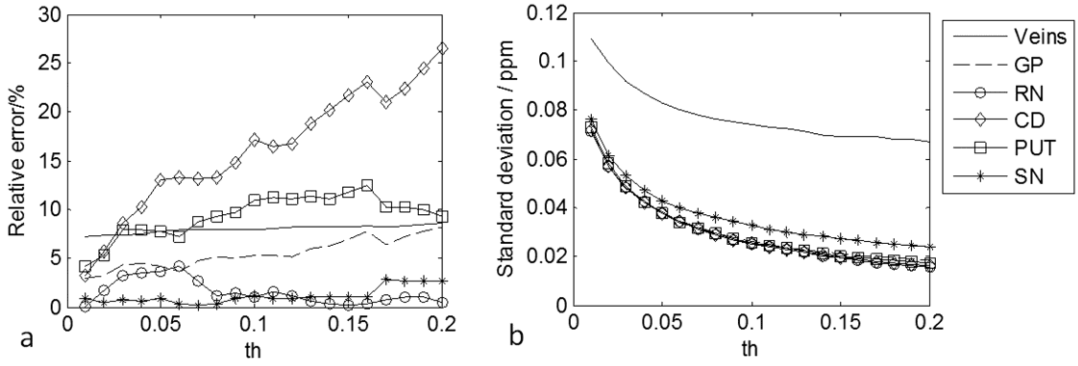

Figure 5.6 The effects of the parameter *th* on the accuracies of the estimated susceptibilities of different structures. **a**) The relative errors (absolute values) in the measured mean susceptibilities at different values of *th*. **b**) The standard deviations of the measured susceptibilities at different values of *th*.

Next, the mean and standard deviations of the susceptibilities of different structures at different iteration steps were plotted in **Fig. 5.7**. When only the geometries of the veins were used as constraints, the relative error in the mean susceptibility value of the veins quickly decreases and converges after the 3rd iteration, while the relative errors for all the other structures were increasing, as shown in **Fig. 5.7.a**. When the geometries of all the structures, including the veins, were used in the iterative SWIM algorithm, reduced relative errors in the measured susceptibility values were observed for all the structures, as indicated in **Fig. 5.7.b**. For the veins, the relative error was maintained at the same level as in **Fig. 5.7.a**. The standard deviations were reducing as more iteration steps were conducted, as can be seen from **Figure 5.7.c** to **5.7.f**.

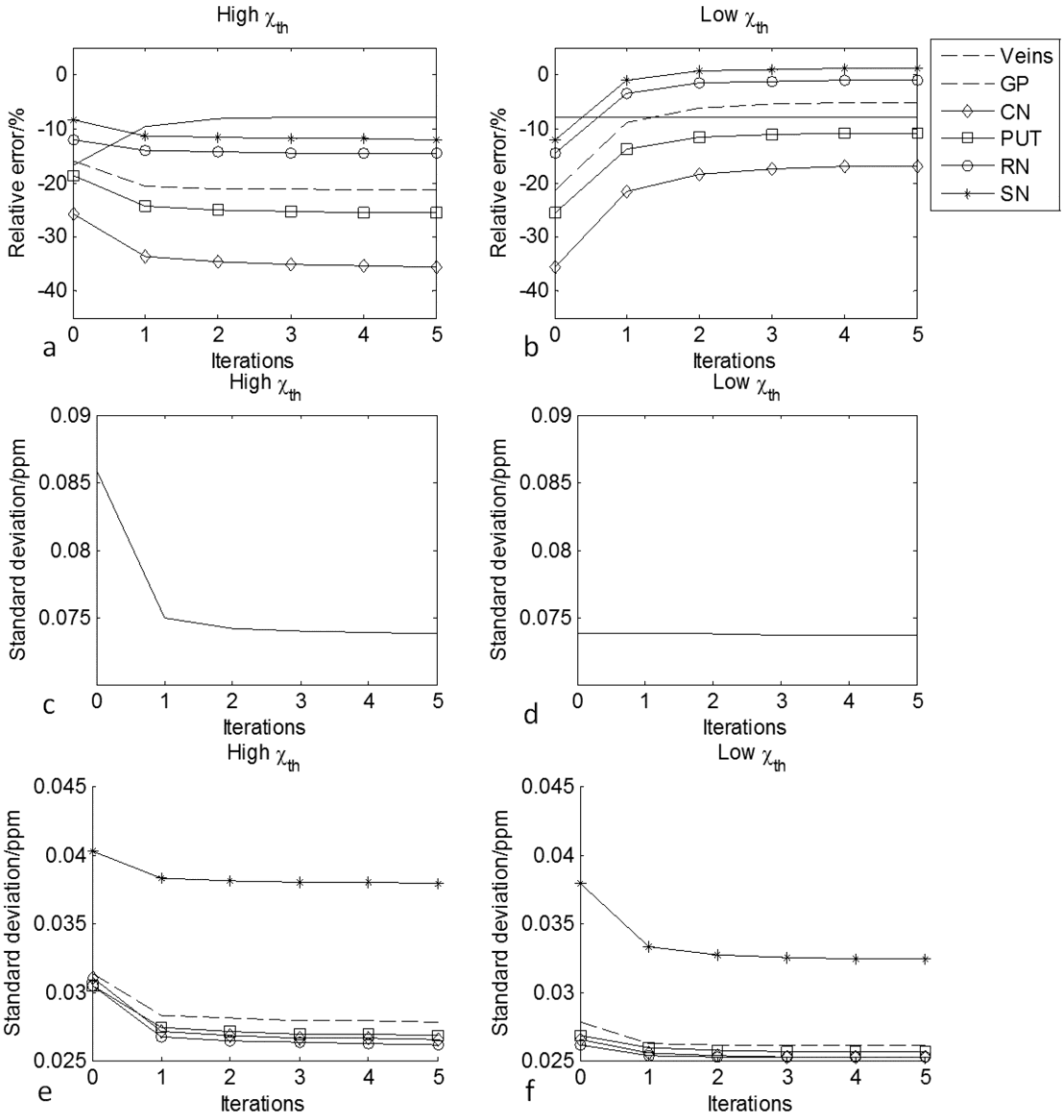

Figure 5.7 Means and standard deviations of the susceptibility values of different structures in the 3D brain model at different iteration steps. **a** and **b:** the mean susceptibility values measured at different iteration steps. **c** to **f**: the standard deviations measured at different iteration steps. The images in the first column (**a**, **c** and **e**) show the changes in mean and standard deviation when a high χ_{th} was used in geometry extraction, while the images in the second column show the results when a low χ_{th} was used in geometry extraction.

The iterative SWIM algorithm has reduced the streaking artefacts effectively, as can be seen from **Fig. 5.8**. Nonetheless, this iterative algorithm is optimized for the veins and the selected grey matter structures only. For the other parts of the brain, the relative errors in the measured mean susceptibility values were slightly increased after the iterative SWIM algorithm, as indicated by the error maps shown in **Fig. 5.8.c** and **5.8.d**.

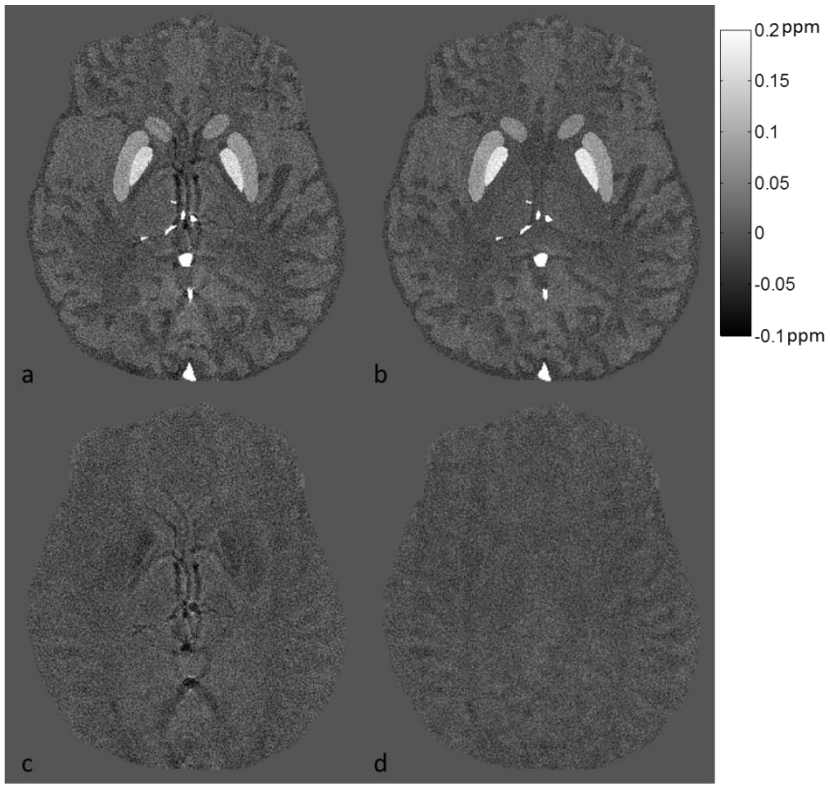

Figure 5.8 a) The initial susceptibility map. **b**) The final susceptibility map after iterative SWIM. **c**) The difference between **a** and the ideal susceptibility map. **d**) The difference between **b** and the ideal susceptibility map.

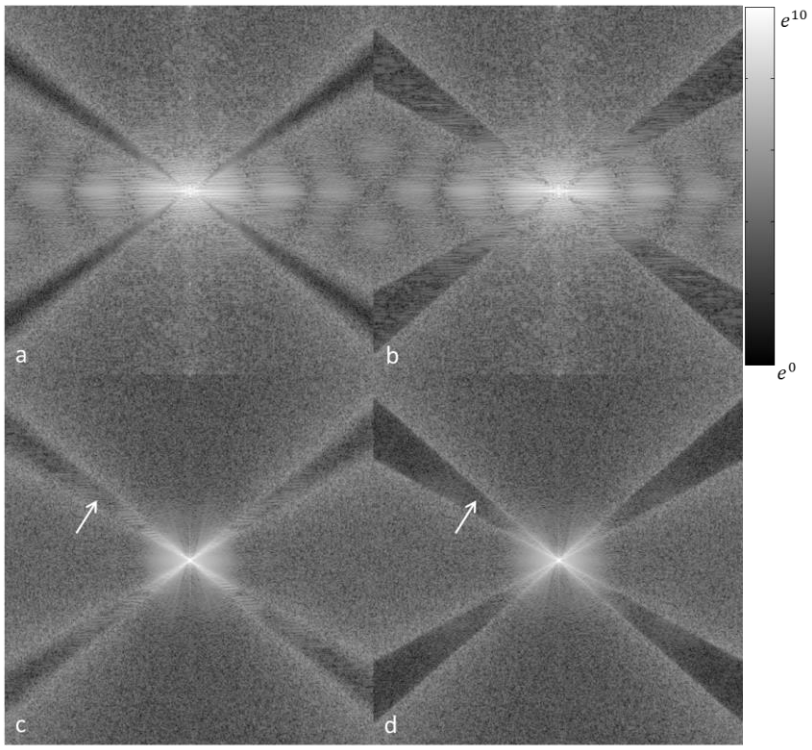

Figure 5.9 K-space profiles of the initial susceptibility map (**a**) and the final susceptibility map after iterative SWIM algorithm (**b**). The errors in the k-space profiles in **a** and **b** are shown in **c** and **d**, respectively. Specifically, the errors were calculated by comparing the k-space of the generated susceptibility maps with the kspace of the ideal susceptibility maps. Compared with the initial susceptibility maps, the final susceptibility maps after iterative SWIM algorithm have reduced errors in the cone of singularities in k-space, as indicated by the white arrows.

The k-space profiles of the original susceptibility map and the final susceptibility map after iterative SWIM algorithm are shown in **Fig. 5.9**. The errors of k-space data in the cone of singularity regions were reduced after the iterative SWIM algorithm, especially for the central part of the k-space, as indicated by the white arrows in **Fig. 5.9**.

5.2.5 *In vivo* Data Results

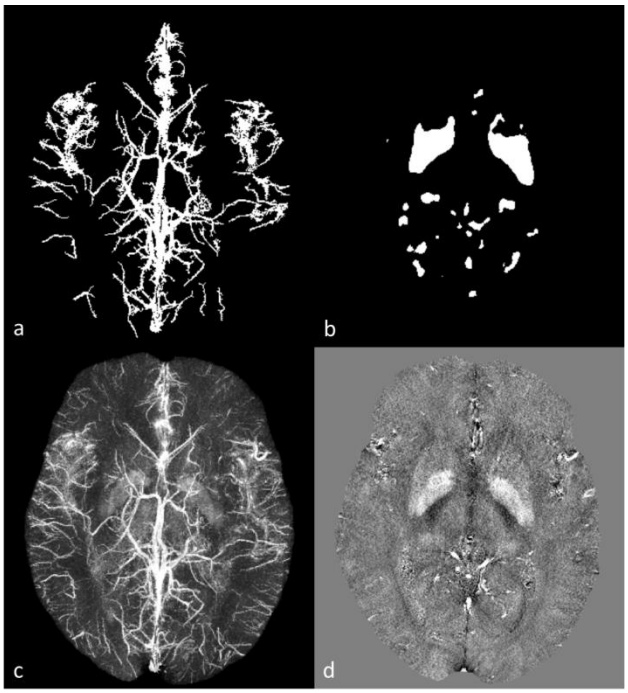

Figure 5.10 The extracted geometries of veins and grey matter structures (**a** and **b**) and the susceptibility maps (**c** and **d**) for the *in vivo* data. **a**) Maximum intensity projection of the binary masks of veins extracted using a high χ_{th}. **b**) One slice of the binary masks of the grey matter structures extracted using a low χ_{th}. **c**) Maximum intensity projection of the initial susceptibility maps. **d**) The corresponding susceptibility map to the binary mask shown in **b**.

The vein masks obtained from the *in vivo* data are shown in **Fig. 5.10**. Particularly, **Fig. 5.10.a** shows the maximum intensity projection (MIP) of the binary vein masks obtained from single high-pass filtering and thresholding, while **Fig. 5.10.b** shows the one slice of the binary masks for other grey matter structures with lower susceptibility values than the

veins. In order to evaluate the accuracy in the structure extraction, the vein masks and grey matter structure masks were generated for the brain model using the same algorithms and parameters. The relative error (calculated as *(number of missed pixels +number of false positives)* / *actual number pixels in veins*) in the extracted veins was measured as 9% and 10%, respectively. For the *in vivo* data, it was also observed that, the detected geometries of the veins or grey matter structures were sometimes locally contaminated by the noise and streaking artefacts which may have high intensities on the susceptibility maps. Besides, the putamen was only partly extracted, as shown in **Fig. 5.10.b**. This could be due to the variation of susceptibilities within the putamen.

Similar to what was seen in the simulation, in the first round of iterations, when the geometries of the veins were extracted using the high χ_{th}, the mean susceptibility values of veins quickly converge after the 3rd iteration step, as shown in **Fig. 5.11.a**. The susceptibility values of other structures were decreased after the iterative algorithm was applied, except for red nucleus, for which the susceptibility value was slightly increased, as indicated by the images in the first columns of **Figs. 5.11** and **5.12**. In the second round of iterations, when the geometries of both the grey matter structures and the veins were extracted using a low χ_{th}, the mean susceptibility values of all the grey matter structures were increased, while the susceptibility of the veins was maintained at the same level as in the first round of iterations, as can be seen from the second columns of **Figs. 5.11** and **5.12**. For the veins, the standard deviations in the measured susceptibilities were decreased as more iteration steps were conducted, as shown in **Fig. 5.13.a** and **5.13.b**. For other structures, the standard deviations measured in the second round of iterations were

slightly increased (**Fig**. **5.13.c** and **5.13.d**). This could be caused by the errors in the extracted geometries of these structures. The streaking artefacts were reduced dramatically for all the structures, as can be seen from **Fig. 5.14.**

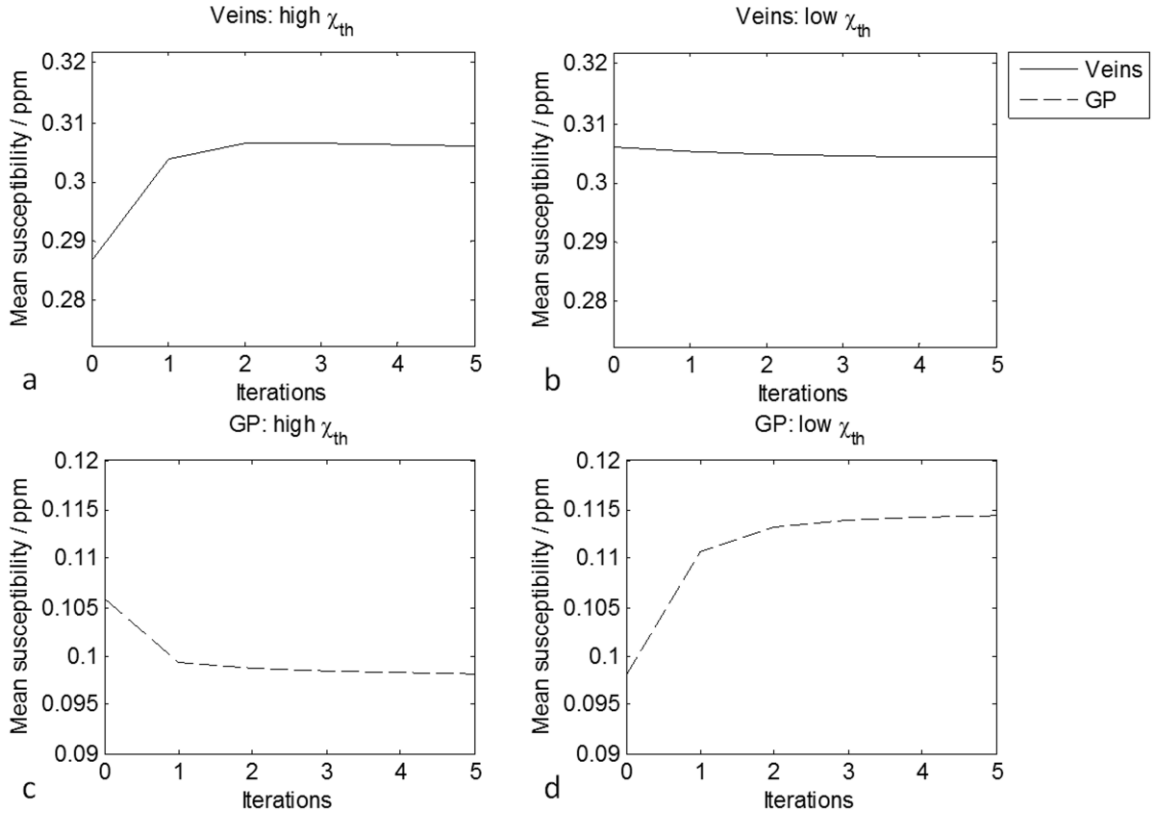

Figure 5.11 Mean susceptibility values of veins and globus pallidus at different iteration steps in the *in vivo* data. The figures in the first column were obtained when high χ_{th} was used to extract the geometries of veins only, while the figures in the second column were measured when low χ_{th} was used to extract the geometries of veins and other structures.

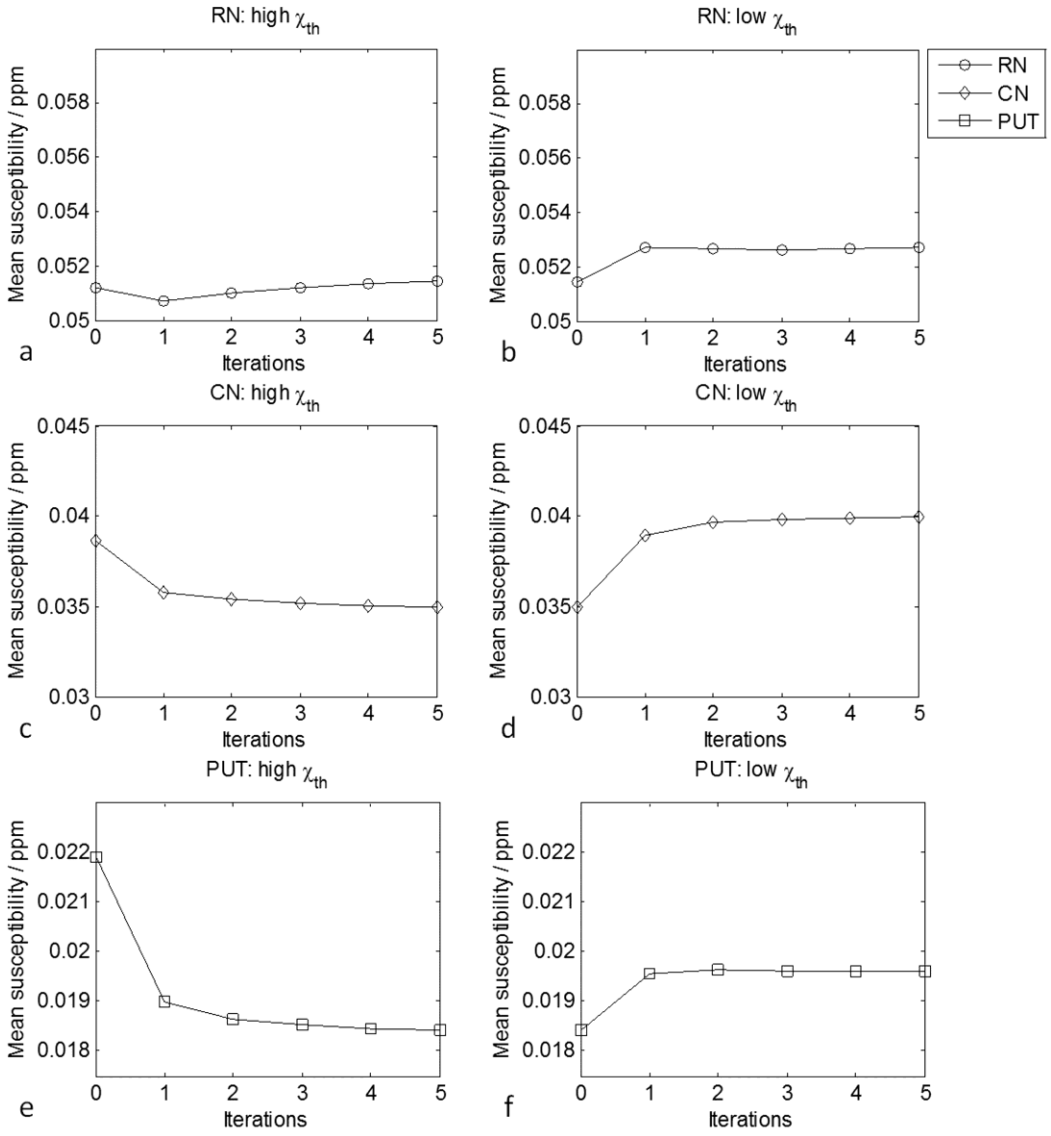

Figure 5.12 Mean susceptibility values of red nucleus (RN), caudate nucleus (CN) and putamen (PUT) at different iteration steps in the *in vivo* data. The figures in the first column were obtained when high χ_{th} was used to extract the geometries of veins only, while the figures in the second column were measured when low χ_{th} was used to extract the geometries of veins and other structures.

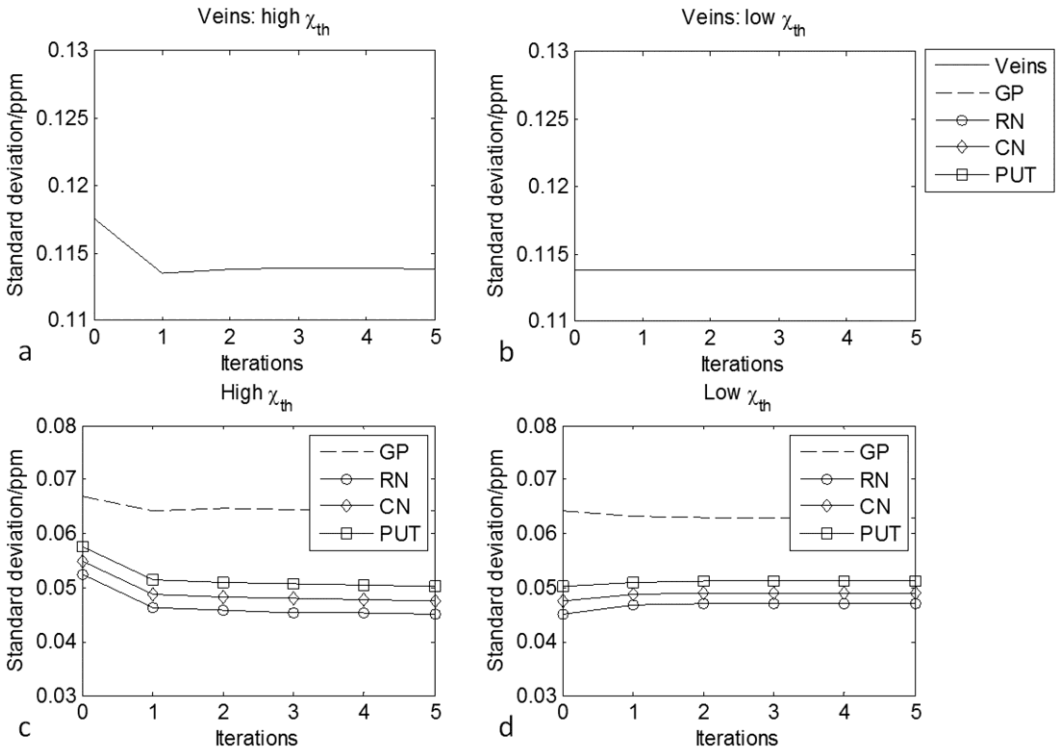

Figure 5.13 Standard deviations of the susceptibility values at different iteration steps for different structures in the *in vivo* data. The figures in the first column were obtained when high χ_{th} was used to extract the geometries of veins only, while the figures in the second column were measured when low χ_{th} was used to extract the geometries of veins and other structures.

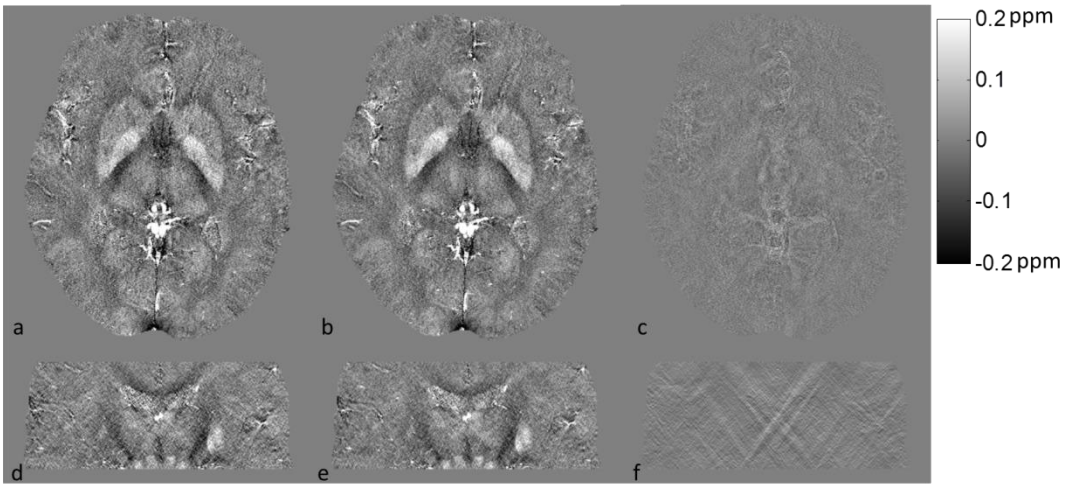

Figure 5.14 Comparison between the initial susceptibiltiy maps (**a** and **d**) and the final susceptibility maps (**b** and **e**). Their differences are shown in **c** and **f** (generated as **b**-**a** and **e**-**d**).

5.2.6 Comparison with Morphology Enabled Dipole Inversion (MEDI)

For MEDI, the proper value of λ was selected based on **Fig. 5.15.** The susceptibility maps generated with different values of λ are shown in **Fig. 5.16**. The smaller the λ, the more smoothed the susceptibility maps, and the smaller the RMSE. In this study, the optimal λ was chosen to be 100.

Compared with the susceptibility maps generated by iterative SWIM algorithm, MEDI leads to smoother images with preserved edge information in the predefined regions. However, since MEDI utilizes the edge information in magnitude images only, when there is no clear edge, MEDI may lead to underestimation of the susceptibilities of veins, as shown in **Fig. 5.17**. In the cortical region, these two methods yield similar results.

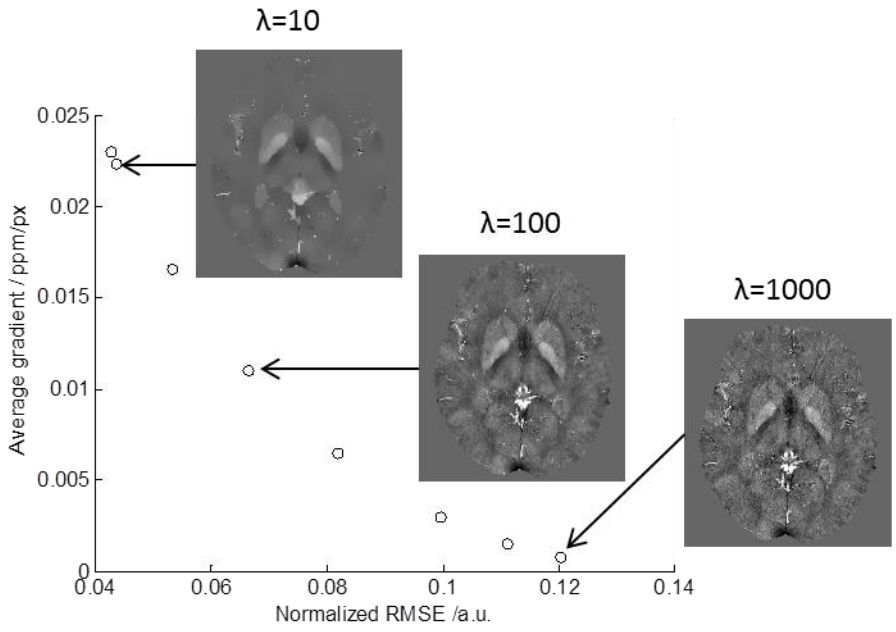

Figure 5.15 The effects of the regularization parameter λ in MEDI. The average gradient was measured in the low gradient regions in the converged susceptibility maps.

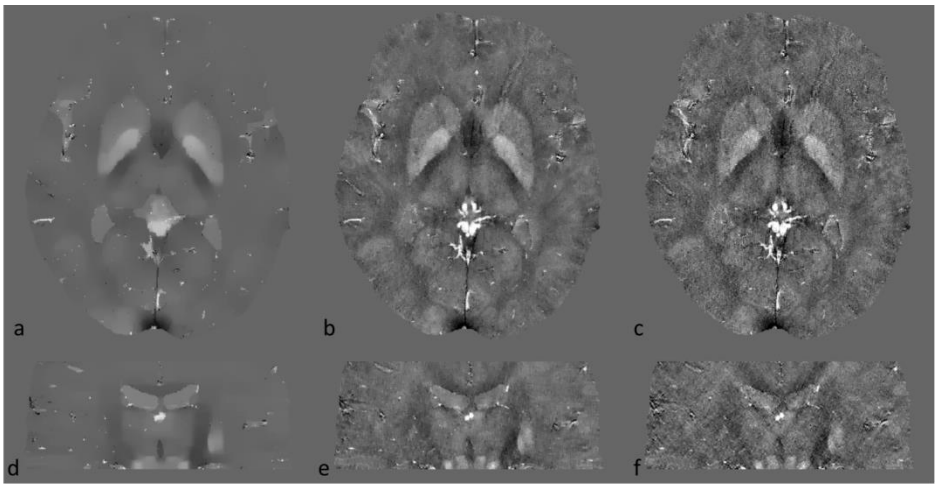

Figure 5.16 Susceptibility maps generated using different values of regularization parameter λ with MEDI. **a** and **d:** λ=10. **b** and **e:** λ=100. **a** and **d:** λ=1000.

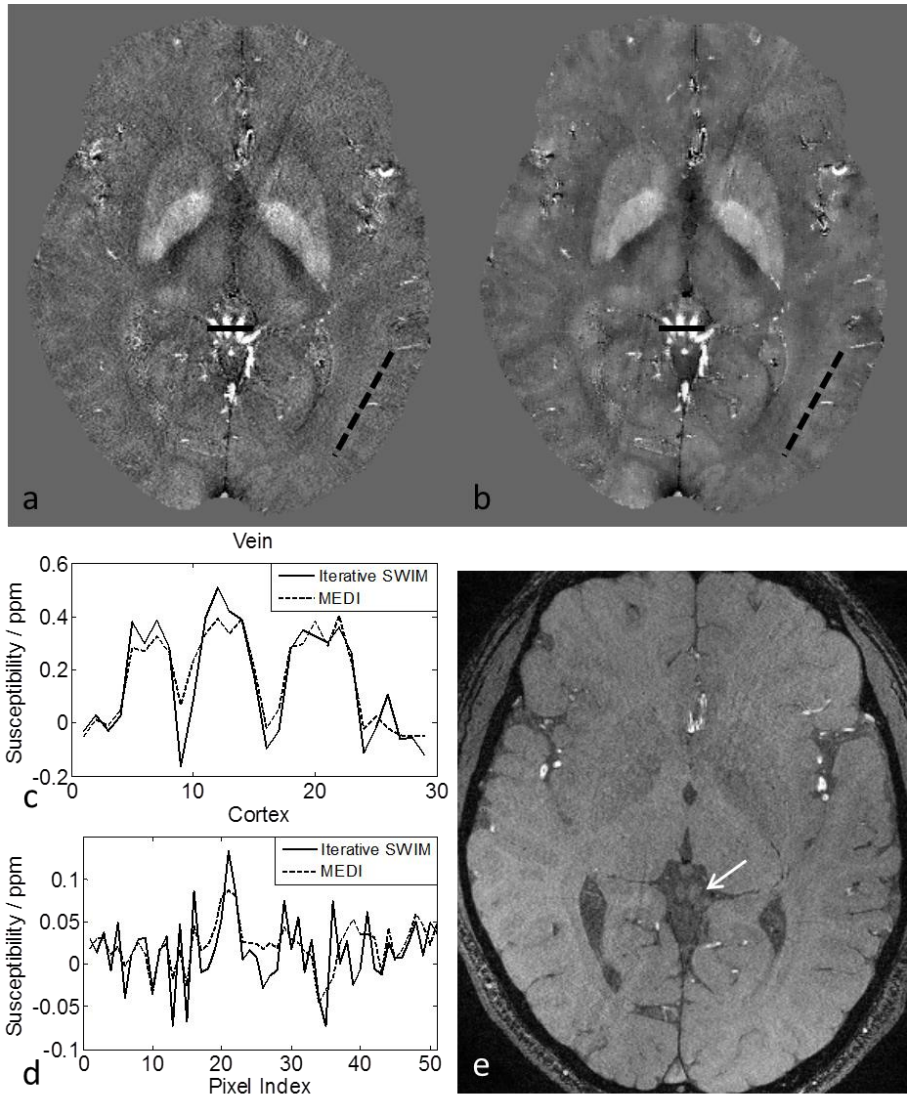

Figure 5.17 Comparison of susceptibility maps generated by iterative SWIM (**a**) and MEDI (**b**). The profiles of the solid black lines across the vein of Galen in **a** and **b** are shown in **c**. The profiles of the dashed black line in the cortical region were shown in **d**. The corresponding magnitude image is shown in **e**, which does not have clear edge information of the veins in the region indicated by the white arrow.

This is further confirmed by the histograms of the susceptibility values of the veins shown in **Fig. 5.18**. Compared with MEDI, iterative SWIM algorithm leads to higher susceptibility estimates of the veins. Meanwhile, the iterative SWIM provides almost the same susceptibility estimates for grey matter structures such as globus pallidus, as shown in **Table 5.1**. The distribution of the susceptibility values of the pixels inside the globus pallidus is narrower in MEDI than in iterative SWIM. This is due to the minimization of the edges inside globus pallidus in the susceptibility maps generated by MEDI.

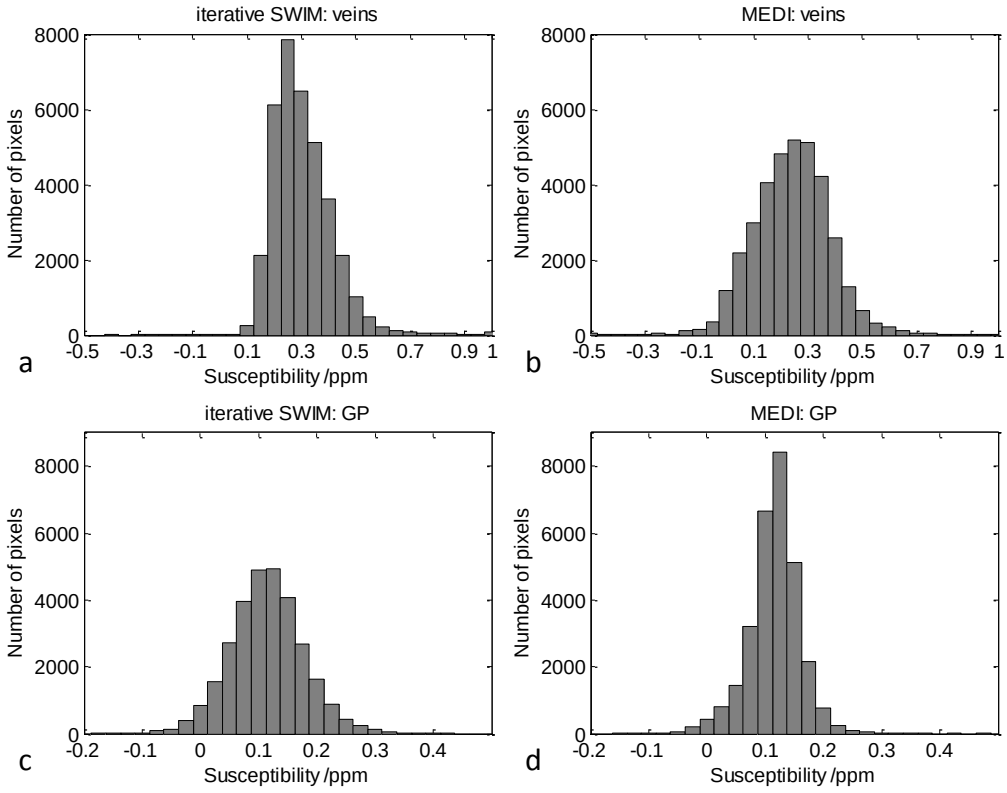

Figure 5.18 Distributions of the susceptibility values of the pixels inside the veins (**a** and **b**) and inside the globus pallidus (**c** and **d**), measured from iterative SWIM generated susceptibility maps (**a** and **c**) and from MEDI generated susceptibility maps (**b** and **d**).

Table 5.1 Mean and standard deviation (in ppm) measured from susceptibility maps generated using iterative SWIM algorithm and MEDI.

	Iterative SWIM	MEDI
Vein	0.30±0.11	0.24±0.15
Globus Pallidus	0.11±0.06	0.12±0.04
Red Nucleus	0.05±0.05	0.06±0.03
Caudate Nucleus	0.04±0.05	0.04±0.03
Putamen	0.02±0.05	0.03±0.04

The k-space profiles of the susceptibility maps are shown in **Fig. 5.19**. The major difference between the k-space obtained from MEDI and the k-space generated by iterative SWIM is associated with the singularity regions in k-space. For the k-space generated using iterative SWIM algorithm, the lower amplitude inside the singularity regions is due to the fact that only veins and certain grey matter structures with high susceptibility values were used to update the k-space. It can also be observed that outside the singularity regions, the amplitude of the k-space generated by iterative SWIM is slightly higher than that generated by MEDI, as indicated by the white arrow in **Fig. 5.19.d**. This is due to the difference between MEDI and iterative SWIM in defining the cone of singularities. In iterative SWIM, the cone of singularities is explicitly defined using the k-space truncation threshold, and only the k-space data inside this singularity region are updated.

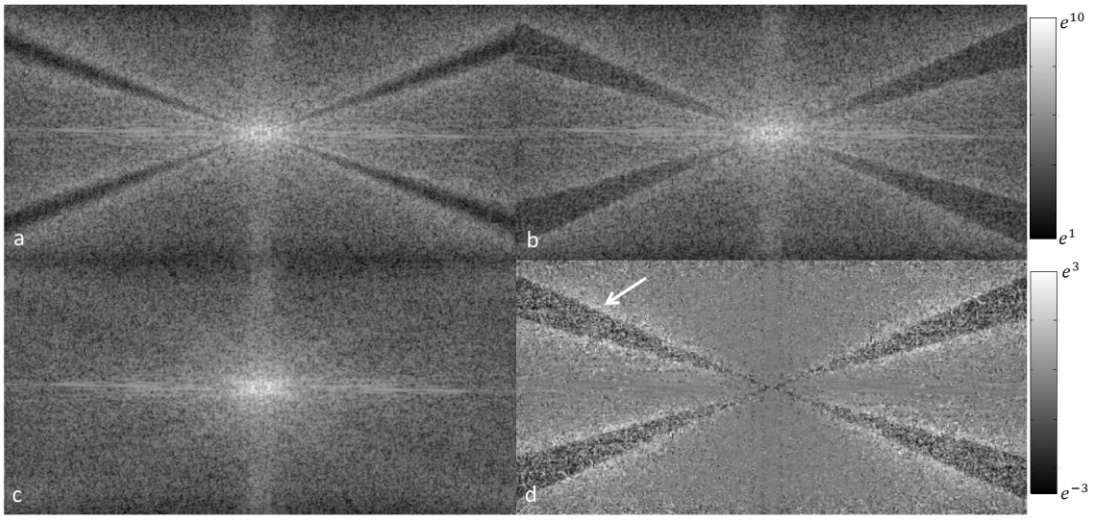

Figure 5.19 The k-space profiles obtained using truncated k-space division (**a**), iterative SWIM (**b**) and MEDI (**c**). The difference between **b** and **c** is shown in **d**. The window levels in **a**, **b**, and **c** are the same. The major differences are seen along the cone of singularities in k-space, as indicated by the white arrow.

5.3 Noise in susceptibility mapping

The noise in susceptibility mapping is dependent on several factors, such as the regularization in solving the inverse problem and the random noise in the original phase data. In order to study the propagation of the random noise in the original phase data to the noise in susceptibility maps, simulations were conducted using 2D cylinders with different radii ranging from 2 to 16 pixels. The phase images were created at B=3T, TE=5ms. The susceptibility value inside the cylinder was set to 1, outside 0. A constant value was assumed to create magnitude images. To simulate the partial volume effects, the magnitude and phase images were first created in a 4096×4096 matrix, then the central 256×256 of k-space were cropped to form the final magnitude and phase images.

Random noise was added to real and imaginary channels of the complex data, and the SNR in the magnitude images ranged from 2:1 to 20:1.

The susceptibility maps were generated using truncated k-space division, with k-space truncation threshold *th* ranging from 0.01 to 0.66, with step size 0.01. In order to study the propagation of random noise, independent of different regularization algorithms, the singularity regions where $|G(\vec{k})| < th$ were replaced using the k-space data of the ideal susceptibility maps. Means and standard deviations of susceptibility values were measured from both the regions inside the cylinders and a referenced region in the background. The mean susceptibility values were used to calculate the relative error in susceptibility estimation using different regularization thresholds with different levels of noise, while the standard deviations were used to estimate the noise in the susceptibility maps.

As shown in **Fig. 5.20.a** and **b**, the standard deviations measured in the reference region in the background are consistent for different cylinders. However, the standard deviations measured inside the cylinders show large variation. For large cylinders, the standard deviations measured in the two different regions are similar. Thus, the large difference between the standard deviations in **Fig. 5.20.a** and **b** for small cylinders is mainly due to the partial volume effects. When the standard deviations measured in the background reference region was used in analysis, the noise in susceptibility maps is found to be dependent on the noise in the original phase images. This relation can be approximated as a linear function as:

$$\sigma_\chi = \frac{\alpha\sigma_\phi}{\gamma B_0 TE} = \frac{\alpha}{\gamma B_0 TE \cdot SNR_{mag}} \quad [5.11],$$

where α represents the noise amplification factor. As shown in **Fig. 5.20.c**, when the regularization threshold *th* was chosen to be 0.1, α is approximately 4. This is consistent with the amplification factor found in the previous study (14). Note that α gets smaller as the regularization threshold *th* increases, although the relative error will also increase as *th* increases, as discussed in earlier sections. When α was plotted as a function of the relative error in the estimated susceptibilities, there appears to be an optimal regularization threshold *th*=0.13 which leads to both low noise amplification and low relative error in the susceptibility estimation. This is consistent with the optimal regularization threshold found earlier in this chapter.

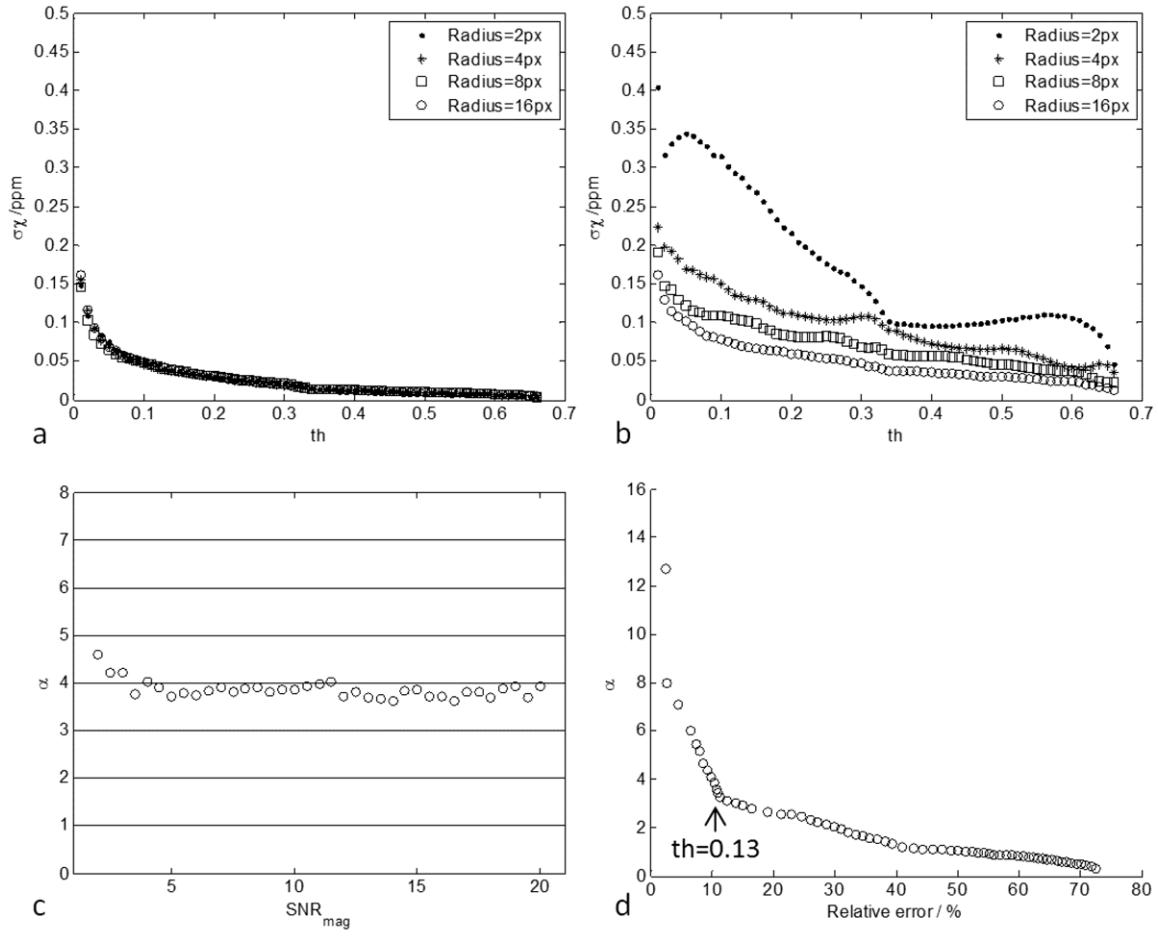

Figure 5.20 **a**) Standard deviation of susceptibilities measured in the background reference region for cylinders with different radii. **b**) Standard deviation measured inside the cylinders. **c**) Noise amplification factor α as a function of SNR in magnitude images, when th=0.1. **d**) Noise amplification factor α as a function of relative errors in the estimated susceptibilities, when SNR=10:1. The arrow shows the case when *th*=0.13, α=3.3 and the underestimation of the susceptibility is 11.3%.

5.4 Discussion and Conclusions

The main obstacle of quantitative susceptibility mapping originates from the ill-posed inverse problem. This leads to mainly three problems: underestimation of the susceptibility, streaking artefacts, and amplification of the noise.

The underestimation of susceptibility can be well-approximated for structures with relatively large susceptibility values, such as veins. But for other structures, such as the grey matter structures, the estimation of susceptibilities is affected by the streaking artefacts caused by the nearby strong susceptibility structures. In this case, using a scaling factor to reduce the underestimation may lead to large uncertainties. Furthermore, it was noticed that when a large k-space truncation threshold was used, there tends to be more blurring of the susceptibility maps (4,5).

Another problem of current susceptibility mapping technique is related to the streaking artefacts. The inverse problem can be efficiently solved in Fourier domain through truncated k-space division, and the streaking artefacts are related to the regularization that is applied in the k-space division. Newer techniques aim to map the susceptibilities as an optimization problem, and impose different constraints to the inverse problem. The accuracies of these newer methods are largely dependent on the constraints that are used in the optimization. It has already been shown that purely the gradient information extracted from magnitude images may not be sufficient, as not all the edges in susceptibility maps correspond to detectable edges in the magnitude images (8). This is partly solved by integrating the gradient information found in both magnitude and phase

images (8). Essentially, all of these methods fall into the category of edge preserving smoothing. Even though the susceptibility maps generated by these algorithms are smooth, the computation time can be prohibitively long. The k-space/image domain iterative SWIM algorithm, on the other hand, is much faster and more suitable for clinical settings. For the *in vivo* data in this study, which has 512x512x256 matrix size, it took MEDI 1.9 hours to converge, but merely 1.6 minutes for iterative SWIM algorithm, on the same desktop with Intel i7 CPU.

The effectiveness of the iterative SWIM algorithm was also examined using simulated data and *in vivo* data. The iterative SWIM algorithm has replaced the original k-space data in the cone of singularities, using the k-space of high-susceptibility structures. This results in proper interpolation of the missing data in central part of the k-space, and suppression of the noise with high frequency due to the replacing of missing data in the periphery of k-space. The iterative SWIM algorithm preserves the susceptibility information of the veins, but may potentially under-estimate the susceptibility of bigger grey matter structures, if they are not included in the geometry masks. Nonetheless, the streaking artefacts surrounding the veins were largely reduced together with improved accuracy of estimating the susceptibility of the veins. This is particularly advantageous for studies related to measuring venous oxygen saturation.

Finally, the propagation of the random noise from original phase images to susceptibility maps was studied. With typical truncation threshold of 0.1, the noise amplification factor is close to four. This amplification factor was obtained assuming that only the cone of singularities in k-space was updated or modified. There are also studies on the noise

behavior in susceptibility mapping, using algorithms that update all the k-space values (15). Due to the smoothing function used in these algorithms, it is expected that the noise will be reduced in susceptibility maps.

The accuracy of susceptibility mapping is also affected by many other factors, particularly, partial volume effects. While this is less a problem for relatively big structures such as the globus pallidus, with the resolution used clinically (e.g., 1mm x 1mm x 2mm), it may cause errors for the veins. Considering a vein with diameter close to the imaging resolution, it may be still feasible to obtain a susceptibility value for the pixel which contains the vein. However, due to partial volume effects, it is not possible to obtain an accurate susceptibility value for the vein itself, but only an estimate of the magnetic moment, unless certain a priori information about the size of the vein is available (16,17).

In conclusion, the core of quantitative susceptibility mapping is solving the inverse problem. Various algorithms have been proposed to deal with the ill-posedness of this inverse problem. The k-space/image domain iterative algorithm is particularly time-efficient and applicable, especially for studies focused on measuring venous oxygen saturation.

References

1. Salomir R, de Senneville BD, Moonen CT. A fast calculation method for magnetic field inhomogeneity due to an arbitrary distribution of bulk susceptibility. Concepts Magn. Reson. Part B Magn. Reson. Eng. 2003;19B:26–34.
2. Marques J p., Bowtell R. Application of a Fourier-based method for rapid calculation of field inhomogeneity due to spatial variation of magnetic susceptibility. Concepts Magn. Reson. Part B Magn. Reson. Eng. 2005;25B:65–78.
3. Cheng Y-CN, Neelavalli J, Haacke EM. Limitations of calculating field distributions and magnetic susceptibilities in MRI using a Fourier based method. Phys. Med. Biol. 2009;54:1169–89.
4. Haacke EM, Tang J, Neelavalli J, Cheng YC. Susceptibility mapping as a means to visualize veins and quantify oxygen saturation. J. Magn. Reson. Imaging 2010;32:663–76.
5. Shmueli K, de Zwart JA, van Gelderen P, Li T, Dodd SJ, Duyn JH. Magnetic susceptibility mapping of brain tissue in vivo using MRI phase data. Magn. Reson. Med. 2009;62:1510–22.
6. Schweser F, Deistung A, Sommer K, Reichenbach JR. Toward online reconstruction of quantitative susceptibility maps: superfast dipole inversion. Magn. Reson. Med. 2013;69:1582–94.
7. Liu J, Liu T, de Rochefort L, Ledoux J, Khalidov I, Chen W, et al. Morphology enabled dipole inversion for quantitative susceptibility mapping using structural consistency between the magnitude image and the susceptibility map. NeuroImage 2012;59:2560–8.
8. Schweser F, Sommer K, Deistung A, Reichenbach JR. Quantitative susceptibility mapping for investigating subtle susceptibility variations in the human brain. NeuroImage 2012;62:2083–100.
9. Bilgic B, Pfefferbaum A, Rohlfing T, Sullivan EV, Adalsteinsson E. MRI estimates of brain iron concentration in normal aging using quantitative susceptibility mapping. NeuroImage 2012;59:2625–35.
10. Paige CC, Saunders MA. LSQR: An Algorithm for Sparse Linear Equations and Sparse Least Squares. ACM Trans Math Softw 1982;8:43–71.
11. Liu T, Wisnieff C, Lou M, Chen W, Spincemaille P, Wang Y. Nonlinear formulation of the magnetic field to source relationship for robust quantitative susceptibility mapping. Magn. Reson. Med. 2013;69:467–76.
12. Perona P, Malik J. Scale-space and edge detection using anisotropic diffusion. IEEE Trans. Pattern Anal. Mach. Intell. 1990;12:629–39.
13. Morozov, VA. On the solution of functional equations by the method of regularization. Sov. Math Dokl 1966;7:414–7.
14. Tang J, Liu S, Neelavalli J, Cheng YCN, Buch S, Haacke EM. Improving susceptibility mapping using a threshold-based K-space/image domain iterative reconstruction approach. Magn. Reson. Med. 2013;69:1396–407.

15. Liu T, Xu W, Spincemaille P, Avestimehr AS, Wang Y. Accuracy of the morphology enabled dipole inversion (MEDI) algorithm for quantitative susceptibility mapping in MRI. IEEE Trans. Med. Imaging 2012;31:816–24.
16. Cheng Y-C, Hsieh C-Y, Neelavalli J, Haacke EM. Quantifying effective magnetic moments of narrow cylindrical objects in MRI. Phys. Med. Biol. 2009;54:7025–44.
17. Liu S, Neelavalli J, Cheng Y-CN, Tang J, Mark Haacke E. Quantitative susceptibility mapping of small objects using volume constraints. Magn. Reson. Med. 2013;69:716–23.

Chapter 6 Improved Venography using True Susceptibility Weighted Imaging (tSWI)[2]

6.1 Introduction

Susceptibility weighted imaging (SWI) is a high resolution, spoiled gradient echo (GRE) magnetic resonance imaging (MRI) technique used today clinically for evaluating small veins and venous abnormalities in the brain and the presence of increased iron content and microbleeds in diseases such as dementia, multiple sclerosis (MS), Parkinson's disease, stroke and traumatic brain injury (TBI) (1–3). SWI's exquisite sensitivity to small tissue magnetic susceptibility changes is due to its use of phase information (3–5). Paramagnetic or diamagnetic substances relative to water such as blood products or calcium, respectively, perturb the local magnetic field proportional to their respective magnetic susceptibilities. These differences are reflected in the phase of the MR images.

[2]Most of the contents in this chapter are adapted from Liu S, Mok K, Neelavalli J, Cheng YCN, Tang J, Ye Y, Haacke EM. Improved MR Venography Using Quantitative Susceptibility-Weighted Imaging. J. Magn. Reson. Imaging 2013; Article first published online: 31 OCT 2013 DOI: 10.1002/jmri.24413. Reprint under license.

In conventional SWI, after applying appropriate unwrapping and/or filtering techniques on the raw phase data (1,3), a phase dependent mask is created and multiplied *n* times into the magnitude data to enhance the contrast/visibility of these substances.

Although SWI has been used quite successfully in clinical applications for many years, it is important to realize that it has a few weaknesses. One of them is based on the fact that the MRI phase signal is not only a function of the susceptibility, but also dependent on shape and orientation of the structure of interest. In data acquired with sufficient resolution, the phase inside veins perpendicular to the field has the opposite sign to that inside veins parallel to B_0. This leads to variable suppression effects with the phase mask that makes SWI unique over conventional gradient echo imaging (6). Recently, quantitative susceptibility mapping (QSM) has emerged as a means to extract the source of phase information, that is, the local susceptibility distribution (7–15). QSM is known to be independent of echo time and, to a large degree, of orientation. To avoid the vessel orientation dependence in routine SWI data, instead of phase, we propose using a mask based on the susceptibility map. We refer to this approach as true-SWI (tSWI) to distinguish it from the conventional phase mask based SWI. In this work, our purpose is to compare the ability of these two methods to improve venous contrast and to show that tSWI is able to remove the geometry dependence of the phase for veins and microbleeds in SWI data.

6.2 Materials and Methods

To provide some flexibility in generating the susceptibility weighting mask *W*, we introduce both lower and upper thresholds for defining the mask as follows:

$$W = \begin{cases} 1 & for\ \chi \leq \chi_1 \\ 1 - \frac{\chi - \chi_1}{\chi_2 - \chi_1} & for\ \chi_1 < \chi \leq \chi_2 \\ 0 & for\ \chi > \chi_2 \end{cases} \quad [6.1],$$

where χ refers to the susceptibility value of a voxel (e.g., vein) relative to the surrounding tissue in the susceptibility map, χ_1 is the lower limit and χ_2 is the upper limit of the range of tissue susceptibility values for which we want to improve the contrast in the final susceptibility weighted image. Finally, the true-SWI is generated by multiplying the magnitude image with the mask *n* times similar to the usual SWI mask application:

$$tSWI = mag \cdot W^n \quad [6.2].$$

The whole process is illustrated in **Fig.6.1**.

In order to determine appropriate values for these two thresholds, we examined different potential choices. For χ_1, we used: 1) the mean susceptibility value in the background white matter tissue region (0 ppm) in the susceptibility map and 2) three standard deviations ($3\sigma_\chi$) above the tissue region, where σ_χ is the standard deviation of the white matter tissue region in the susceptibility map. While a threshold of 0 ppm would ensure that the susceptibility weighting mask would include smaller veins that are partial volumed, it can also lead to increased noise in tissue regions where susceptibility is supposed to be zero. On the other hand, a choice of $\chi_1 = 3\sigma_\chi$ would reduce inclusion of noise in the mask. For χ_2, we used: 1) the expected mean susceptibility value in the vein,

which is about 0.45 parts per million (ppm) relative to water (3,16) under normal physiological conditions; and 2) a value higher than this, in this case 1ppm.

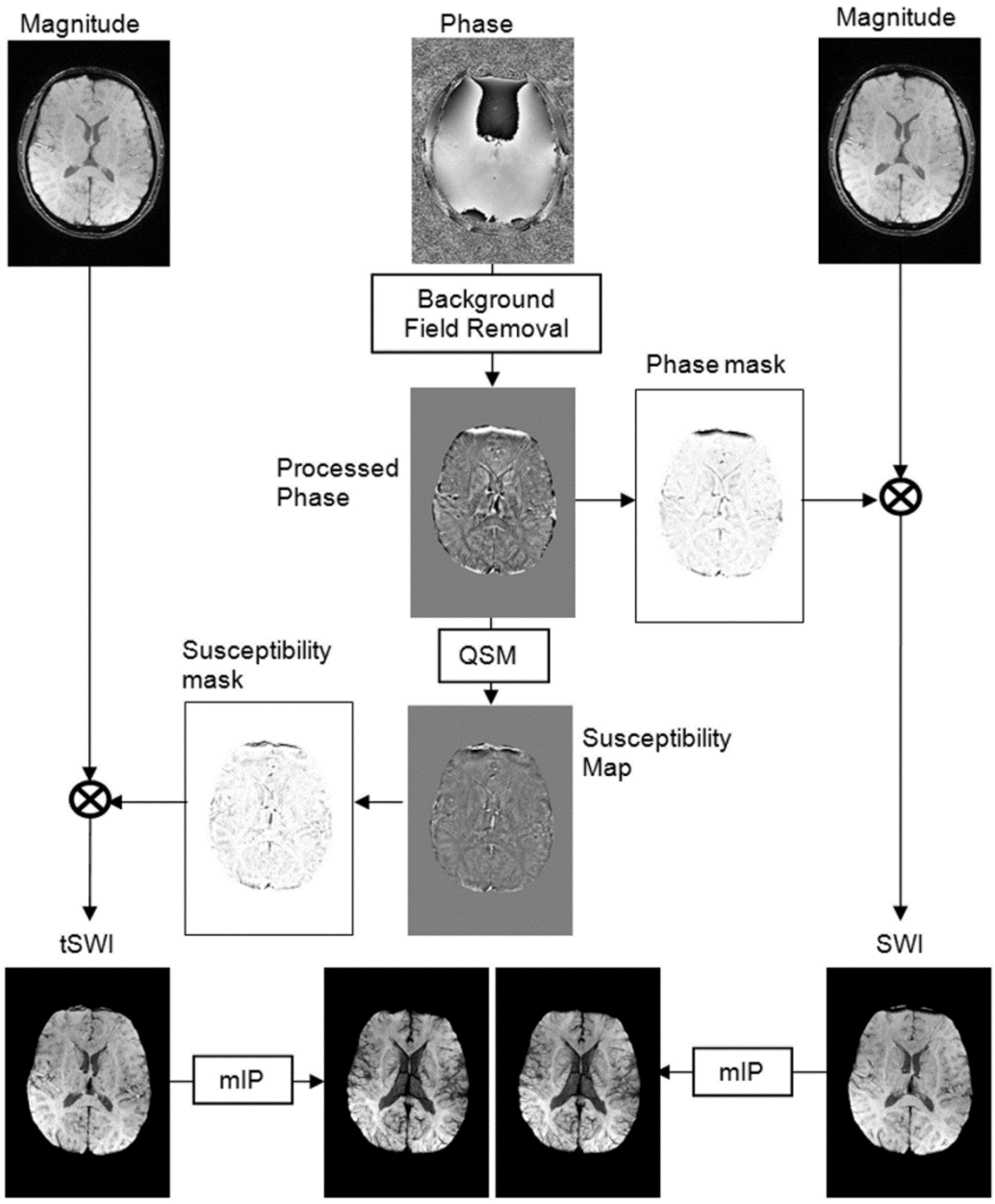

Figure 6.1 A comparison between tSWI and SWI data processing steps.

For a given set of χ_1 and χ_2 values, the contrast-to-noise ratio (CNR) between the vein and the background tissue can be optimized by choosing an appropriate *n* value in Eq. 6.2. CNR for a vein can be defined as the ratio between tSWI signal contrast for the vein and its associated uncertainty as follows:

$$CNR = \frac{|S_{ref,tSWI} - S_{vein,tSWI}|}{\sigma_t} \quad [6.3],$$

where $\sigma_t = \sqrt{\sigma_{ref,tSWI}^2 + \sigma_{vein,tSWI}^2}$. Noise in either the reference (background tissue) region ($\sigma_{ref,tSWI}$) or in the vein ($\sigma_{vein,tSWI}$) in the tSWI image can be estimated using the following equation:

$$\sigma_{tSWI} = \sqrt{W^{2n}\sigma_{mag}^2 + mag^2 n^2 W^{2n-2}\sigma_W^2} \quad [6.4].$$

The noise, represented by the standard deviation for a given voxel in *W*, σ_W, is dependent on the noise, σ_χ, in the susceptibility map in the following manner:

$$\sigma_W = \begin{cases} \frac{\sigma_\chi}{\chi_2 - \chi_1} & for\ \chi_1 < \chi < \chi_2 \\ 0 & for\ \chi < \chi_1 \text{ or } \chi > \chi_2 \\ \frac{\sigma_\chi}{2(\chi_2 - \chi_1)} & for\ \chi = \chi_1\ or\ \chi = \chi_2 \end{cases} \quad [6.5].$$

The factor 1/2 in the case when $\chi = \chi_1$ or $\chi = \chi_2$ in Eq. 6.5 is due to the discontinuity (1). For simplicity, we assume that signal from vein (or cylinder) and reference region in the original magnitude images are the same: $mag_{ref} = mag_{vein} = S$, and their associated signal standard deviations in these two regions are also the same: $\sigma_{ref,mag} = \sigma_{vein,mag} = \sigma$. Furthermore, we assume that the mean susceptibility value of the reference region is 0, and the mean susceptibility value of the vein is χ_v.

i) When a threshold of $\chi_1 = 0$ was used to generate the susceptibility mask, in the reference region, $W = 1$, and $\sigma_W = \sigma_\chi/(2\chi_2)$. In the vein, $W = 1 - \chi_v/\chi_2, \sigma_W = \sigma_\chi/\chi_2$, for $\chi_1 < \chi_v < \chi_2$; but when $\chi_v = \chi_2$, $W = 0$, $\sigma_W = \sigma_\chi/(2\chi_2)$; when $\chi_v > \chi_2$, $W = 0$, $\sigma_W = 0$. Using Eq. 6.4,

$$\sigma_t = \begin{cases} \left(\sigma^2 + \frac{S^2 n^2 \sigma_\chi^2}{4\chi_2^2} + \sigma^2\left(1 - \frac{\chi_v}{\chi_2}\right)^{2n} + S^2 n^2 \left(1 - \frac{\chi_v}{\chi_2}\right)^{2n-2} \frac{\sigma_\chi^2}{\chi_2^2}\right)^{\frac{1}{2}}, & \text{for } \chi_1 < \chi_v < \chi_2 \\ \left(\sigma^2 + \frac{S^2\sigma_\chi^2}{4\chi_2^2} + \frac{S^2\sigma_\chi^2}{4\chi_2^2}\right)^{\frac{1}{2}} & \text{for } \chi_v = \chi_2, n = 1 \\ \left(\sigma^2 + \frac{S^2 n^2 \sigma_\chi^2}{4\chi_2^2}\right)^{\frac{1}{2}} & \text{for } \chi_v = \chi_2, n > 1; or\ \chi_v > \chi_2 \end{cases} \quad [6.6].$$

ii) When a threshold of $\chi_1 = 3\sigma_\chi$ was chosen, in the reference region, $W = 1$, and $\sigma_w = 0$ due to the fact that most pixels in the reference (background tissue) region have susceptibility values less than $3\sigma_\chi$. In the vein, $W = 1 - (\chi_v - 3\sigma_\chi)/(\chi_2 - 3\sigma_\chi), \sigma_w = \sigma_\chi/(\chi_2 - 3\sigma_\chi)$, for $\chi_1 < \chi_v < \chi_2$; but when $\chi_v = \chi_2$, $W = 0$, $\sigma_w = \sigma_\chi/2(\chi_2 - 3\sigma_\chi)$; when $\chi_v > \chi_2$, $W = 0$, $\sigma_w = 0$. Thus,

$$\sigma_t = \begin{cases} \left(\sigma^2 + \sigma^2\left(1 - \frac{\chi_v - 3\sigma_\chi}{\chi_2 - 3\sigma_\chi}\right)^{2n} + S^2 n^2 \left(1 - \frac{\chi_v - 3\sigma_\chi}{\chi_2 - 3\sigma_\chi}\right)^{2n-2} \frac{\sigma_\chi^2}{(\chi_2 - 3\sigma_\chi)^2}\right)^{\frac{1}{2}}, & \text{for } \chi_1 < \chi_v < \chi_2 \\ \left(\sigma^2 + S^2 n^2 \frac{\sigma_\chi^2}{4(\chi_2 - 3\sigma_\chi)^2}\right)^{\frac{1}{2}}, & \text{for } \chi_v = \chi_2, n = 1 \\ \sigma, & \text{for } \chi_v = \chi_2, n > 1;\ or\ \chi_v > \chi_2 \end{cases}$$

[6.7].

Thus the CNR can be written as:

$$CNR = S(1 - \left(1 - \frac{\chi_v - \chi_1}{\chi_2 - \chi_1}\right)^n)/\sigma_t \quad [6.8],$$

for $\chi_1 < \chi_v \leq \chi_2$, with σ_t given in Eqs. 6.6 and 6.7.

When $\chi_1 = 3\sigma_\chi$ and χ_v is slightly less than χ_2, CNR approaches SNR in the magnitude images as *n* approaches infinity. In this case, the optimal *n* was chosen to be the value where CNR reaches 90% of the maximal CNR for a certain vein.

Simulations

To evaluate the theoretical predictions, the optimal choice of *n* for generating tSWI images for different threshold values and vessel susceptibility values, and the influence of high-pass filtering on the final CNR for veins in tSWI images, simulations were performed using cylinders as surrogates to veins. A series of cylinders with radii ranging from 2 pixels to 16 pixels was used to simulate the associated phase images in a 512×512 matrix at B_0=3T, and TE=10ms. The cylinders were taken to be perpendicular to the main magnetic field. The input susceptibility of the cylinders was set to be 0.45ppm and the susceptibility value of the background region was set to zero. In order to simulate a more realistic response of the field perturbation, the complex data of a cylinder with radius 16 times of the final radius was first created on an 8192×8192 matrix. The magnitude signal for the cylinder and background region were taken to be unity. The central 512×512 k-space points generated from the larger matrix were then used to reconstruct the complex images of the cylinders. Gaussian noise was added to both real and imaginary channels of the data to simulate the SNR in the magnitude images to be 10:1. The simulated phase images were processed using a homodyne high-pass filter with a k-space window size of

64×64. Two sets of susceptibility maps, one from unfiltered and the other from filtered phase images, were generated for each cylinder size, using truncated k-space division with a k-space threshold of 0.1 (7). This is to evaluate the influence of high-pass filtering on the final CNR in tSWI images. The tSWI images were generated using Eqs. 6.1 and 6.2 for different values of χ_1 and χ_2 as mentioned in the previous section. The standard deviation of the susceptibility maps was measured from a reference region outside the cylinder. The susceptibility mask was multiplied into the magnitude image *n* times with *n* ranging from 0 to 10 (*n*=0 refers to the case of no mask multiplication). The local CNRs between cylinders and the background reference were measured from the tSWI data using:

$$CNR_{measured} = |S_{vein} - S_{ref}| \,/\sigma_t \qquad [6.9]$$

where S_{vein} and S_{ref} are the mean intensity values inside the cylinder (vein) and inside a reference region of interest (ROI) adjacent to the cylinder directly from tSWI image, respectively. In order to estimate the overall noise σ_t directly from tSWI images, the standard deviations inside the cylinder ($\sigma_{vein,tSWI}$) and the reference region ($\sigma_{ref,tSWI}$) in tSWI were measured and σ_t was again calculated as the square root of $\sigma^2_{vein,tSWI} + \sigma^2_{ref,tSWI}$. The theoretically predicted CNRs from Eq. 6.8 using different thresholds for generating the susceptibility mask were compared with those measured from the simulations and the appropriate value for χ_2 for processing *in vivo* data was determined. CNRs of the cylinders with different susceptibility values ranging from 0.2ppm to 0.45ppm were calculated to evaluate the influence of the susceptibility value of the object on the optimal choice of *n*.

In vivo data

Table 6.1 Imaging parameters for three volunteers and one patient for *in vivo* studies. Dataset 5 was collected on a TBI patient.

Dataset No.	1	2	3	4	5
Volunteer No.	1	1	2	3	-
B_0 (T)	3	3	3	3	3
TR (ms)	26	26	24	24	29
TE (ms)	14.3	17.3	17	15.3	20
FA (degrees)	15	15	15	12	15
BW (Hz/px)	121	121	181	121	120
Voxel size (mm^3)	0.5×0.5 ×0.5	0.5×0.5 ×0.5	0.5×0.5 ×0.5	0.5×0.5 ×0.5	0.5×0.5 ×2
Matrix Size	512×368 ×256	512×368 ×256	512×368 ×224	512×368 ×192	512×416 ×64

To evaluate the efficacy of tSWI in *in vivo* neuro-imaging, we compared the CNR obtained in tSWI data with that obtained in conventional SWI images in three healthy adult volunteers. The study was approved by the local institutional review board and informed consent was obtained from all subjects before the MRI scan. The volunteers were imaged on a 3T Verio system (Siemens, Erlangen) using a 3D SWI sequence with isotropic voxel size of 0.5mm×0.5mm×0.5mm. Imaging parameters are given in Table 6.1. Data were acquired in the transverse orientation. In one case (volunteer 1), the SWI sequence was performed twice using two different echo times (TE = 14.3ms and 17.3ms). To evaluate the influence of voxel aspect ratio on the CNR, lower resolution images of 0.5mm×0.5mm×2mm (anisotropic voxel size) from all 4 volunteer datasets were

generated by taking the central portion of the original k-space along the transverse direction.

The quantitative susceptibility maps were generated for the isotropic and the anisotropic data, as follows: tissues outside the brain were removed using the Brain Extraction Tool (BET) in FSL (17), a homodyne high-pass filter with a k-space window of 64×64 was applied to remove the background field induced phase artefacts (1), and the inversion process to create susceptibility maps was accomplished using a single orientation truncated k-space division approach with a k-space truncation threshold of 0.1 (7). Similar to the case of the simulated data, two sets of tSWI images for each of the SWI datasets were generated using Eqs. 6.1 and 6.2 with: a) χ_1=0 and b)$\chi_1 = 3\sigma_\chi$, where σ_χ is the standard deviation of the susceptibility in the background white matter region close to the vein for which the CNR was measured. The threshold $\chi_2$was kept at 0.45ppm. The susceptibility mask was multiplied into the magnitude image *n* times, with *n* ranging from 1 to 10. To generate conventional SWI images, phase masks were created using the high-pass filtered phase images and then multiplied four times into the magnitude images (1). To investigate the impact of newer data processing methods, we also applied phase unwrapping (18) and SHARP (9) to remove the background field, and applied a geometry constrained iterative algorithm (8) to reconstruct the susceptibility maps for one dataset (Dataset 2). Then, tSWI images were generated using χ_1=0 and χ_2=0.45ppm. Local CNRs of two selected veins, the left internal cerebral vein (LICV) and the right septal vein (RSV), were measured from both tSWI and SWI using Eq. 6.9. Each vessel's ROI was selected from the susceptibility maps and copied onto the tSWI or SWI images for

CNR evaluation. The reference ROI adjacent to each vein was taken from the same slice. To demonstrate the advantages of using tSWI over conventional SWI, we also analyzed one SWI dataset from a TBI patient. For this patient dataset, susceptibility maps were generated through homodyne high-pass filtering and truncated k-space division. tSWI images were then obtained with susceptibility weighting masks generated using χ_1=0, χ_2=0.45ppm and n=2. All the processing was done using Matlab (R2010a, Natick, MA).

6.3 Results

Simulations

The simulated phase images of cylinders of different sizes, their corresponding susceptibility maps and tSWI images are shown in **Fig. 6.2**. The measured CNRs for cylinders with different radii, but with a constant input susceptibility of 0.45ppm, are plotted as a function of *n* in **Fig. 6.3**, and the theoretically predicted CNRs are plotted in **Fig. 6.4**. Since no T2* effects are considered here, the CNRs shown in **Figs. 6.3** and **6.4** reflect contrasts from only phase/susceptibility differences between the cylinders and the background reference region. The optimal choice of *n* and, correspondingly, the value of CNR in the tSWI image, are influenced both by (a) the choices of χ_1 and χ_2 and (b) the high pass filter. For χ_1=0, CNRs reach maximum when $n \leq 4$ (**Figs. 6.3.a, 6.3.c, 6.3.e, 6.4.a** and **6.4.c**). When χ_2 is larger with χ_1=0, it also takes a larger *n* value to reach the optimized CNR. Meanwhile, the choices of χ_1 and χ_2 can also affect the rate at which optimal CNR is approached as a function of *n*. For $\chi_1 = 3\sigma_\chi$, CNRs in general increase as *n* increases (**Figs. 6.3.b, 6.3.d, 6.3.f, 6.4.b** and **6.4.d**). The optimal *n* may be chosen

when CNR reaches 90% of the maximum of CNR. The optimal *n* was 4 for χ_2=0.45ppm, and greater than 10 for χ_2=1ppm.

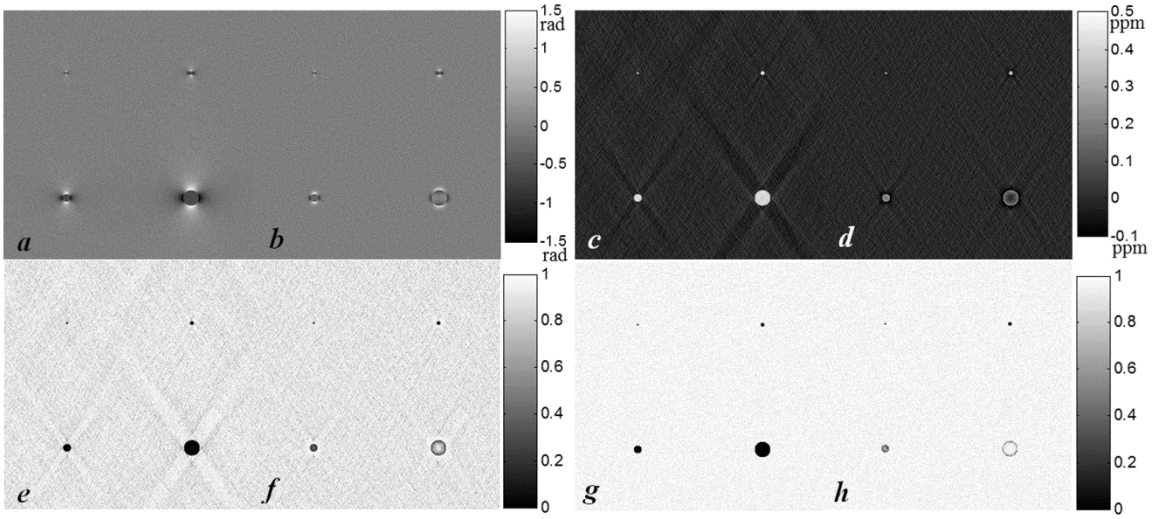

Figure 6.2 Phase images (**a** and **b**), susceptibility maps (**c** and **d**) and tSWI images (**e**, **f**, **g** and **h**) for simulated cylinders with and without homodyne high-pass filtering. Images in the first and third columns are generated using the original phase images without high-pass filtering, while images in the second and fourth columns are generated using high-pass filtering. The tSWI images **e** and **f** were generated using χ_1=0, χ_2=0.45ppm, n=2; while **g** and **h** were generated using $\chi_1=3\sigma_\chi$, χ_2=0.45ppm, n=4. σ_χ is the standard deviation of a reference region measured from the susceptibility maps shown in **c** and **d** (σ_χ=0.05ppm for both **c** and **d**). The SNR in the original magnitude image was set to be 10:1 and the CNR between the cylinders and background in the original magnitude images was basically zero.

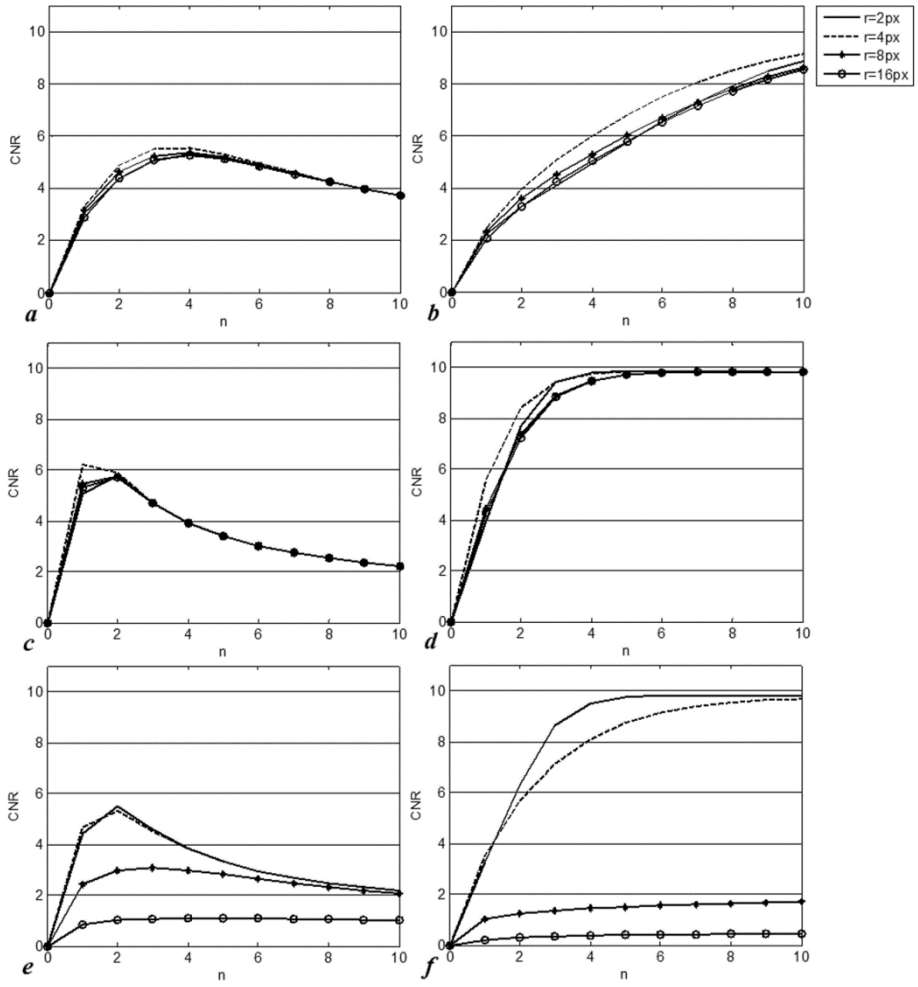

Figure 6.3 Measured CNRs of cylinders from simulated tSWI images. Figures in different rows were generated using different χ_2 values, while figures in different columns were generated using different χ_1 values. **a**) χ_1=0, χ_2=1ppm; **b**) $\chi_1=3\sigma_\chi$, χ_2=1ppm; **c)** χ_1=0, χ_2=0.45ppm; **d)** $\chi_1=3\sigma_\chi$, χ_2=0.45ppm; **e)** χ_1=0, χ_2=0.45ppm; and **f)** $\chi_1=3\sigma_\chi$, χ_2=0.45ppm. To evaluate the effect of high-pass filtering, **e** and **f** were generated using high-pass filtered phase images.

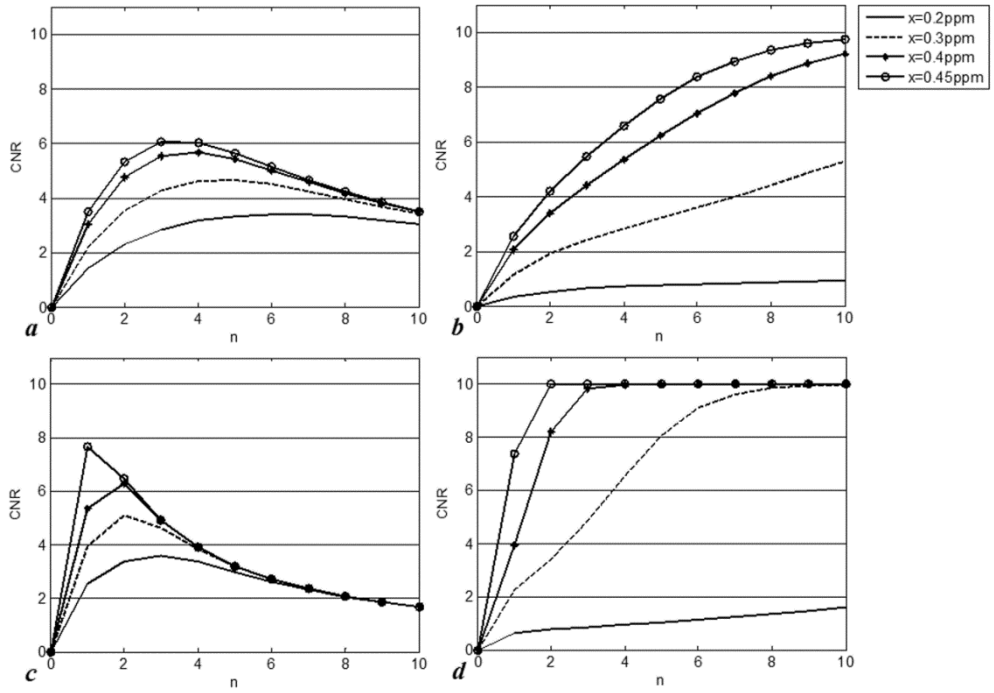

Figure 6.4 Theoretically predicted CNRs of cylinders with different susceptibility values. Figures in different rows were generated using different χ_2 values, while figures in different columns were generated using different χ_1 values. **a)** χ_1=0, χ_2=1ppm; **b**) χ_1=3σ_χ, χ_2=1ppm; **c)** χ_1=0, χ_2=0.45ppm; and **d)** χ_1=3σ_χ, χ_2=0.45ppm.

When a high-pass filtered phase was used, the optimal choice of *n* was not affected much for χ_1=0 and χ_2 = 0.45ppm (**Fig. 6.3.e**), but was slightly bigger for $\chi_1 = 3\sigma_\chi$ and χ_2 = 0.45ppm for all the cylinders except for the smallest one (**Fig. 6.3.f**). For both χ_1 = 0 and $\chi_1 = 3\sigma_\chi$, the maximal CNR was reduced for bigger cylinders, when the high-pass filter was used. This is also partly evident in **Fig. 6.2**. The behavior in the case when the high pass filtered phase was used, agreed with the pattern observed in the theoretically predicted CNRs for objects with low susceptibility in **Fig. 6.4**. Given the simulated results

shown in **Fig. 6.3**, we chose χ_2 = 0.45ppm in the *in vivo* studies for a consistent choice of *n* for the maximal CNR.

In vivo studies

The local CNRs of the two veins, 1) the right septal vein and 2) the left internal cerebral vein, normalized by the SNRs, are plotted in **Figs. 6.5** and **6.6** for all the *in vivo* datasets. The normalized CNRs in the SWI images and in the original magnitude images, as well as the SNRs in the original magnitude images (from the background tissues) are shown in **Table 6.2**. Compared to the original magnitude images, SWI improves the local CNR of the right septal vein in the anisotropic data, but not in the isotropic data. The CNR of the left internal cerebral vein is not improved in SWI in either isotropic or anisotropic data, due to the amplification of the noise in the background tissue region. Compared with the CNRs in magnitude images, the local CNRs in tSWI were improved by roughly a factor of 2 in both isotropic and anisotropic cases for χ_1 = 0. Compared with conventional SWI, the CNRs were improved by a factor of greater than three for datasets with isotropic resolution and greater than 30% for datasets with anisotropic resolution in tSWI. The local CNRs were further improved when $\chi_1 = 3\sigma_\chi$. Considering all cases, when χ_1 = 0 was used, *n* = 2 was a reasonable practical choice for both isotropic and anisotropic datasets; when $\chi_1 = 3\sigma_\chi$ was used, *n* = 4 was a reasonable choice for isotropic datasets and *n* = 8 for anisotropic datasets.

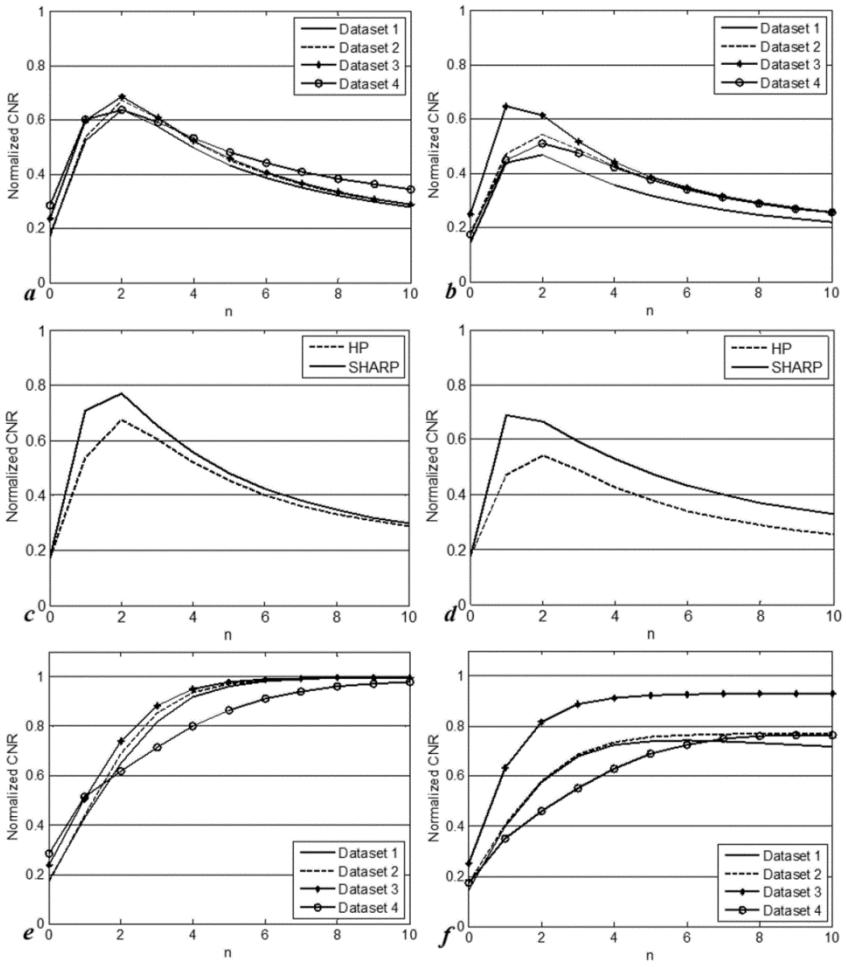

Figure 6.5 Local CNRs of the right septal vein (**a**, **c**, and **e**) and the left internal cerebral vein (**b**, **d**, and **f**) from different datasets with isotropic resolution. **a**, **b**, **c** and **d** were generated when threshold $\chi_1=0$ was used to create the susceptibility weighting masks, while **e** and **f** were generated when $\chi_1=3\sigma_\chi$ was used. The CNRs were normalized by the corresponding SNRs listed in **Table 6.2**. **c** and **d** show the CNRs of the two veins in Dataset 2 with isotropic resolution, when different data processing methods were used for susceptibility mapping (see **Fig. 6.7** for examples of the tSWI images).

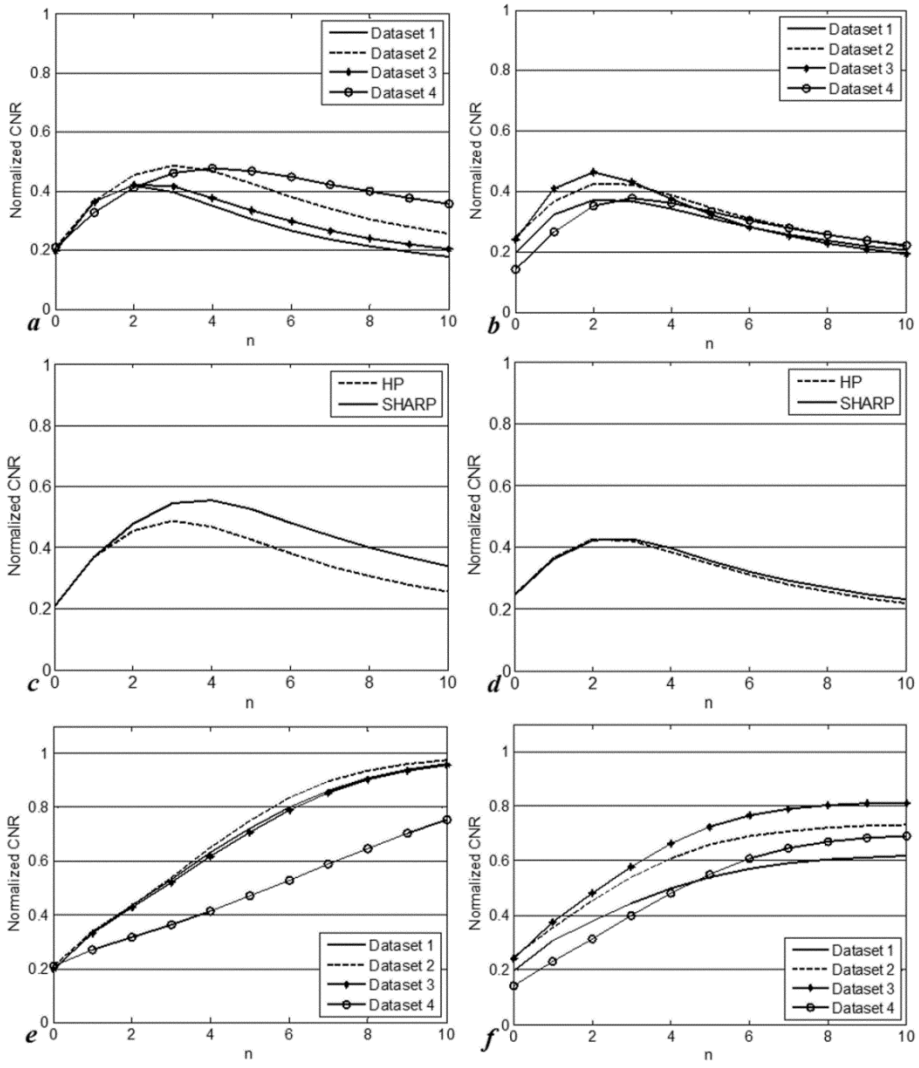

Figure 6.6 Local CNRs of the right septal vein (**a**, **c**, and **e**) and the left internal cerebral vein (**b**, **d**, and **f**) from different datasets with anisotropic resolution. **a**, **b**, **c** and **d** were generated when threshold χ_1=0 was used to create the susceptibility weighting masks, while **e** and **f** were generated when $\chi_1=3\sigma_\chi$ was used. The CNRs were normalized by the corresponding SNRs listed in **Table 6.2**. **c** and **d** show the CNRs of the two veins in Dataset 2 with anisotropic resolution, when different data processing methods were used for susceptibility mapping (see **Fig. 6.7** for examples of the tSWI images).

When SHARP along with an iterative algorithm (8) was used to generate susceptibility maps, the CNRs of the two veins of interest in the corresponding tSWI image were improved, as shown in **Figs. 6.5.c, 6.5.d, 6.6.c** and **6.6.d**. For isotropic resolution, at *n*=2 with χ_1 = 0, the relative improvements for the left internal cerebral vein and the right septal vein were 23% and 14%, respectively. For anisotropic resolution and at *n*=2, the relative improvements for the two veins were less than 5%. However, this improvement in CNR was more significant for grey matter structures than for veins, as can be seen from **Fig**. **6.7.d** and **6.7.h**.

In **Fig. 6.7**, we compare the tSWI and SWI minimum intensity projections for both the isotropic and anisotropic cases. The tSWI appears to have higher CNR than the conventional SWI in both isotropic and anisotropic data. For tSWI, isotropic data provided a better delineation of the venous structures, compared to the anisotropic data. This is consistent with the results shown in **Figs**. **6.5** and **6.6**, in which the normalized maximal CNRs are higher for the isotropic data than those for the anisotropic data. When $\chi_1 = 3\sigma_\chi$ was used, the visibility of some tiny veins and the grey matter structures was reduced compared to the case when χ_1 = 0 was used.

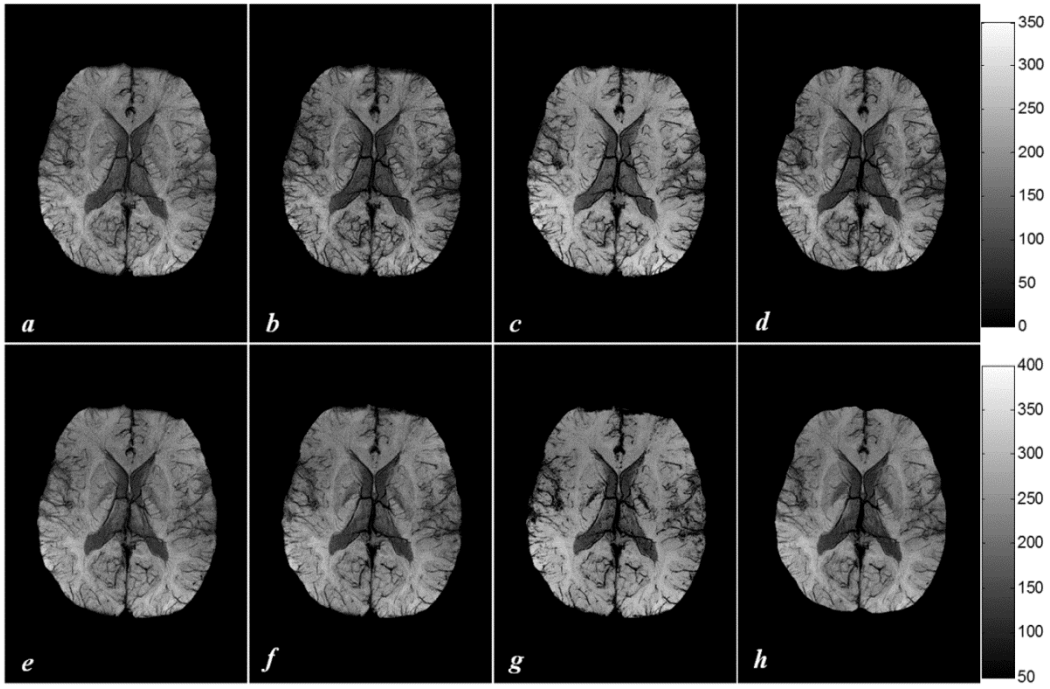

Figure 6.7 Comparison between minimal intensity projections (mIP) of tSWI and SWI data over 16mm for isotropic (top row) and anisotropic data (bottom row) for Dataset 2. For ***b***, ***c***, ***f*** and ***g***, susceptibility maps were generated using homodyne high-pass filtering and thresholded k-space division; while for ***d*** and ***h,*** susceptibility maps were generated using SHARP and geometry constrained iterative algorithm. ***a***) isotropic SWI mIP; ***b***) isotropic tSWI mIP (χ_1=0, χ_2=0.45ppm, n=2); ***c***) isotropic tSWI mIP (χ_1=3σ_χ, χ_2=0.45ppm, n=4); ***d***) isotropic tSWI mIP (χ_1=0, χ_2=0.45ppm, n=2); ***e***) anisotropic SWI mIP. ***f***) anisotropic tSWI mIP (χ_1=0, χ_2=0.45ppm, n=2). ***g***) anisotropic tSWI mIP (χ_1=3σ_χ, χ_2=0.45ppm, n=8). ***h***) anisotropic tSWI mIP (χ_1=0, χ_2=0.45ppm, n=2).

As an example of this process with χ_1 = 0, χ_2 = 0.45ppm and n = 2, **Fig. 6.8** shows a case that demonstrates the problems with the conventional SWI processing: one of the veins has a trajectory roughly at the magic angle (54.7°) with respect to the direction of the main magnetic field B_0. The black arrow shows the vein which is clearly seen in the tSWI (**Fig. 6.8.f**). In SWI (**Fig. 6.8.e**), the vein actually shows a dark structure which is in fact more associated with its edges. This makes the veins appear much bigger in the SWI than in the tSWI data, as can be seen from the minimum intensity projections (mIPs) in **Figs. 6.8.g** and **6.8.h**. This non-local phase information used in SWI can lead to an inaccurate estimation of the geometry of microbleeds, as demonstrated in **Fig. 6.9**. In this TBI case, tSWI has more faithfully represented the microbleeds.

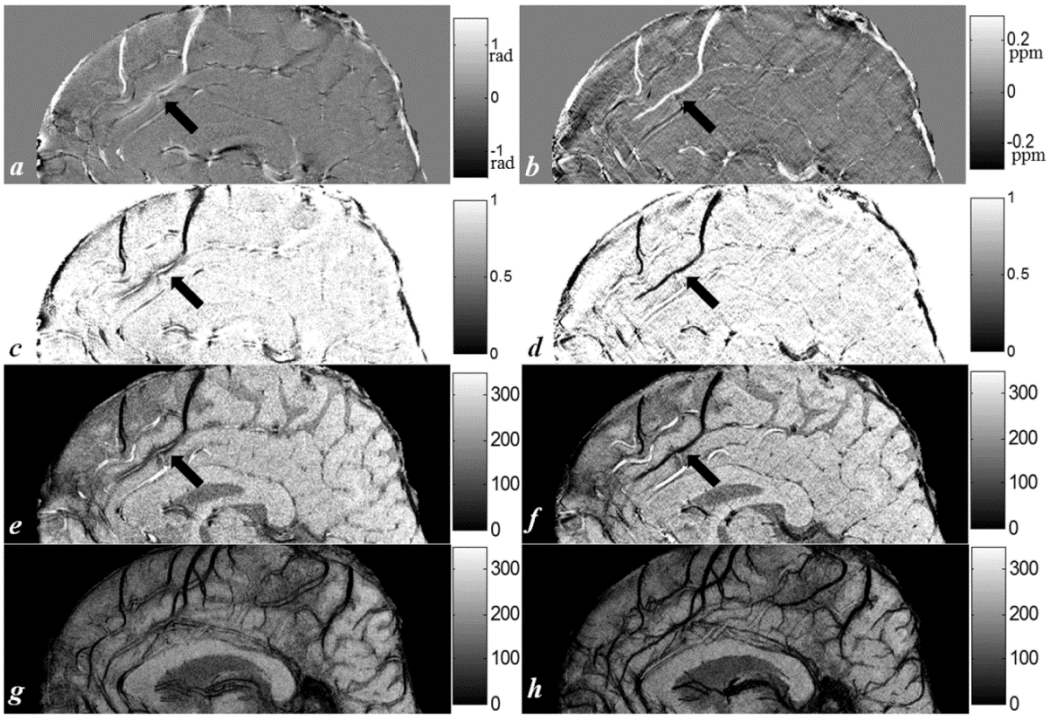

Figure 6.8 A sagittal view showing a vein near the magic angle (54.7° relative to the main magnetic field) as indicated by the black arrows. **a**) Phase image (from a left-handed system) showing effectively zero phase inside the vein, with outer field dipole effects also visible; **b**) susceptibility maps showing the vein as uniformly bright; **c**) susceptibility weighting mask obtained from the phase image (n=4); **d**) susceptibility weighting mask obtained from the susceptibility maps (χ_1=0, χ_2=0.45ppm, n=2); **e**) SWI showing unsuppressed signal inside the vein; and **f**) tSWI showing a clear suppression of the vein even at the magic angle. **g**) mIP of SWI in the sagittal direction. **h**) mIP of tSWI in the sagittal direction. Note the vessels near the magic angle are now well delineated in the tSWI data.

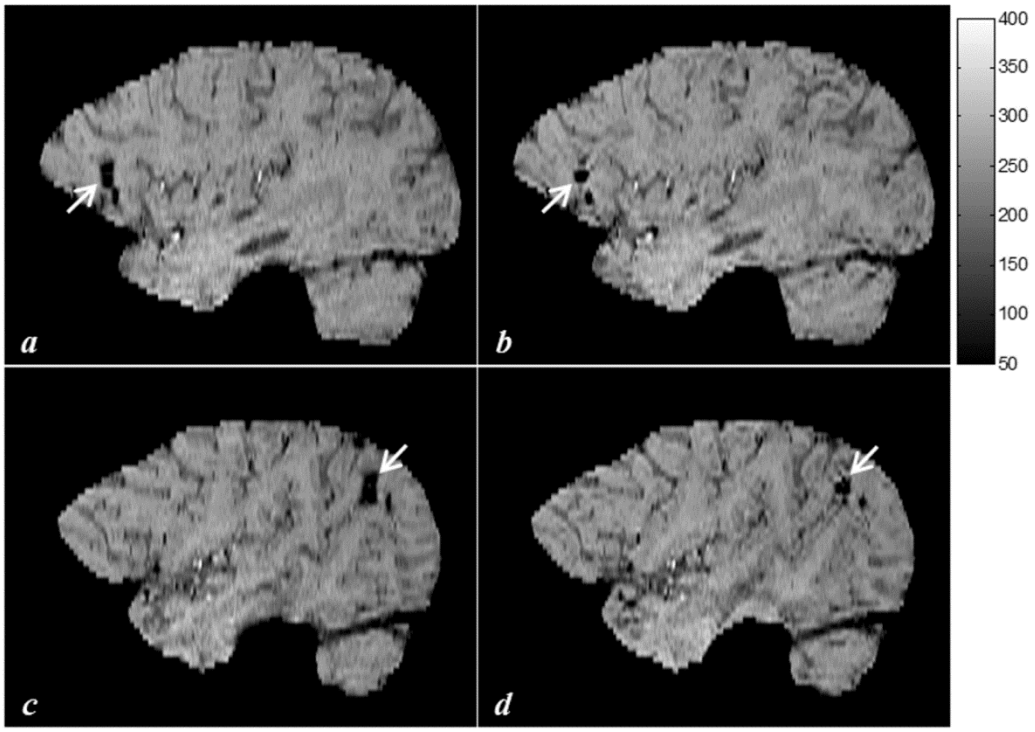

Figure 6.9 Sagittal views of SWI (**a** and **c**) and tSWI images (**b** and **d**) in a TBI case. The microbleeds appear much bigger on the SWI images than on the tSWI images, as indicated by the white arrows. This is due to the non-local phase information used in the conventional SWI weighting mask. For better visualization, the images were interpolated in through-plane direction from a resolution of 0.5mm×0.5mm×2mm to 0.5mm isotropic resolution.

6.4 Discussion

Quantitative susceptibility mapping offers an additional means to recognize veins and microbleeds and other tissues with high iron content as phase imaging does. However, the phase images are dependent on each object's shape and orientation while the susceptibility values of the structures are not, at least in principle. Therefore, to produce

better susceptibility weighted images, we have investigated the use of susceptibility maps for the masking process.

There are a number of key observations that can be made from the data presented herein. First, the results presented in this paper demonstrate that the object shape and orientation can be reasonably accounted for by using susceptibility maps and, hence, the inability of SWI processing to enhance veins at different orientations can be overcome. Besides, the blooming artefact due to the dipolar phase of microbleeds in conventional SWI was avoided. This leads to potential applications of this technique, for example, the evaluation of microbleeds in TBI studies. Nonetheless, the blooming artefact also enables the visualization of small or even sub-voxel structures using conventional SWI (6). In this case, due to the severe partial volume effects, the susceptibility values will not be accurately estimated and it is expected that tSWI will lead to similar results as conventional SWI. Second, tSWI can be used to process isotropic data, whereas SWI processing has relied on anisotropic data for its best results due to the direct use of phase information which is orientation dependent (6). In the past, SWI data have usually been collected with anisotropic resolution with 2mm slice thickness(6). However, modern segmented echo planar approaches are becoming viable and one expects to see more data being collected with isotropic voxel sizes (19,20). The high isotropic resolution also helps to reduce the error caused by the partial volume effects in susceptibility quantification, and thus leads to improved quality for tSWI. Note that, high image resolution will also lead to lower SNR within a given image time and thus lower CNR. Generally speaking, tSWI is most advantageous with the isotropic datasets. Third, the use of a susceptibility

mask is not restricted to the paramagnetic venous blood, but it could also be designed to study the diamagnetic materials (e.g., calcifications, which have negative susceptibility in the susceptibility maps). Fourth, the effects of the upper and lower thresholds used in creating the susceptibility masks have been studied for two reasonable values, and the optimal number of multiplications, *n* has been determined. When the lower threshold was set to zero, the fact that a continuous mask from zero to unity is generated makes it possible to enhance contrast even in smaller veins, or larger veins that have had their phase artificially suppressed by using the high-pass filter, or in structures that have lower iron contents. The use of $\chi_1 = 3\sigma_\chi$ helps to avoid amplifying noise in regions of low susceptibility and hence leads to a higher CNR. However, at the same time it can prevent small veins or structures with very low susceptibility from being enhanced. In addition, different datasets require different optimal *n* values. To avoid this problem, it may be more practical to choose χ_1 to be 0. We choose the upper threshold χ_2 to be 0.45ppm, as it corresponds to the theoretical susceptibility of venous blood when the oxygen saturation is 70% and the hematocrit is 45%. Increasing this upper threshold may lead to a slightly larger value for the optimal *n* when the susceptibility value of the vein is much smaller than χ_2. In most cases, *n* = 2 gave optimal results, for χ_1 = 0 and χ_2 = 0.45ppm. In order to capture smaller veins or structures with lower susceptibility values such as the basal ganglia, a slightly larger *n* can be used for either isotropic or anisotropic datasets (21). The lower susceptibility values are due to a combined effect of partial volume and high-pass filtering. Fifth, the predicted CNRs slightly deviate from measured CNRs in simulations, as the mean value of the susceptibility mask W in the background reference

region is slightly less than 1. As a result, this creates slight differences between the prediction and measurements at large n values ($n > 4$). Lastly, conventional SWI uses phase information which is dependent on echo time and usually a relatively long echo time is used in SWI data collection. Although the phase mask could be redefined as a function of echo time to accommodate the loss of phase information as echo times are reduced, no such modification needs to take place for tSWI since the susceptibility map does not change with echo time. However when echo times are reduced the phase SNR used to generate the susceptibility map will decrease. On the other hand, if echo times become too long, phase aliasing occurs and the apparent size of the vessel will increase. Thus, tSWI makes the use of short echo times possible as long as the SNR is high enough to create a reasonable estimate of the local susceptibilities. The selection of a shorter TE has several major advantages, including reducing background field induced phase artefacts, shorter scan time and better overall image quality.

There are several limitations to this method. First, we are using susceptibility maps generated from a single orientation dataset to create the mask for tSWI. These susceptibility maps can have streaking artefacts which are caused by the singularities in the inverse kernel (7–15). The streaking artefacts could permeate the tSWI data causing artefacts which did not exist before or decrease the CNR of grey matter structures. Some newer techniques such as nonlinear regularization (10,13,14) and iterative algorithms (8) will reduce the streaking artefacts and the latter is particularly time-efficient. Another common problem of the single orientation QSM method is the systematic under-estimation or bias of the susceptibility. However, this can be compensated by the

thresholds used to generate the tSWI weighting masks. Second, we used the traditional homodyne high-pass filter to remove the background phase artefacts in the *in vivo* data. Even though homodyne high-pass filtering could be applied without phase unwrapping, it leads to an underestimation of the susceptibility, especially for large objects. This can be improved by using newly developed background field removal methods (9,22). But for relatively small structures such as veins, homodyne high-pass filtering already gives satisfying results if it is performed in the appropriate plane (see Chapter 3). Given the fact that homodyne high-pass filtering is still being widely used, the proposed algorithm can be directly added to the current SWI data processing scheme.

In conclusion, we have proposed a data processing scheme which we refer to as true SWI or tSWI to generate SWI like images using susceptibility maps. This helps to avoid the orientation dependence related problem in SWI, especially in data with isotropic resolution and, in the future, possibly to allow the use of short TE SWI data collection. This tSWI data provide better and more consistent visualization of the venous system and thus have potential clinical applications in the study of neurodegenerative diseases.

References

1. Haacke EM, Xu Y, Cheng YN, Reichenbach JR. Susceptibility weighted imaging (SWI). Magn. Reson. Med. 2004;52:612–8.
2. Mittal S, Wu Z, Neelavalli J, Haacke EM. Susceptibility-Weighted Imaging: Technical Aspects and Clinical Applications, Part 2. Am. J. Neuroradiol. 2009;30:232–52.
3. Haacke EM, Reichenbach JR, editors. Susceptibility Weighted Imaging in MRI: Basic Concepts and Clinical Applications. 1st ed. Wiley-Blackwell; 2011.
4. Haacke EM, Brown RW, Thompson MR, Venkatesan R. Magnetic Resonance Imaging: Physical Principles and Sequence Design. 1st ed. Wiley-Liss; 1999.
5. Marques J p., Bowtell R. Application of a Fourier-based method for rapid calculation of field inhomogeneity due to spatial variation of magnetic susceptibility. Concepts Magn. Reson. Part B Magn. Reson. Eng. 2005;25B:65–78.
6. Xu Y, Haacke EM. The role of voxel aspect ratio in determining apparent vascular phase behavior in susceptibility weighted imaging. Magn. Reson. Imaging 2006;24:155–60.
7. Haacke EM, Tang J, Neelavalli J, Cheng YC. Susceptibility mapping as a means to visualize veins and quantify oxygen saturation. J. Magn. Reson. Imaging 2010;32:663–76.
8. Tang J, Liu S, Neelavalli J, Cheng YCN, Buch S, Haacke EM. Improving susceptibility mapping using a threshold-based K-space/image domain iterative reconstruction approach. Magn. Reson. Med. 2013;69:1396–407.
9. Schweser F, Deistung A, Lehr BW, Reichenbach JR. Quantitative imaging of intrinsic magnetic tissue properties using MRI signal phase: An approach to in vivo brain iron metabolism? NeuroImage 2011;54:2789–807.
10. Schweser F, Sommer K, Deistung A, Reichenbach JR. Quantitative susceptibility mapping for investigating subtle susceptibility variations in the human brain. NeuroImage 2012;62:2083–100.
11. Shmueli K, de Zwart JA, van Gelderen P, Li T, Dodd SJ, Duyn JH. Magnetic susceptibility mapping of brain tissue in vivo using MRI phase data. Magn. Reson. Med. 2009;62:1510–22.
12. Liu T, Spincemaille P, de Rochefort L, Kressler B, Wang Y. Calculation of susceptibility through multiple orientation sampling (COSMOS): A method for conditioning the inverse problem from measured magnetic field map to susceptibility source image in MRI. Magn. Reson. Med. 2009;61:196–204.
13. Liu J, Liu T, de Rochefort L, Ledoux J, Khalidov I, Chen W, et al. Morphology enabled dipole inversion for quantitative susceptibility mapping using structural consistency between the magnitude image and the susceptibility map. NeuroImage 2012;59:2560–8.
14. De Rochefort L, Liu T, Kressler B, Liu J, Spincemaille P, Lebon V, et al. Quantitative susceptibility map reconstruction from MR phase data using bayesian regularization: Validation and application to brain imaging. Magn. Reson. Med. 2010;63:194–206.

15. Wharton S, Bowtell R. Whole-brain susceptibility mapping at high field: A comparison of multiple- and single-orientation methods. NeuroImage 2010;53:515–25.
16. Jain V, Abdulmalik O, Propert KJ, Wehrli FW. Investigating the magnetic susceptibility properties of fresh human blood for noninvasive oxygen saturation quantification. Magn. Reson. Med. 2012;68:863–7.
17. Smith SM. Fast robust automated brain extraction. Hum. Brain Mapp. 2002;17:143–55.
18. Abdul-Rahman HS, Gdeisat MA, Burton DR, Lalor MJ, Lilley F, Moore CJ. Fast and robust three-dimensional best path phase unwrapping algorithm. Appl. Opt. 2007;46:6623–35.
19. Xu Y, Haacke EM. An iterative reconstruction technique for geometric distortion-corrected segmented echo-planar imaging. Magn. Reson. Imaging 2008;26:1406–14.
20. Zwanenburg JJM, Versluis MJ, Luijten PR, Petridou N. Fast high resolution whole brain T2* weighted imaging using echo planar imaging at 7T. NeuroImage 2011;56:1902–7.
21. Gho S-M, Liu C, Li W, Jang U, Kim EY, Hwang D, et al. Susceptibility map-weighted imaging (SMWI) for neuroimaging. Magn. Reson. Med. 2013; doi: 10.1002/mrm.24920.
22. Liu T, Khalidov I, de Rochefort L, Spincemaille P, Liu J, Tsiouris AJ, et al. A novel background field removal method for MRI using projection onto dipole fields (PDF). NMR Biomed. 2011;24:1129–36.

Chapter 7 Quantitative Susceptibility Mapping of Small Objects using Volume Constraints[3]

7.1 Introduction

The measurement of magnetic susceptibility offers an entirely new form of contrast in magnetic resonance imaging (1-6). More specifically, susceptibility quantification has already found applications in mapping out iron in the form of ferritin in brain tissues such as the basal ganglia (1, 4, 6) and in the form of deoxyhemoglobin for measuring the oxygen saturation in veins (1, 4). This new form of imaging may provide a means for monitoring longitudinal changes in iron content in dementia, multiple sclerosis (MS), traumatic brain injury (TBI) and Parkinson's disease (PD). It may also be used to monitor microbleeds which have been implicated in the progression of vascular dementia (7), Alzheimer's and other neurovascular disorders (8, 9).

[3]Most of the contents in this chapter are adapted from Liu S, Neelavalli J, Cheng Y-CN, Tang J, Haacke EM. Quantitative susceptibility mapping of small objects using volume constraints. Magn. Reson. Med. 2013;69:716–23. Reprint under license.

One of the most recent susceptibility mapping methods is a Fourier based method (2, 3, 5, 10) which utilizes phase images. The accuracy of such a method depends on the volume measurement of the object. For example, in order to quantify the susceptibility of a given microbleed, usually the center and the radius of the microbleed have to be determined (10-13). Alternate volume estimations of the microbleed from high resolution spin echo images may overcome these limitations. With a gradient echo sequence, the apparent volume of the object is increased due to what is commonly referred to as the "blooming" effect, a signal loss around the object caused by T_2^* dephasing. This increased apparent volume may be used to obtain an estimated susceptibility of the object while the product of the apparent volume and the estimated susceptibility is much more robust and should still provide a good estimate of the magnetic moment of the object.

The goal of this paper is to evaluate the quantitative accuracy of a Fourier based susceptibility mapping method when it is applied to small structures, and to show that: 1) an accurate estimate of the magnetic moment is possible using multi-echo gradient echo imaging; and 2) the accuracy of the effective susceptibility can be improved using the magnetic moment when an estimate of the true volume is available. For validation, we used a gel phantom with air bubbles and glass beads to mimic the clinical situation of microbleeds. The method illustrated here does not depend on the susceptibility value or the size of the object.

7.2 Theory and Methods

Current susceptibility mapping methods are based on the relation between the susceptibility distribution and the magnetic field variation in the Fourier domain (1-6; 10):

$$\Delta B(\vec{k}) = B_0 G(\vec{k}) \Delta\chi(\vec{k}) \quad [7.1],$$

where $\Delta B(\vec{k})$ is the Fourier transform of the magnetic field variation $\Delta B(\vec{r})$, $\Delta\chi(\vec{k})$is the Fourier transform of the susceptibility distribution $\Delta\chi(\vec{r})$, and $G(\vec{k})$ is the Green's function

$$G(\vec{k}) = 1/3 - k_z^2/(k_x^2 + k_y^2 + k_z^2) \quad [7.2],$$

assuming that the main field direction is in the z direction. Susceptibility quantification is an ill-posed inverse problem, due to zeros in the Green's function $G(\vec{k})$ along the magic angle in the k-space domain. As a result, regularization is required. In this study, we applied the regularization procedure described in a previous study (1) in which the intensity of the inverse of $G(\vec{k})$ is reasonably attenuated when the absolute value of $G(\vec{k})$ is below a threshold value, *th*. The selection of this threshold is a trade-off between the susceptibility-to-noise ratio of the reconstructed susceptibility map and the accuracy in susceptibility quantification (1, 6). The threshold value was chosen to be 0.1 in this study.

Although ideally $\Delta\chi$ is the sought after parameter, when reduced resolution or T_2^* effects confound a clean measurement of the object's volume, it is more appropriate to investigate the associated magnetic moment (or, equivalently, the total or integrated

susceptibility weighted by the voxel volume (12)). To see why this is the case, consider a sphere with a susceptibility difference $\Delta\chi$, the induced magnetic field at point $P(\vec{r},\theta)$ outside the sphere is given by (14):

$$\Delta B_{out}(\vec{r}) = \frac{\Delta\chi r_0^3(3\cos^2\theta-1)B_0}{3r^3} \quad [7.3]$$

where $\Delta\chi = \chi_{in} - \chi_{out}$, χ_{in} is the susceptibility inside the object, χ_{out} is the susceptibility outside the object, r_0 is the radius of the sphere, r is the distance from the point $P(\vec{r},\theta)$ to the center of the sphere, and θ is the angle between the point P and the main field direction. For simplicity, the meaning of susceptibility in this paper will be taken to be $\Delta\chi$ rather than χ_{in} or χ_{out}. Eq. 7.3 also indicates that the product $\Delta\chi V$ is independent of TE, where $V = 4\pi r_0^3/3$ is the true volume of the sphere. Since the magnetic dipole moment of the spherical object is given as (14):

$$\mu = \frac{4\pi r_0^3 M(\Delta\chi)}{3} \approx \frac{4\pi r_0^3 \Delta\chi B_0}{3\mu_0} \quad [7.4],$$

when $\Delta\chi \ll 1$. For simplicity we refer to the product $\Delta\chi V$ as the magnetic moment in this study. The phase value at a particular echo time (TE) is given in a right handed system by:

$$\Delta\varphi(\vec{r}) = -\gamma\Delta B(\vec{r})TE \quad [7.5].$$

The susceptibility $\Delta\chi$ may be quantified using the phase information, if the true volume (V) of the object is known. Otherwise, the magnetic moment ($\Delta\chi V$) may be found. Since gradient echo images lead to a dephasing artefact and the object appears larger than its actual size, we defined an apparent volume V' and assuming that the susceptibility of this

larger object can be accurately quantified, the magnetic moment could still be accurately calculated. Expressed symbolically, an estimated susceptibility value $\Delta\chi'$ can be calculated from the Fourier based method using Eqs. 7.1 to 7.5. The quantity $\Delta\chi'V'$ provides an estimate of the magnetic moment. Finally, the true susceptibility $\Delta\chi$ can be calculated using the following equation:

$$\Delta\chi = \Delta\chi'V'/V \quad [7.6].$$

In this study, we use three volume definitions. The first one is the true volume *V*. The second one is the apparent volume *V'*, which is used in estimating the magnetic moment. The apparent volume is related to the signal loss due to T_2^* dephasing and is determined from gradient echo magnitude images, as described later. The last one is the spin echo volume V_{se}, which is measured from the spin echo images. This volume is used as an MR based estimate of the true volume of the air bubble or glass bead. We used simulations and multi-echo gradient echo images of a gel phantom containing air-bubbles and glass beads of varying sizes to test Eq. 7.6. While glass beads can be considered as almost perfect spheres, air bubbles are closer to the clinical situation of variable shaped microbleeds.

Simulations

To evaluate validity of Eq. 7.6 for susceptibility calculation of small objects, we simulated magnitude and phase images of 4 spheres with different radii at 21 different TEs (from 0 ms to 20 ms, with a step size of 1 ms). In each simulation, the sphere was placed in the center of a 1024^3 matrix with complex elements. The radii of four spheres

tested, within this 1024^3 matrix, were 32, 48, 64 and 96 pixels, respectively. The magnitude inside each sphere was set to 0 while the background magnitude was set to 300 to simulate intensities in the experimental data from the gel phantom. The phase images of the spheres were generated according to Eqs. 7.3 and 7.5 with $\Delta\chi = 9.4$ ppm. In order to simulate Gibbs ringing as well as partial volume effects seen in actual MR data, a process simulating the MR data sampling was used. Complex images generated in each 1024^3 matrix were Fourier transformed into k-space. The central 32^3 region was selected from k-space and was inverse Fourier transformed back to the imaging domain generating low resolution data containing both Gibbs ringing and partial volume effects. The radii of the four spheres became 1, 1.5, 2 and 3 pixels respectively in this final 32^3 volume. White Gaussian noise was then added to the real and imaginary channels of the complex data in the image domain such that the SNR in resultant magnitude images was 10:1. Susceptibility and the magnetic moment values were quantified for each of the spheres at all echo times and errors associated with these measurements were evaluated.

Phantom experiments

A gel phantom, containing 14 small air-bubbles and 9 glass beads of varying sizes, was imaged at 3T (Siemens VERIO, Erlangen, Germany) using a five-echo 3D gradient echo sequence. The echo times (TEs) were 3.93ms, 9.60ms, 15.27ms, 20.94ms and 26.61ms. Other imaging parameters for the gradient echo sequence were: repetition time (TR) 33ms, flip angle (FA) 11º, read bandwidth (BW) 465 Hz/pixel, voxel size $0.5\times0.5\times0.5 mm^3$, and matrix size 512×304×176. A multi-slice 2D spin echo dataset was also collected with FA = 90º, TR = 5000ms and TE = 15ms and with the same field of view (FOV), BW,

resolution and matrix size as in the gradient echo dataset. This is to maintain a one-to-one correspondence of the spin echo with the gradient echo images of the phantom. To ensure that the field perturbation measured in the phase images is the actual perturbation profile from the gel phantom, we first performed shimming using a spherical phantom immediately before performing the imaging experiment. Manual shimming was performed on the spherical phantom, to a spectral full width at half maximum of 13 Hz and the shim coefficients were noted. The same shim settings were used while imaging the gel phantom to ensure that field perturbation profile due to the presence of the phantom in the magnet is not influenced by any additional shimming.

For the construction of the phantom, an agarose gel solution was prepared with an 8% concentration by weight and poured into a cylindrical container. In the lower portion of the container, the gel was first filled to 1/3 the height of the cylinder and 9 glass beads of various sizes were embedded in the gel. The true diameter of the glass beads was roughly measured using calipers before the glass beads were put into the gel solution. Specifically, 4 glass beads were 2mm in diameter, 3 glass beads were 3mm in diameter, 1 glass bead was 5mm in diameter, and the largest glass bead was 6mm in diameter. The phantom was allowed to cool so that the gel solidified and properly engulfed the glass beads. Rest of the prepared gel solution was then poured into the cylindrical container and variable sized bubbles were injected by pumping various amount of air into the gel using an empty syringe (two smallest air bubbles were excluded from this study, due to the limitation in volume estimation of small objects. Details are provided in later sections). The theoretical susceptibility difference between air and water is known to be 9.4ppm and will be used to

compare with the measurements from our method. For glass beads, the susceptibility values were measured independently in a former study to be −1.8 +/- 0.3ppm (15).

First, in order to identify air bubbles and glass beads in the collected MR data, binary masks from magnitude data were used. The intensity variation in the magnitude images caused by the RF field inhomogeneity was first removed using a 2D quadratic fitting, before the binary masks were created. A reasonably uniform magnitude intensity profile across the phantom was obtained after this intensity correction. The binary masks were created by local thresholding of the corrected magnitude images (11). First, a relatively strict threshold is used to pick only the voxels where the signal is less than 50% of the signal-to-noise ratio (SNR) in the gel away from the air bubbles or glass beads, since both air bubbles and glass beads have much lower intensities than the intensity of the surrounding gel. Next, the mean ($\alpha_{mag,gel}$) and standard deviation ($\sigma_{mag,gel}$) were calculated for a cubic 21×21×21 VOI for each bubble or glass bead. A voxel roughly at the center of the bubble or glass bead was first chosen to center this 21^3 voxel window. The voxels picked up in the first step were excluded in the mean and standard deviation calculation. If a neighboring voxel has intensity lower than $\alpha_{mag,gel} - \beta\sigma_{mag,gel}$, it was regarded as a voxel belonging to air or glass bead. For the high SNR data used here, β was empirically chosen to be 4 to separate air bubbles and glass beads from gel.

Susceptibility Quantification

In order to reduce the background field or phase variation, a forward modeling approach was used to estimate air/gel-phantom interface effects (16). The phase processing steps were as follows:

i. The original phase images were first unwrapped using the phase unwrapping tool, PRELUDE, in FMRIB Software Library (FSL) (17). With the geometry of the gel phantom extracted from the magnitude images at the shortest TE (3.93ms in this study), the background field effects were reduced by fitting the predicted phase to the unwrapped phase by a least squares method. An additional 2D quadratic fitting was added in order to remove the induced phase due to eddy currents.

ii. The phase value inside a particular air bubble/glass bead (where the binary mask is 1) was set to the mean phase (essentially zero) from the local 9260 voxels. This is due to the fact that the phase inside a sphere is theoretically zero and the nonzero phase is induced by the remnant background field variation as well as Gibbs ringing. This step also determines the apparent volume (V') from magnitude images.

iii. At each echo time, a 160×160×87 voxel volume was cropped from the original phase images. This volume was selected because it covers most of the air bubbles and glass beads while voxels near the edge of the gel phantom were excluded. The selected volume was then zero-filled to a 512×512×256 matrix.

iv. Susceptibility maps were generated using a threshold based approach described previously in (1). The mean ($\alpha_{\chi,air}$ *or* $\alpha_{\chi,glass}$) and standard deviation ($\sigma_{\chi,air}$

or $\sigma_{\chi,glass}$) of the susceptibility values of air bubble (or glass bead) were measured, taking into account the background susceptibility of the gel. Measurements were obtained in the following manner: the background mean ($\alpha_{\chi,gel}$) and standard deviation ($\sigma_{\chi,gel}$) of the local gel susceptibility value around each bubble or glass bead was first calculated from the 21^3 voxel region centered at each of the bubble/bead. Within this 21^3 volume, the voxels belonging to the bubble or glass bead, as determined by the binary mask, were excluded for this background mean and standard deviation calculation. Once these measures were obtained, for susceptibility of air bubbles, only voxels with susceptibility values higher than $\alpha_{\chi,gel} + 3\sigma_{\chi,gel}$ were used for calculation purposes; while for glass beads, only voxels with a susceptibility value lower than $\alpha_{\chi,gel} - 3\sigma_{\chi,gel}$ were used. This process assumes that the noise in the susceptibility maps follows a Gaussian distribution, and the susceptibility of a voxel consisting of air or glass is statistically different from a voxel consisting of gel. The change in sign is due to the fact that the air bubbles are paramagnetic relative to the gel while glass beads are diamagnetic. To account for the baseline shift caused by remnant field variation, the susceptibility of the air bubble (or glass bead) was taken as $\alpha_{\chi,air} - \alpha_{\chi,gel}$ (or $\alpha_{\chi,glass} - \alpha_{\chi,gel}$).

Comparison with recent data processing algorithms

In addition to the above described data processing steps, the phantom data were also processed using newer data processing algorithms to further reduce the streaking artefact in the susceptibility maps and to improve the accuracy of susceptibility quantification.

The background phase was removed using SHARP with radius 6 pixels, regularization threshold 0.05 (18). Susceptibility maps were generated using the k-space/image domain iterative algorithm (19). The geometries of the air bubbles and glass beads were extracted from magnitude images at different TEs. In each iteration step, the regions outside the air bubbles or glass beads were set to 0, while the regions inside the bubbles and beads were smoothed using an edge-preserving averaging filter. Then the cone of singularities in the original k-space was updated. The phase inside the air bubbles and glass beads was still set to zero initially, and was updated using the predicted phase from forward calculation using the susceptibility maps in each iteration step. The susceptibilities of the air bubbles and glass beads were measured in the same way as described in the previous section.

Volume Measurement

The apparent volume of the air bubble or glass bead was determined from the binary masks directly, i.e., by counting the number of voxels inside the air bubble or glass bead. On the other hand, the spin echo volume is measured utilizing the "object strength" notion proposed by Tofts et al (20), in which the total intensity is measured for a particular volume of interest (VOI). For a volume composed of two types of tissues, a and b, the total intensity can be expressed as

$$I = I_a \cdot n_a + I_b \cdot (N - n_a) \; = \; (I_a - I_b) \cdot n_a + I_b \cdot N \qquad [7.7],$$

where I is the total intensity, "I_a" and "I_b" are the intensities of the voxels containing purely tissue "a" or tissue "b", respectively. The total number of voxels in this volume of interest is denoted by "N", and the number of voxels occupied by tissue "a" is denoted by

"n_a". Consequently, the number of voxels occupied by tissue "b" can be expressed as $N - n_a$.

By varying the size of the VOI, the total intensity is linearly dependent on the number of voxels in the VOI. While "I_b" can be determined as the slope in the fit to Eq. 7.7, n_a can be calculated from the intercept if "I_a" is given (n_a may not be an integer as partial volume is included). In this study, "I_b" corresponds to the intensity of a voxel composed purely of gel, while "I_a" corresponds to the intensity of a voxel composed purely of air or glass. For a relatively large air bubble or glass bead, "I_a" is dominated by the thermal noise, which can be approximated as $1.25\sigma_{mag,gel}$, where $\sigma_{mag,gel}$ is the measured standard deviation of the gel region in the magnitude images (21). For an air bubble or glass bead with a radius generally less than 3 pixels, "I_a" is a combination of thermal noise and Gibbs ringing. To best account for these fluctuations, "I_a" is calculated as:

$$I_a = \begin{cases} w_1 \cdot \alpha_{mag,air} + w_2 \cdot 1.25\sigma_{mag,gel}, & for\ air\ bubbles \\ w_1 \cdot \alpha_{mag,glass} + w_2 \cdot 1.25\sigma_{mag,glass}, & for\ glass\ beads \end{cases} \quad [7.8]$$

where $\alpha_{mag,air}$ and $\alpha_{mag,glass}$ are the measured mean values inside the bubble and glass bead, respectively; w_1 and w_2 are two weighting factors. Based on our simulations (explained below), w_1 and w_2 were empirically determined from simulations to be 0.4 and 0.6 respectively, to minimize the error in estimation of the true volume.

Error in Volume Measurement

Although a regression method is used to measure the spin echo volume, it is still affected by partial volume effects, Gibbs ringing as well as random noise. The simulated magnitude images at TE=0 were used to mimic spin echo magnitude images and to study the error in spin echo volume estimation. In addition, to examine the stability of this method due to thermal noise, the volume measurement evaluation was performed 10 times for each simulated sphere, with independently generated random noise for each of these simulations. The errors were determined by comparing the measured volume with the true volume. Note that, this error estimation does not apply for the apparent volume which is determined directly from the binary masks.

7.3 Results

Simulations

Magnetic moments for simulated spheres were calculated with the measured susceptibilities and the apparent volume for each sphere at a given echo time. The results across different TEs are shown in **Fig. 7.1**. The measured volumes at different TEs were normalized to the volume at the longest TE, while the measured magnetic moments were normalized to the true magnetic moment, which is the product of input volume (i.e., the true volume) of the sphere and the input susceptibility (true susceptibility) 9.4 ppm. The normalized magnetic moment is roughly a constant for all spheres. However, for the sphere with a radius less than 2 pixels, the magnetic moments measured in the short TE range have more fluctuations than those measured at longer TEs. In addition, the magnetic moments are under-estimated for all spheres. The mean normalized magnetic

moments were measured as: 0.85±0.04 (radius=1 pixel), 0.82±0.05 (radius=1.5 pixels), 0.81±0.03 (radius=2 pixels) and 0.81± 0.02 (radius=3 pixels).

After the magnetic moments were obtained, the susceptibility values were corrected using the actual known volume (i.e., true volume) using Eq. 7.6. Specifically, the corrected susceptibilities are: 7.95±0.38ppm (radius=1pixel), 7.70±0.43ppm (radius=1.5pixels), 7.62±0.27 (radius=2pixels), and 7.63±0.21 (radius=3pixels). There is still a 15% to 19% under-estimation in the averaged susceptibility after attempting to correct the volume of the sphere.

To evaluate the stability of the volume measuring method, we carried out 10 simulations for each sphere at TE=0. The means and standard deviations of the percentage errors relative to true volume for each sphere are: 18.02±27.26% (radius=1pixel), 1.89±12.18% (radius=1.5pixels), 3.67±8.91% (radius=2pixels) and 2.09±2.54% (radius=3pixels). The algorithm failed to quantify, in two of the 10 simulations for sphere with radius of 1pixel. Larger errors and more variations of the volume measurements were seen in spheres with radii less than 2 pixels. For the sphere with a radius of 3 pixels, the error in the volume estimation appears to be within 5% using the proposed method. As can be expected, when the object radius is only 1 pixel, the volume measurement becomes unstable.

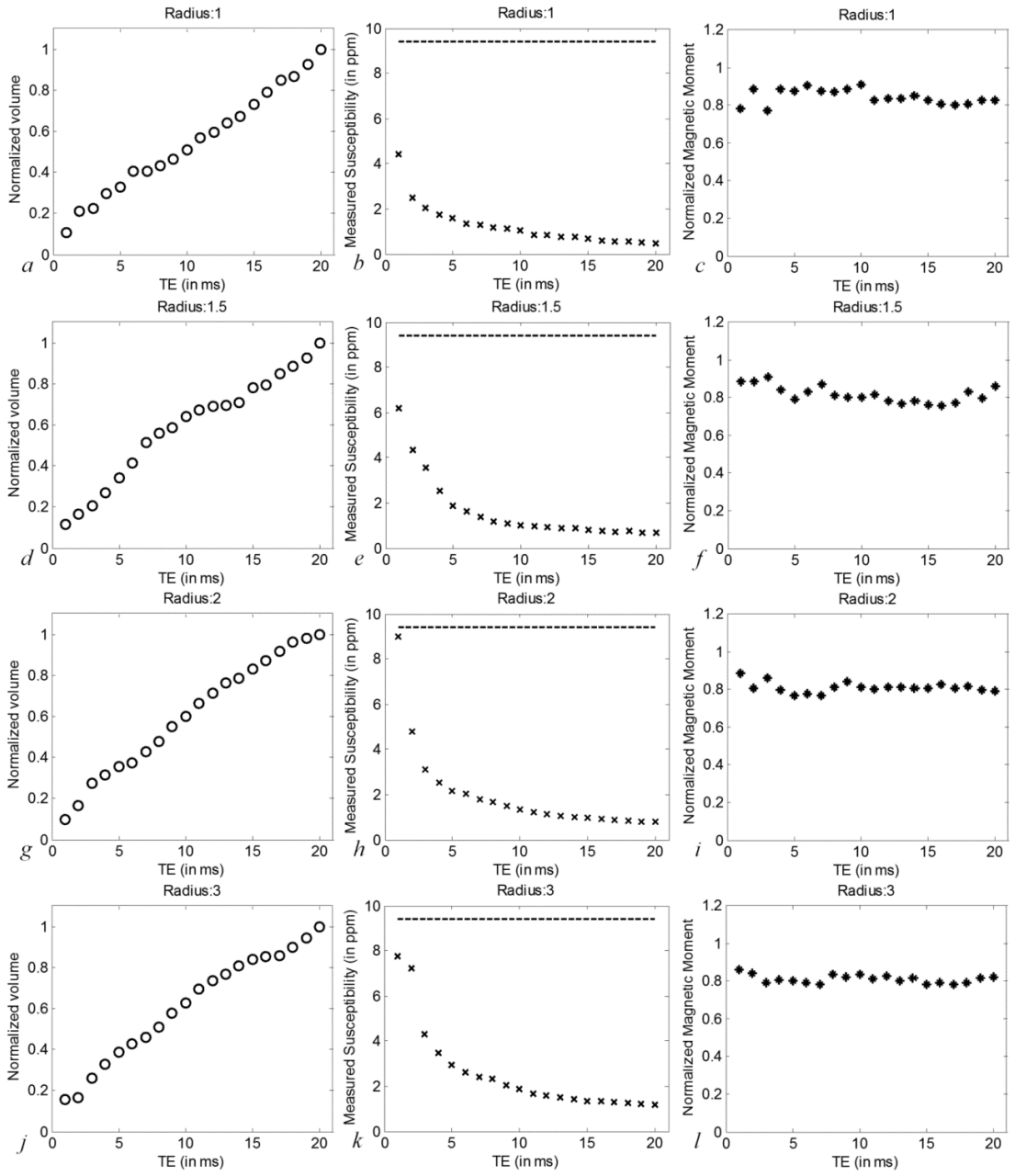

Figure 7.1 Apparent volume normalized to the volume at TE = 20 ms (first column), measured susceptibility (second column), and normalized magnetic moments (third column) measured at different TEs of four different spheres. The dashed lines in the second column (***b***, ***e***, ***h*** and ***k***) indicate the true susceptibility 9.4 ppm. For each sphere, the effective magnetic moments were normalized to the true effective magnetic moment.

Phantom experiments

A total of 14 air bubbles and 9 glass beads were examined in the phantom data. The measured spin echo volumes of the glass beads and air bubbles are shown in **Tables 7.1** and **7.2**. In these two tables, the glass beads as well as air bubbles are sorted based on their spin echo volumes, from small to large objects. The diameters of these glass beads calculated from their spin echo volumes agree reasonably well with their physically measured diameters, as shown in **Table 7.1**. Also note that, the error in volume measurement is unreliable for spherical objects with radii less than 1.5 pixels (14.13 voxels for the volume). The error is generally larger than 20%, as shown in the simulations. Thus, the first two smallest air bubbles were excluded from the analysis.

Fig. 7.2 shows three orthogonal views of the susceptibility map of the largest glass bead for the shortest TE and the longest TE. **Fig. 7.3** shows the susceptibility maps obtained using the newer data processing algorithms. Compared with the former results, the streaking artefacts are reduced and the objects are more homogeneous.

Table 7.1 Spin echo volume (in voxels) and the diameter (in mm) calculated from spin echo volume for each glass bead.

Measure \ Bead	**1**	**2**	**3**	**4**	**5**	**6**	**7**	**8**	**9**
Spin Echo Volume	35.4	37.5	38.2	39.1	96.5	103.8	113.6	516.6	912.1
Spin Echo Diameter	2.0	2.1	2.1	2.1	2.9	2.9	3.0	5.0	6.0
Actual Diameter	2.0	2.0	2.0	2.0	3.0	3.0	3.0	5.0	6.0

Table 7.2 Spin echo volume (in voxel) of the 14 air bubbles.

Bubble	**1**	**2**	**3**	**4**	**5**	**6**	**7**
Volume	3.3	15.1	28.7	42.2	43.9	82.8	87.7
Bubble	**8**	**9**	**10**	**11**	**12**	**13**	**14**
Volume	92.7	118.2	170.5	238.6	288.7	322.7	897.2

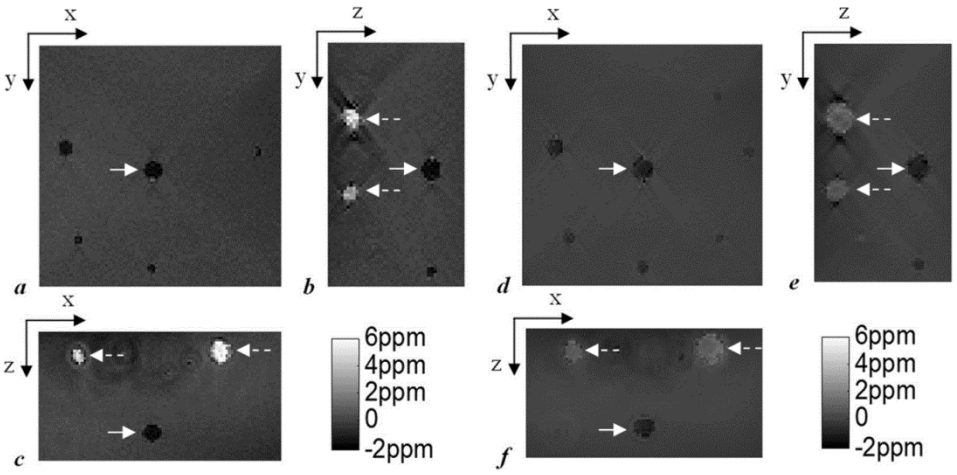

Figure 7.2 Axial, sagittal and coronal views of the susceptibility maps with TE=3.93ms (**a**, **b** and **c**) and TE=26.61ms (**d**, **e** and **f**). The main field direction is in "**y**" direction. Glass bead No. 9 in **Table 7.1** is pointed by the white arrows. The air bubbles are pointed by the white dashed arrows.

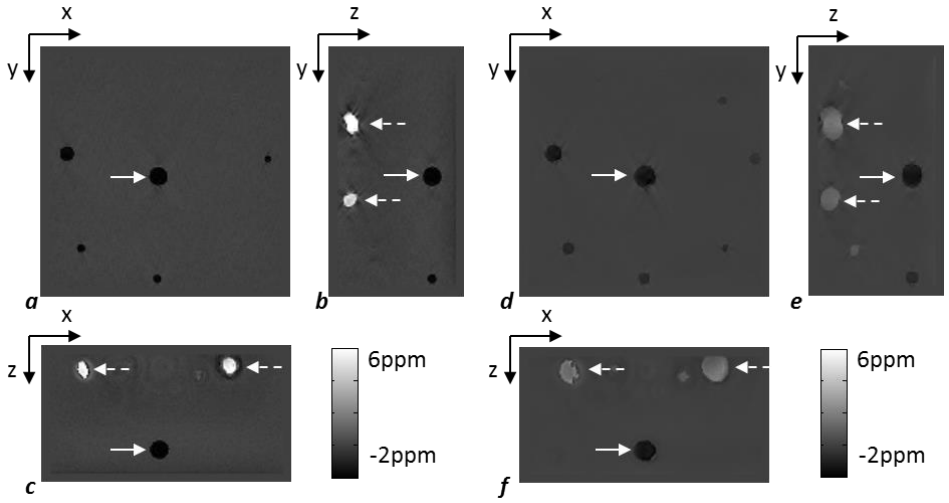

Figure 7.3 Axial, sagittal and coronal views of the susceptibility maps with TE=3.93ms (**a**, **b** and **c**) and TE=26.61ms (**d**, **e** and **f**), obtained using newer data processing algorithms.

Using Eq. 7.6, the measured susceptibilities can be corrected with the volume estimated from the spin echo images. These results were shown in **Table 7.3**. The results obtained using the newer algorithms were shown in **Table 7.4**. Using the original data processing methods (i.e. geometry based artefact reduction together with 2D quadratic fitting for background field removal, and truncated k-space division for susceptibility mapping), the mean of the corrected susceptibility values of the glass beads averaged over all the TEs was −1.82±0.17ppm, which is within the range of the measured values in the previous study (15). The mean of the corrected susceptibility values of the air bubbles was 6.66±0.85ppm. This is to be compared to the actual susceptibility of 9.4ppm. Using the new data processing algorithms (i.e. SHARP for background field removal, iterative SWIM for susceptibility mapping), the corrected average susceptibility of the glass beads was -2.12±0.15ppm, and the corrected average susceptibility of the air bubbles was 7.35±1.13ppm.

The susceptibility values estimated using the newer data processing algorithms are plotted as a function of echo time in **Fig. 7.4.** As shown in **Fig. 7.4.a**, the absolute susceptibility values of both the air bubbles and glass beads decreases as TE increases, due to the over-estimated volume. And the corrected susceptibility values are almost constant over different TEs, indicating that the product of susceptibility and the measured volume, or the effective magnetic moment, is also constant. After correction, both the distributions of susceptibility of air bubble and glass beads became narrower, indicating reduced uncertainties in the susceptibility estimates, as shown in **Fig. 7.4.c** and **7.4.d**.

Table 7.3 Mean measured and corrected susceptibilities (in ppm) of the glass beads and air bubbles and different TEs.

	Glass Bead		Air bubble	
TE/ms	**Measured**	**Corrected**	**Measured**	**Corrected**
3.93	-1.50±0.07	-1.79±0.13	3.15±1.16	6.13±0.77
9.60	-1.07±0.32	-1.76±0.13	1.70±0.61	6.44±0.90
15.27	-0.86±0.32	-1.82±0.19	1.30±0.45	6.64±0.76
20.94	-0.68±0.28	-1.82±0.18	1.07±0.36	6.88±0.77
26.61	-0.59±0.25	-1.88±0.21	0.93±0.34	7.22±0.74

Table 7.4 Mean measured and corrected susceptibilities (in ppm) of the glass beads and air bubbles and different TEs. These results were obtained using the new data processing algorithms.

	Glass Bead		Air bubble	
TE/ms	**Measured**	**Corrected**	**Measured**	**Corrected**
3.93	-1.73±0.06	-2.06±0.15	3.58±1.41	7.24±1.01
9.60	-1.29±0.35	-2.13±0.15	1.87±0.68	7.40±1.16
15.27	-1.02±0.38	-2.16±0.16	1.36±0.48	7.39±1.20
20.94	-0.79±0.34	-2.10±0.14	1.08±0.37	7.35±1.21
26.61	-0.68±0.29	-2.17±0.18	0.89±0.31	7.38±1.23

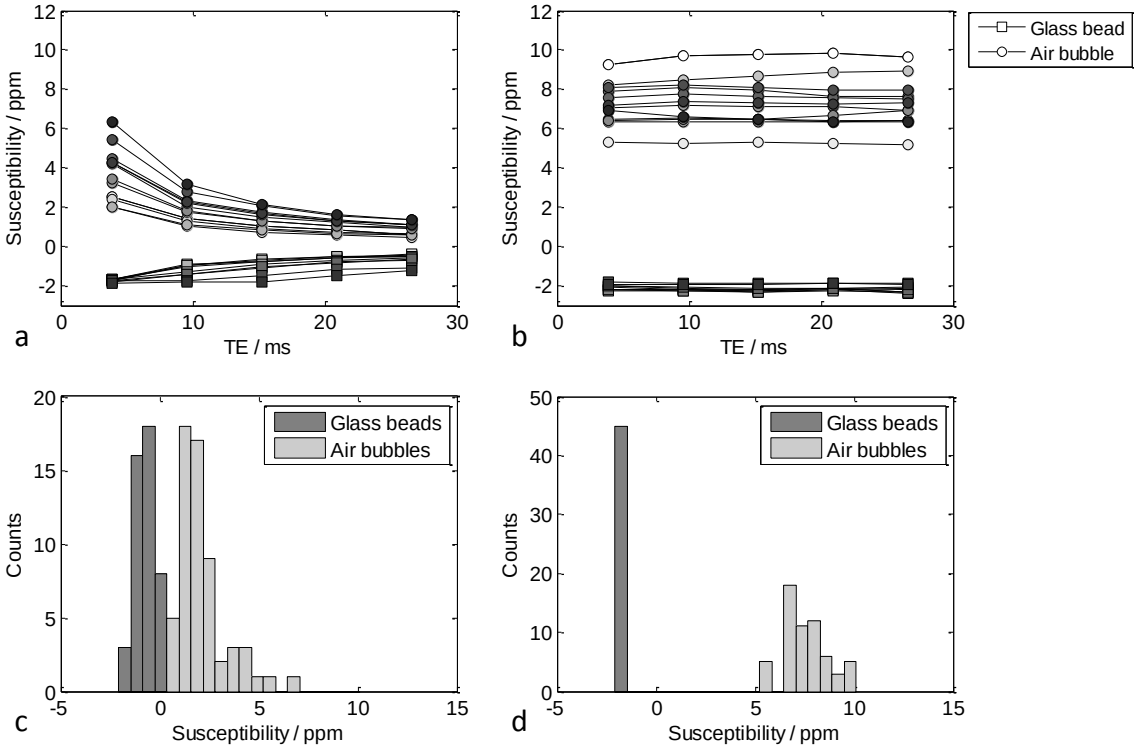

Figure 7.4 a) Originally measured susceptibility values at different TEs for glass beads and air bubbles. **b**) Corrected susceptibility values. **c**) Distribution of the originally measured susceptibility values. **d**) Distribution of the corrected susceptibility values. After correction using the spin echo volume, the glass beads can be clearly distinguished from air bubbles. These results were obtained using the new data processing algorithms.

7.4 Discussion and Conclusions

The susceptibility mapping technique using the regularized Fourier based method has certain advantages over other methods, especially in terms of time-efficiency and simplicity. However, it suffers from problems caused by the intrinsic singularities in the inverse of the Green's function, as well as partial volume effects which disrupt the true

phase behavior. For small objects, susceptibility quantification using the inverse method (1) yields a significant under-estimation of the susceptibility. The increased apparent volume at long TE can be utilized to create a larger virtual object, for which the true volume can be more accurately measured and thus the Fourier based susceptibility quantification gives a relatively smaller error for the magnetic moment. At this point, the susceptibility close to the actual value can be extracted from the estimated magnetic moment with an estimation of the true volume, either if it is known ahead of time, or it can be estimated from a high resolution spin echo dataset.

Based on the discussions above, the error $\delta\Delta\chi$ in the corrected susceptibility $\Delta\chi$ comes from the estimated magnetic moment $\mu_a = \Delta\chi' V'$ and estimated volume (V). Through error propagation, the error in the corrected susceptibility is given by:

$$\frac{\delta\Delta\chi}{|\Delta\chi|} = \sqrt{\left(\frac{\delta\mu_a}{\mu_a}\right)^2 + \left(\frac{\delta V}{V}\right)^2} \qquad [7.9]$$

As can be seen from Eq. 7.9, the smaller the error in the estimated volume, the smaller the error in the corrected susceptibility. This equation explains the error seen in the corrected susceptibility of the air bubbles as well as glass beads.

In simulations, where the true volume is known, the remnant under-estimation in the averaged corrected susceptibility ranges from 15% to 19%. Since there is no error in the true volume, this error must be due to the error in the apparent volume measurement and $\Delta\chi'$ quantification due to the regularization process. The level of under-estimation is related to the threshold value in the inverse of the Green's function. A smaller threshold

leads to less under-estimation, but more streaking artefacts in the susceptibility maps. The regularized Fourier based method, with threshold value of 0.1, can lead to an under-estimation of around 13% for objects with radii larger than 3 pixels and even worse for smaller objects (1, 6). This can be viewed as a systematic error, and can be reduced using the k-space/image domain iterative algorithm, as shown in previous chapters.

In phantom studies, using high-pass filtered phase images and truncated k-space division for generating susceptibility maps, the corrected susceptibility values of the air bubbles have a maximum underestimation close to 44%, compared to the theoretical value 9.4ppm, even after using the volume estimated from the spin echo data. This is essentially a consequence of three factors: the error in the spin echo volume measurement, the signal loss due to high-pass filtering, and the under-estimation of $\Delta\chi'$ quantified using the truncated k-space division method. To overcome the limitations related to volume estimation, one has to go to high resolution images that can minimize volume quantification error. However, the decreased SNR in high resolution spin echo images may introduce additional variation/noise in the final volume results.

The accuracy in the susceptibility estimation can be further improved using more sophisticated background field removal and susceptibility mapping methods. Using the newer data processing algorithms, the background phase was better reduced. Particularly, the streaking artefacts surrounding the air bubbles and glass beads were largely reduced due to the use of geometry constrained iterative SWIM algorithm. Finally, the phase values of the pixels inside the air bubbles and glass beads are not reliable, due to the low

signal inside these objects. This is solved by updating the phase values inside, using the predicted phase, during the iterative SWIM algorithm. This helps to get a faster convergence. All of these help to improve the accuracy in estimating the susceptibilities of small objects with low signal inside.

There are a number of limitations to this study. Even though a forward calculation was carried out to reduce the geometry induced field variation, remnant background field variation still exists. To best account for it, the phase inside the spherical objects was set to the local average phase. This also helps to reduce the large variation in susceptibility estimate induced by Gibbs ringing and thermal noise. However, this phase correction process is based on the assumption that the object of interest is a sphere. For non-spherical objects, this phase correction process may lead to variations of magnetic moment at different TEs. In addition, phase correction also creates a virtually larger object. It is possible that the center of the created object deviates from the true center of the original object of interest. This leads to additional errors even for spherical objects, as seen from simulations. Thus, the phase inside the spherical object has significant effects to this method. Theoretically, only when the center of a simulated large sphere coincides with the original center of the sphere, and when the background phase value is 0, can we obtain constant magnetic moment across different TEs. Hence, slight variation in object definition from binary mask, which is used for phase substitution, can introduce variations in magnetic moment values. This is the essential source of shape dependence of the proposed method.

Although the estimated magnetic moments of the glass beads are almost a constant over different TEs, as indicated by the corrected susceptibilities, the estimated magnetic moments of the air bubbles are usually larger at a longer TE than at a shorter TE. This can be understood by the fact that the air bubbles are not perfect spherical objects compared to the glass beads. In fact, most of the air bubbles have ellipsoidal shapes, and any attempt of phase correction inside the bubble based on the assumption of the spherical shape will cause errors in the susceptibility measurement and thus lead to errors in the measurement of the magnetic moments.

Generally speaking, for small objects which can be well approximated as spheres, the theoretically expected errors in the estimated magnetic moment measurements are within 20% of the expected values and can be further reduced by adjusting the regularization thresholds in the susceptibility mapping method. Practically, the errors might be larger due to the limited knowledge of the true volume. While most small microbleeds can be well approximated as spheres, the use of more accurate volume estimation methods has the potential to reduce the error in susceptibility quantification of microbleeds.

In conclusion, we have shown that for very small structures, obtaining accurate magnetic susceptibility values is limited by the errors in the volume estimations of these structures and in the Fourier based method itself. Despite this inability to estimate the actual volume of a small object accurately (whether it is an air bubble or microbleed), the estimated magnetic moment is almost a constant over different TEs. This demonstrates that it is possible to measure the magnetic moment at a longer TE when the apparent volume is

increased due to T_2^* dephasing. By measuring or knowing *a priori* the actual volume of an object, it is possible to obtain a reasonable estimate of the susceptibility.

Acknowledgments This work is supported in part by National Institutes of Health via grants NHLBI R01HL062983-A4 and NHLBI R21 HL 108230-A2. This work is also supported in part by the Wayne State University Perinatal Research Initiative.

References

1. Haacke EM, Tang J, Neelavalli J, Cheng YC. Susceptibility mapping as a means to visualize veins and quantify oxygen saturation. Journal of Magnetic Resonance Imaging 2010; 32(3):663-676.
2. Liu T, Spincemaille P, de Rochefort L, Kressler B, Wang Y. Calculation of susceptibility through multiple orientation sampling (COSMOS): A method for conditioning the inverse problem from measured magnetic field map to susceptibility source image in MRI. Magnetic Resonance in Medicine 2009; 61(1):196-204.
3. de Rochefort L, Brown R, Prince MR, Wang Y. Quantitative MR susceptibility mapping using piece-wise constant regularized inversion of the magnetic field. Magnetic Resonance in Medicine 2008; 60(4):1003-1009.
4. Schweser F, Deistung A, Lehr BW, Reichenbach JR. Quantitative imaging of intrinsic magnetic tissue properties using MRI signal phase: An approach to in vivo brain iron metabolism? NeuroImage 2011; 54(4):2789-2807.
5. Wharton S, Schäfer A, Bowtell R. Susceptibility mapping in the human brain using threshold-based k-space division. Magnetic Resonance in Medicine 2010; 63(5):1292-1304.
6. Shmueli K, de Zwart JA, van Gelderen P, Li T, Dodd SJ, Duyn JH. Magnetic susceptibility mapping of brain tissue in vivo using MRI phase data. Magnetic Resonance in Medicine 2009; 62(6):1510-1522.
7. Ayaz M, Boikov AS, Haacke EM, Kido DK, Kirsch WM. Imaging cerebral microbleeds using susceptibility weighted imaging: One step toward detecting vascular dementia. Journal of Magnetic Resonance Imaging 2010; 31(1):142-148.
8. Greenberg SM, Vernooij MW, Cordonnier C, Viswanathan A, Al-Shahi Salman R, Warach S, Launer LJ, Van Buchem MA, Breteler MM. Cerebral microbleeds: a guide to detection and interpretation. The Lancet Neurology 2009; 8(2):165-174.
9. Yates PA, Sirisriro R, Villemagne VL, Farquharson S, Masters CL, Rowe CC, For the AIBL Research Group. Cerebral microhemorrhage and brain β-amyloid in aging and Alzheimer disease. Neurology 2011; 77(1):48 -54.
10. Cheng Y-CN, Neelavalli J, Haacke EM. Limitations of calculating field distributions and magnetic susceptibilities in MRI using a Fourier based method. Physics in Medicine and Biology. 2009; 54(5):1169-1189.
11. McAuley G, Schrag M, Barnes S, Obenaus A, Dickson A, Holshouser B, Kirsch W. Iron quantification of microbleeds in postmortem brain. Magnetic Resonance in Medicine 2011; 65(6):1592-1601.
12. Liu T, Surapaneni K, Lou M, Cheng L, Spincemaille P, Wang Y. Cerebral Microbleeds : Burden Assessment by Using Quantitative Susceptibility Mapping. Radiology (2012); 262(1):269-78.
13. Cheng Y-C, Hsieh C-Y, Neelavalli J, Haacke EM. Quantifying effective magnetic moments of narrow cylindrical objects in MRI. Physics in Medicine and Biology. 2009; 54(22):7025-7044.
14. Haacke EM, Brown RW, Thompson MR, Venkatesan R. Magnetic Resonance Imaging: Physical Principles and Sequence Design. 1st ed. Wiley-Liss; 1999.

15. Hsieh C, Cheng Y, Tackett R, Kumar R, Lawes G, Haacke E. TH-D-304A-02: Quantifying Magnetic Moments and Susceptibilities of Small Spherical Objects in MRI. Medical Physics 2009; 36:2816.
16. Neelavalli J, Cheng YN, Jiang J, Haacke EM. Removing background phase variations in susceptibility-weighted imaging using a fast, forward-field calculation. Journal of Magnetic Resonance Imaging 2009; 29(4):937-948.
17. Jenkinson M. Fast, automated, N-dimensional phase-unwrapping algorithm. Magnetic Resonance in Medicine 2003; 49(1):193-197.
18. Schweser F, Deistung A, Lehr BW, Reichenbach JR. Quantitative imaging of intrinsic magnetic tissue properties using MRI signal phase: An approach to in vivo brain iron metabolism? NeuroImage. 2011 Feb 14;54(4):2789–807.
19. Tang J, Liu S, Neelavalli J, Cheng YCN, Buch S, Haacke EM. Improving susceptibility mapping using a threshold-based K-space/image domain iterative reconstruction approach. Magn Reson Med. 2013 May;69(5):1396–407.
20. Tofts PS, Silver NC, Barker GJ, Gass A. Object strength-an accurate measure for small objects that is insensitive to partial volume effects. MAGMA 2005; 18(3):162-169.
21. Gudbjartsson, H., and Patz, S. The Rician distribution of noisy MRI data. Magnetic Resonance in Medicine 1995; 34(6):910-914.

Chapter 8 Conclusions and Future Directions

Quantitative susceptibility mapping (QSM) is a promising technique to study tissue properties such as iron content and function such as oxygen extraction *in vivo*. In this thesis, several technical advances in the QSM methodology have been made which will accelerate the data processing and improve the accuracy of QSM.

First, the quality of QSM is largely dependent on background field removal. From the results of simulations and *in vivo* data studies, the spherical mean value filtering (SMV) based techniques are the most effective method, both in terms of the time-efficiency and accuracy. However, the regions close to the edge of the brain are usually eroded in order to avoid noisy pixels outside the brain. This is the main remnant problem of these SMV based background field removal algorithms. For studies focused on the cerebral venous oxygen saturation, the superior sagittal sinus (SSS) is of great interest. But the accuracy of the extracted local phase information for the superior sagittal sinus is poor, since SSS is sitting at the edge of the brain and may be partly removed by the brain extraction step. Thus, it is critical to keep this structure using the binary brain mask and to keep the phase at the edge of the SSS or even outside the SSS in the skull (1,2).

The Local Spherical Mean Value filtering (LSMV) algorithm proposed in this thesis improves the robustness and efficiency for background field removal. It is particularly time-efficient for processing data collected with double- or multi- echo. The main advantage of this algorithm is avoiding global phase unwrapping and the reduction of phase signal loss near the edges of the veins due to T_2^* signal decay. It can also be used for processing of data collected with a single short TE. The local background field removal also helps to reduce the effects of cusp artefacts/phase singularities, which are typically caused by improper combination of multi-channel data.

Proper multi-channel phase data combination is critical for data collected using phased array coils and parallel imaging techniques such as GRAPPA (3). Any improper combination of the phase will lead to signal cancellation and cusp artefacts (4,5). For regions inside the brain, the cusp artefacts can be avoided by correcting the linear gradients and baseline differences of different channels. But for regions outside the brain, such a simple correction may still lead to cusp artefacts (6). This is again due to the difference in the phase references of different channels, ϕ_0, which contains both the coil-sensitivity induced phase components and the conductivity induced phase components. Thus, the ideal phase combination should have the ϕ_0 removed from each channel before combining all the channels' data. This can be done by using either a reference scan or reference echo (6). In the former method, usually the reference scan is performed using coils with relatively uniform sensitivity profile. In the latter method, the TE of the reference echo could be chosen such that it equals half of the TE of the main scan. Then ϕ_0 can be calculated using these two echoes using complex division (without phase

unwrapping). Removing these spatially varying ϕ_0 effects will then lead to an improved QSM reconstruction.

Second, QSM is essentially an ill-posed inverse problem. For solving the inverse problem, the main difference in currently available algorithms is related to the handling of the gradients/edges in the susceptibility maps. In order to suppress false gradients caused by the streaking artefacts, the gradients estimated from magnitude images and phase images or a combination of both are usually used as *a priori* information (7,8). Care should be taken when imposing these *a priori* constraints. While a false edge detected from magnitude or phase images will reduce the effectiveness in removing the streaking artefacts in the susceptibility maps, a missed edge will lead to over-smoothing of the susceptibility maps. For clinical studies, the processing time for these methods is also of concern, especially when large numbers of datasets with large matrix size are involved. The k-space/image domain iterative algorithm (iterative SWIM) is a promising method, precisely because of its proper preserving of the edge information in the susceptibility maps and its time-efficiency. As validated using simulated data and *in vivo* data, this iterative SWIM algorithm is particularly effective for studies focused on measuring venous oxygen saturation.

An improved version of the iterative SWIM algorithm, which utilizes the geometries of the structures found in the susceptibility maps for solving the inverse problem, is demonstrated in this thesis. Instead of using the geometries of the structures with high susceptibilities, e.g., veins, as in the original iterative SWIM algorithm (9), in the

improved version proposed in this thesis, both the geometries of the veins and grey matter structures (with relatively high susceptibilities) were extracted and utilized in solving the inverse problem. This improves the accuracy of susceptibility estimation of both the veins and the grey matter structures.

The accuracy of QSM is also dependent on the estimation of the volume, especially for small objects (10). Longer TE gives higher phase values and potentially higher phase SNR, but it also leads to more T_2^* signal decay and larger apparent volume of the object. Any error in estimating the volume of the object will lead to error in estimating the susceptibility of that object (10). On the other hand, the effective magnetic moment can be used as surrogate to reflect the changes of the object of interest (10-12).

Furthermore, the susceptibility maps can also be combined with the magnitude images to produce tSWI images (13,14). This helps to remove the orientation dependence of conventional SWI data. These tSWI images provide improved delineation of the geometries of veins and microbleeds and tSWI data processing can be easily incorporated with the current SWI data processing scheme. Thus tSWI has great potential in studies of traumatic brain injury (TBI) (13).

There are also a few limitations in the techniques presented in this thesis. First, all of the techniques are for the data collected with single orientation. Orientation dependence of the susceptibility values of the white matter structures has been reported in former studies, and has been attributed to the myelin sheath surrounding the axons in the white matter (15–18). This requires more sophisticated models to describe the relation between field

variation and susceptibility distribution (19–21). In addition to the susceptibility anisotropy, nonlinear phase evolution was also observed and can be modeled using multi water compartments (17). Both the orientation dependence and nonlinear phase evolution are neglected in this thesis, since this thesis is focused on the deep grey matter structures and veins (18). Second, the method of improving the accuracy of susceptibility quantification using volume constraint was only demonstrated with a phantom, but without any *in vivo* data. The main application of this method is quantification of cerebral microbleeds or calcifications. For *in vivo* data, an estimate of the true volume of the microbleeds from the spin echo data may not be available. If multi-echo data were collected, it is possible to get an estimate of the true volume at TE=0 through extrapolation using the measured apparent volumes at different TEs. Otherwise, the effective magnetic moment could be used to study the longitudinal changes of the microbleeds or calcifications (12).

Future directions include the following aspects. First, the performance of the iterative SWIM algorithm for solving the ill-posed inverse problem in susceptibility mapping could be improved. The effectiveness of the iterative SWIM algorithm relies on proper extraction of the geometries of different structures of interest. Currently, the geometries are extracted purely from susceptibility maps. The accuracy of the extracted geometries could be potentially improved by incorporating the geometries found in the magnitude and phase images (8). Second, the lost phase information near the edge of the brain, due to erosion of the background field removal algorithm, should be recovered as much as possible. This can be achieved by preserving the signal outside the brain. Previous studies

have already shown that it is possible to keep the phase in the skull region (22). This provides more accurate boundary conditions for background field removal and thus reduces the error of background field removal near the edges of the brain. Third, the accuracy of susceptibility quantification could be further improved. Particularly, the quantification of the susceptibility of veins is usually affected by partial volume effects, especially for small veins. Future studies should aim to model and compensate for the partial volume effects. Other future directions include: compensation for the signal loss caused by homodyne high-pass filtering, in a way similar to the deconvolution step in SHARP; incorporation of partial volume effects in the magnitude and phase images of the 3D brain model.

In conclusion, quantitative susceptibility mapping is a promising technique which has many potential applications. It can be applied to most of the applications found by susceptibility weighted imaging (5,23). It is also finding newer applications, given its ability to quantify the source of the phase information and its independence of echo time or orientation, such as tracking and quantifying iron labeled stem cells (24). The accuracy of QSM is dependent on both the imaging acquisition and image post-processing. This thesis has focused on two core steps of QSM post-processing: background field removal and solving the inverse problem. While a new algorithm has been proposed for background field removal, an improved method for solving the inverse problem has also been demonstrated. Both of them contribute to a more sophisticated data processing scheme for quantitative susceptibility mapping with improved effectiveness and accuracy.

References

1. Li L, Leigh JS. High-precision mapping of the magnetic field utilizing the harmonic function mean value property. J. Magn. Reson. 1997 2001;148:442–8.

2. Zhou D, Liu T, Spincemaille P, Wang Y. Background field removal by solving the Laplacian boundary value problem. NMR Biomed. 2014;

3. Griswold MA, Jakob PM, Heidemann RM, Nittka M, Jellus V, Wang J, et al. Generalized autocalibrating partially parallel acquisitions (GRAPPA). Magn. Reson. Med. 2002;47:1202–10.

4. Hammond KE, Lupo JM, Xu D, Metcalf M, Kelley DAC, Pelletier D, et al. Development of a robust method for generating 7.0 T multichannel phase images of the brain with application to normal volunteers and patients with neurological diseases. NeuroImage 2008;39:1682–92.

5. Haacke EM, Reichenbach JR, editors. Susceptibility Weighted Imaging in MRI: Basic Concepts and Clinical Applications. 1st ed. Wiley-Blackwell; 2011.

6. Robinson S, Grabner G, Witoszynskyj S, Trattnig S. Combining phase images from multi-channel RF coils using 3D phase offset maps derived from a dual-echo scan. Magn. Reson. Med. 2011;65:1638–48.

7. Liu J, Liu T, de Rochefort L, Ledoux J, Khalidov I, Chen W, et al. Morphology enabled dipole inversion for quantitative susceptibility mapping using structural consistency between the magnitude image and the susceptibility map. NeuroImage 2012;59:2560–8.

8. Schweser F, Sommer K, Deistung A, Reichenbach JR. Quantitative susceptibility mapping for investigating subtle susceptibility variations in the human brain. NeuroImage 2012;62:2083–100.

9. Tang J, Liu S, Neelavalli J, Cheng YCN, Buch S, Haacke EM. Improving susceptibility mapping using a threshold-based K-space/image domain iterative reconstruction approach. Magn. Reson. Med. 2013;69:1396–407.

10. Liu S, Neelavalli J, Cheng Y-CN, Tang J, Mark Haacke E. Quantitative susceptibility mapping of small objects using volume constraints. Magn. Reson. Med. 2013;69:716–23.

11. Schweser F, Deistung A, Lehr BW, Reichenbach JR. Differentiation between diamagnetic and paramagnetic cerebral lesions based on magnetic susceptibility mapping. Med. Phys. 2010;37:5165.

12. Liu T, Surapaneni K, Lou M, Cheng L, Spincemaille P, Wang Y. Cerebral microbleeds: burden assessment by using quantitative susceptibility mapping. Radiology 2012;262:269–78.

13. Liu S, Mok K, Neelavalli J, Cheng YCN, Tang J, Ye Y, et al. Improved MR Venography Using Quantitative Susceptibility-Weighted Imaging. J. Magn. Reson. Imaging 2013;

14. Gho S-M, Liu C, Li W, Jang U, Kim EY, Hwang D, et al. Susceptibility map-weighted imaging (SMWI) for neuroimaging. Magn. Reson. Med. 2013;

15. Liu C, Li W, Johnson GA, Wu B. High-field (9.4 T) MRI of brain dysmyelination by quantitative mapping of magnetic susceptibility. NeuroImage 2011;56:930–8.

16. Li X, Vikram DS, Lim IAL, Jones CK, Farrell JAD, van Zijl PCM. Mapping magnetic susceptibility anisotropies of white matter in vivo in the human brain at 7 T. NeuroImage 2012;62:314–30.

17. Wharton S, Bowtell R. Fiber orientation-dependent white matter contrast in gradient echo MRI. Proc. Natl. Acad. Sci. U. S. A. 2012;109:18559–64.

18. Rudko DA, Klassen LM, de Chickera SN, Gati JS, Dekaban GA, Menon RS. Origins of orientation dependence in gray and white matter. Proc. Natl. Acad. Sci. U. S. A. 2014;111:E159–167.

19. He X, Yablonskiy DA. Biophysical mechanisms of phase contrast in gradient echo MRI. Proc. Natl. Acad. Sci. U. S. A. 2009;106:13558–63.

20. Liu C. Susceptibility tensor imaging. Magn. Reson. Med. 2010;63:1471–7.

21. Luo J, He X, Yablonskiy DA. Magnetic susceptibility induced white matter MR signal frequency shifts-experimental comparison between Lorentzian sphere and generalized Lorentzian approaches. Magn. Reson. Med. 2013;

22. Buch S, Liu S, Cheng Y, Haacke E. Susceptibility Mapping of the Sinuses in the Brain by Preserving Phase Information in the Skull Using Short Echo Times. Proc. 21st Annu. Meet. ISMRM Salt Lake City Utah USA 2013;:2483.

23. Mittal S, Wu Z, Neelavalli J, Haacke EM. Susceptibility-Weighted Imaging: Technical Aspects and Clinical Applications, Part 2. Am. J. Neuroradiol. 2009;30:232–52.

24. Ruggiero A, Guenoun J, Smit H, Doeswijk GN, Klein S, Krestin GP, et al. In vivo MRI mapping of iron oxide-labeled stem cells transplanted in the heart. Contrast Media Mol. Imaging 2013;8:487–94.